

**The Temperature Dependence of Giant Dipole  
Resonance Width at Excited States  
of Atomic Nuclei**

*By*

**BALARAM DEY**

Enrolment No. : PHYS04201004008

Experimental Nuclear Physics Division

VARIABLE ENERGY CYCLOTRON CENTRE

Kolkata-700064, India

*A thesis submitted to the  
Board of Studies in **Physical Sciences**  
In partial fulfillment of requirements  
For the Degree of  
**DOCTOR OF PHILOSOPHY**  
of*

**HOMI BHABHA NATIONAL INSTITUTE**  
Bhabha Atomic Research Centre  
Mumbai-400085, India



August, 2015



## STATEMENT BY AUTHOR

This dissertation has been submitted in partial fulfillment of requirements for an advanced degree at Homi Bhabha National Institute (HBNI) and is deposited in the Library to be made available to borrowers under rules of the HBNI.

Brief quotations from this dissertation are allowable without special permission, provided that accurate acknowledgement of source is made. Requests for permission for extended quotation from or reproduction of this manuscript in whole or in part may be granted by the Competent Authority of HBNI when in his or her judgment the proposed use of the material is in the interests of scholarship. In all other instances, however, permission must be obtained from the author.

BALARAM DEY



## DECLARATION

I, hereby declare that the investigation presented in the thesis has been carried out by me. The work is original and has not been submitted earlier as a whole or in part for a degree / diploma at this or any other Institution / University.

BALARAM DEY



# List of Publications

## A. In Peer Reviewed Journal

1. “*Experimental investigation on the temperature dependence of the nuclear level density parameter*”, **Balaram Dey**, Deepak Pandit, Srijit Bhattacharya, K. Banerjee, N. Quang Hung, N. Dinh Dang, Debasish Mondal, S. Mukhopadhyay, Surajit Pal, A. De and S. R. Banerjee, **Phys. Rev. C 91 (2015) 044326**.
- \*2. “*Examination of level density prescriptions for the interpretation of high-energy  $\gamma$ -ray spectra*”, Srijit Bhattacharya, Deepak Pandit, **Balaram Dey**, Debasish Mondal, S. Mukhopadhyay, Surajit Pal, A. De and S. R. Banerjee, **Phys. Rev. C 90 (2014) 054319**.
- \*3. “*Probing the critical behavior in the evolution of GDR width at very low temperatures in  $A \sim 100$  mass region*”, **Balaram Dey**, Debasish Mondal, Deepak Pandit, S. Mukhopadhyay, Surajit Pal, Srijit Bhattacharya, A. De, K. banerjee, N. Dinh Dang, N. Quang Hung and S.R. Banerjee, **Phys. Lett. B 731 (2014) 92**.
4. “*A Unique TAS Setup for high multiplicity events at VECC, Kolkata using  $BaF_2$  detectors*”, G. Mukherjee, **Balaram Dey**, S. Mukhopadhyay, Surajit Pal, H. Pai and S. R. Banerjee, **EPJ Web of Conferences 66 (2014) 11026**.
- \*5. “*Giant dipole resonance width and the universality of a fluctuation model including critical temperature*”, Deepak Pandit, Srijit Bhattacharya, **Balaram Dey**, Debasish Mondal, S. Mukhopadhyay, Surajit Pal, A. De and S. R. Banerjee, **Phys. Rev. C 90 (2014) 054319**.

---

\*Indicates publications related to this thesis.

- \*6. “Giant dipole resonance width as a probe for nuclear deformation at finite excitation”, Deepak Pandit, **Balaram Dey**, Srijit Bhattacharya, Debasish Mondal, S. Mukhopadhyay, Surajit Pal, A. De and S. R. Banerjee, **Phys. Rev. C 87 (2013) 044325**.
- \*7. “Neutron response of the LAMBDA spectrometer and neutron interaction length in  $BaF_2$ ”, **Balaram Dey**, Debasish Mondal, Deepak Pandit, Srijit Bhattacharya, S. Mukhopadhyay, Surajit Pal, K. Banerjee, A. De and S. R. Banerjee, **NIM A 727 (2013) 711**.

## B. In Conference & Symposia

- 1. “Experimental investigation on the temperature dependence of the nuclear level density parameter” **Balaram Dey**, Deepak Pandit, Srijit Bhattacharya, Debasish Mondal, S. Mukhopadhyay, Surajit Pal, A. De, K. Banerjee, and S. R. Banerjee **DAE Symp. on Nucl. Phys. 59 (2014) 76**.
- \*2. “Verification of the critical behavior of the Giant Dipole Resonance width in  $A \sim 100$  mass region” **Balaram Dey**, Debasish Mondal, Deepak Pandit, S. Mukhopadhyay, Surajit Pal, Srijit Bhattacharya, A. De, K. Banerjee and S. R. Banerjee **DAE Symp. on Nucl. Phys. 58 (2013) 52**.
- †3. “Measurement of average interaction length of neutrons in  $BaF_2$  crystal” **Balaram Dey**, Debasish Mondal, Deepak Pandit, S. Mukhopadhyay, Surajit Pal and S. R. Banerjee, **DAE Symp. on Nucl. Phys. 58 (2013) 844**.
- \*4. “Neutron response of the LAMBDA spectrometer” **Balaram Dey**, Deepak Pandit, S. Mukhopadhyay, Surajit Pal, K. Banerjee, S. R. Banerjee **DAE**

---

†Indicates publications related to this thesis.

- Symp. on Nucl. Phys. 57 (2012) 868.**
5. “*Clover detector setup at VECC*” Soumik Bhattacharya, **Balaram Dey**, A. Saha, A. Choudhury, S. Bhattacharyya, T. Bhattacharjee, S.R. Banerjee, S. Das Gupta, D. Mondal, G. Mukherjee, S. Mukhopadhyay, P. Mukhopadhyay, D. Pandit, S. Pal, T. Roy, I. Seikh, **DAE Symp. on Nucl. Phys. 58 (2013).**
- \*6. “*Determination of the nuclear deformation via the giant dipole resonance width at finite temperature*” Deepak Pandit, **Balaram Dey**, Debasish Mondal, S. Mukhopadhyay, Srijit Bhattacharya, Surajit Pal, A. De and S. R. Banerjee, **DAE Symp. on Nucl. Phys. 58 (2012).**
7. “*A modular TAS Setup at VECC using BaF<sub>2</sub> detectors*” G Mukherjee, **Balaram Dey**, S Mukhopadhyay, Deepak Pandit, Surajit Pal, H Pai, S. R Banerjee **DAE Symp. on Nucl. Phys. 57 (2012) 872.**
- \*8. “*The effect of level density prescriptions on the understanding of high energy  $\gamma$ -ray spectra*” Srijit Bhattacharya, Deepak Pandit, **Balaram Dey**, Debasish Mondal, S. Mukhopadhyay, Surajit Pal, A. De and S. R. Banerjee **DAE Symp. on Nucl. Phys. 59 (2014) 178.**
9. “*The decay of high energy GDR  $\gamma$ -rays from <sup>32</sup>S nucleus*” Deepak Pandit, Debasish Mondal, **Balaram Dey**, Srijit Bhattacharya, S. Mukhopadhyay, Surajit Pal, A. De and S. R. Banerjee **DAE Symp. on Nucl. Phys. 59 (2014) 64.**
10. “*Indication of long fission lifetime of <sup>242</sup>Pu at  $E_X \sim 55$  MeV*” A. Ray, A. K. Sikdar, **Balaram Dey**, D. Pandit, S. Bhattacharya, A. De, S. Paul, Srijit Bhattacharya, A. Bisoi **DAE Symp. on Nucl. Phys. 59 (2014) 486.**

11. “*Measurement of Intrinsic Neutron Detection Efficiency of a Liquid Scintillator using Digital Data Acquisition System*”  
Abhijit Bisoi, D. Pramanik, **Balaram Dey** and M. Saha Sarkar. **DAE Symp. on Nucl. Phys. 58 (2013) 998.**
12. “*Isospin symmetry breaking at high excitation via isovector giant dipole resonance decay in  $^{32}\text{S}$* ” Debasish Mondal, Deepak Pandit, **Balaram Dey**, S. Mukhopadhyay, Surajit Pal, A. De, Srijit Bhattacharya, and S. R. Banerjee, **DAE Symp. on Nucl. Phys. 58 (2013) 50.**
13. “*Suitability of Digital Signal Processing for LAMBDA spectrometer*” Debasish Mondal, S. Mukhopadhyay, **Balaram Dey**, Deepak Pandit, Surajit Pal, Pranab Singha Roy, Partha Dhara, S.R. Banerjee, **DAE Symp. on Nucl. Phys. 58 (2013) 894.**
14. “*An investigation on off-shell behavior of nuclear reaction in the alpha-induced break-up of deuterons at low energies*” A. De, Sushovan Paul, Debakinandan Majee, S. R. Banerjee, Surajit Pal, S. Mukhopadhyay, Deepak Pandit, **Balaram Dey**, Debasish Mondal and Srijit Bhattacharya **DAE Symp. on Nucl. Phys. 59 (2014) 376.**
15. “*Evolution of collectivity in  $^{160}\text{Yb}$* ” A. Saha, T. Bhattacharjee, S. Rajbanshi, A. Bisoi, D. Curien, J. Dudek, P. Petkov, D. Banerjee, S. R. Banerjee, Soumik Bhattacharya<sup>1</sup>, S. Bhattacharyya, S. Biswas, A. Chakraborty, G. de Angelis, S. K. Das, S. Das Gupta, **Balaram Dey**, G. Duchene, A. Goswami, D. Mondal, D. Pandit, R. Palit<sup>6</sup>, T. Roy, M. Saha Sarkar, S. Saha, R. P. Singh, J. Sethi **DAE Symp. on Nucl. Phys. 59 (2014) 376.**

## DEDICATIONS

Dedicated to my Grandfather  
**SHRI NARAYAN CHANDRA DEY**



## ACKNOWLEDGEMENTS

This thesis owes its existence to the help, support and inspiration of several people. First and foremost, I would like to express my sincerest appreciation and gratitude to my supervisor, Prof. Sudhee Ranjan Banerjee, who has guided me through the past four years since I began my research career. He has continuously encouraged, advised, and supported me in all the aspects of my thesis work. I have learnt from him not only skillful experimental techniques but also the necessary attitudes to solve scientific problems. His support and inspiring suggestions have been precious for the development of this thesis content.

I am deeply grateful to my collaborators Dr Supriya Mukhopadhyay, Dr Deepak Pandit, Dr Surajit Pal, Shri Debasish Mondal, Dr Srijit Bhattacharya and Dr Alok De. They have been constant source of encouragement and enthusiasm, not only during this thesis project but also during the four years of my research life. All of them help me tremendously during the completion of my investigation. It would have never been possible to complete this thesis without their dedicated supervision. I have learnt academically and personally many things from them. They are not only my collaborators but also good elder brothers protecting me. I feel very fortunate for being a part of this prestigious group. I would also like to thank my international collaborators Prof. N Dinh Dang, RIKEN, Japan and Prof. N Quang Hung, Tan Tao University, Vietnam for their theoretical support in my Ph.D work.

It is my great pleasure to thank Hari da (Dr Haridas Pai) who first introduced me to my Ph.D collaborators and constantly encouraged me to work with them.

A special thanks must go to Shri Harihar Pan without whom I would have never started this wonderful academic career. He was my school teacher, who

showed me the right path in my academic career. Thank you Sir and no matter where you are around the world, you are always with me !

I am very much indebted to our Director Prof. Dinesh Kumar Srivastava, for his constant inspiration. I met him and discussed with the prospectus of research with him before joining VECC and he has motivated and encouraged ever since. I owe my sincerest gratitude to Dr Sailajananda Bhattacharya, Dr Chandana Bhattacharya, Dr V S Pandit, Dr Gopal Mukherjee and Dr Sarmistha Bhattacharya for their encouragement and kind support. I would also like to give my sincere thanks to Dr Tilak Kumar Ghose, Dr Kaushik Banerjee, Dr Tapan Rana, Dr Samir Kundu, Dr Tumpa Bhattacharya, Ratnesh Panday, Pratap Roy, J K Meena, Santu Manna, Soumik Bhattacharya, Arindam Sikdar, Asif Reja and other senior colleagues of Physics Group for their help and suggestions at various stages. Thanks to the VECC Cyclotron operators for a smooth running of the accelerator during thesis experiments.

I would like to warmly thank my colleagues cum friends Sumit Basu, Subikash Choudhury, Rajesh Ganai and Arindam Roy for their constant help in academically. They always extended their kind support whenever I approached them. These guys have helped me to deal with all my frustration during the time here. I will forever remember in my heart the stories and the moments you boys shared with me during these five years in my research life.

I would like to thank my colleagues Maitreyee Mukherjee, Vishal Srivastava and Rihan Haque for their support. I would also like to give a big thanks to my friends Kalipada Das, Raju Halder, Divyadyuti Pramanik, Angsuman Patra, Kuntal Talit, Sukhen Paramanik, Debabrata Mondal, Rajib Samanta, Tutul Dey, Bapan Mondal, Soumitra Banerjee, Dulal Shit, Ajoy De, Baban Karmakar, Sujoy Bid, Baidyanath Roy and Sampa Karmakar for their constant

inspiration.

It is a pleasure to thank Younus da, Trambak da, Surasree di, Nihar da, Sudipan da, Subhash da, Somnath da, Manish da, Arnab da, Nasim da, Amal da, Sukanya di, Debojit, Somnath, Rana, Rajendra, Sarowar, Arunavo, Arghya, Avirup, Debasish, Tanmoy, Noor, Asgar and Abhijit Bisoi for their support.

I would like to thank those people in my life who may not have contributed directly to my research work but have made it possible to fulfill my dream. First of all, thanks to my parents for their unflagging love and unconditional support throughout my life and my studies, and allowing me to be just as ambitious as I wanted. Secondly, I am extremely indebted to my grandmothers (Labanyamoyee Dey), uncles (Gouranga Dey, Banshi Badan Dey, Tarak Nath Dey), aunties (Vandana Dey and Chobi Rani Dey), brothers (Krishna, Lob and Kush) and sisters (Soma, Tutu, Piku, Mou, Munu, Priya and Shrabani) and jiju's (Swapan Nandi, Nibas Barui, Gopinath Paul, Bubai Maji and Avik Kundu) for their constant inspiration. I also convey my thanks to Anath Bandhu Sir and Samir dadu for their guidance and help during my school days. Finally, I would like to address my heartfelt acknowledgment to Neepamala Giri for her continuous support and encouragement.

I sincerely apologize inadvertent omission of any name from the above list of acknowledgment.



# Contents

<b>SYNOPSIS</b> . . . . .	xvii
<b>List of Figures</b> . . . . .	xxxii
<b>List of Tables</b> . . . . .	xxxvii
<b>1 Introduction</b> . . . . .	<b>1</b>
1.1 Giant resonances (GR) . . . . .	2
1.2 Classification of Giant resonances . . . . .	2
1.3 Isovector giant dipole resonance (IVGDR) . . . . .	5
1.3.1 IVGDR built on ground state . . . . .	6
1.3.2 IVGDR built on excited state . . . . .	6
1.3.3 High energy $\gamma$ -ray spectrum from the decay of GDR built on excited state . . . . .	7
1.4 Parameters for characterizing the GDR vibration . . . . .	8
1.4.1 Strength function $S_{GDR}$ . . . . .	9
1.4.2 Resonance energy, $E_{GDR}$ . . . . .	10
1.4.3 Width of the resonance, $\Gamma_{GDR}$ . . . . .	12
1.5 Origin of the GDR width . . . . .	13
1.5.1 Macroscopic description . . . . .	13
1.5.2 Microscopic description . . . . .	13
1.6 Evolution of GDR width built on excited states of atomic nuclei	15
1.6.1 Experimental observation . . . . .	15
1.6.2 Theoretical explanation . . . . .	22
1.7 Motivation of the present work . . . . .	24

<b>2</b>	<b>Theoretical tools to interpret the high energy <math>\gamma</math>-ray spectra</b>	<b>27</b>
2.1	Statistical Model Calculations . . . . .	27
2.2	CASCADE : A statistical model code . . . . .	29
2.2.1	Decay probabilities . . . . .	30
2.2.2	Nuclear level density . . . . .	32
2.3	Theoretical treatment of GDR width at finite T & J . . . . .	34
2.3.1	Thermal Shape Fluctuation Model (TSFM) : A macroscopic calculation . . . . .	35
2.3.2	Critical Temperature included Fluctuation Model (CTFM) : A new parametrization of TSFM . . . . .	41
2.3.3	Phonon Damping Model (PDM) : A microscopic calculation . . . . .	44
2.4	Bremsstrahlung corrections . . . . .	46
<b>3</b>	<b>Detectors and simulation studies</b>	<b>48</b>
3.1	$\gamma$ -ray detectors . . . . .	48
3.1.1	The LAMBDA spectrometer . . . . .	52
3.1.2	Multiplicity filter . . . . .	54
3.2	Neutron detector: Liquid organic scintillator (BC501A) . . . . .	56
3.3	GEANT4 simulation of the detector systems . . . . .	58
3.3.1	Simulation of the LAMBDA array and its response function . . . . .	59
3.3.2	Simulation of Multiplicity filter and conversion of experimental fold distribution to angular momentum distribution . . . . .	62
3.3.3	Simulation of BC501A neutron detector and its efficiency . . . . .	65
<b>4</b>	<b>Experimental Details and data analysis</b>	<b>68</b>
4.1	Detector set-up . . . . .	68
4.2	Electronic set-up . . . . .	70
4.2.1	Electronics for measuring the angular momentum gated high energy $\gamma$ -ray spectra . . . . .	71
4.2.2	Electronics for neutron energy measurement . . . . .	74
4.3	Detectors calibration . . . . .	76
4.4	Data reduction technique . . . . .	78

4.4.1	Rejection of neutron backgrounds . . . . .	78
4.4.2	Rejection of pile-up events . . . . .	79
4.4.3	Cosmic event rejection . . . . .	80
4.5	Measurement of high energy $\gamma$ -rays using cluster summing technique . . . . .	81
4.6	Extraction of angular momentum . . . . .	85
4.7	Measurement of evaporated neutron energy spectrum . . . . .	86
4.7.1	Calculation of compound nucleus temperature . . . . .	88
4.7.2	The effect of nuclear level density formalism on the high energy $\gamma$ -ray spectra . . . . .	90
4.8	Extraction of GDR parameters . . . . .	93
<b>5</b>	<b>Results and discussion</b>	<b>97</b>
5.1	Evolution of GDR width at low temperature . . . . .	97
5.1.1	GDR width as a function of temperature with macroscopic TSFM calculation . . . . .	98
5.1.2	GDR width as a function of temperature with new CTFM calculation . . . . .	99
5.1.3	GDR width as a function of temperature with microscopic PDM calculation . . . . .	100
5.2	Determination of nuclear deformation via GDR width at finite temperature for $^{97}\text{Tc}$ . . . . .	101
5.3	Discussion on the experimental results . . . . .	102
<b>6</b>	<b>Neutron response of LAMBDA spectrometer</b>	<b>105</b>
6.1	Introduction . . . . .	105
6.2	Experimental Details . . . . .	107
6.2.1	Efficiency measurement . . . . .	107
6.2.2	Time-of-flight energy resolution . . . . .	112
6.3	In-beam-experiment: LAMBDA used as a neutron detector . . .	116
6.4	Results and discussion . . . . .	119
<b>7</b>	<b>Summary and Conclusion</b>	<b>120</b>

**Bibliography** . . . . . 125

# SYNOPSIS

One of the important aspects in nuclear many body system has been to describe the emergence of collective features of nuclei as well as their structures in terms of the individual motion of nucleons. Giant dipole resonance (GDR), the most prominent collective mode of excitation, present in all nuclei, has been studied extensively and considered as an important tool to probe the properties of nuclei in extreme conditions of spin and temperature. The GDR vibration decays either via particle emission or high energy  $\gamma$ -ray ( $> 8$  MeV) emission. The high energy  $\gamma$ -rays are the cleanest probe to study GDR properties as the  $\gamma$ -rays are not strongly affected by the nuclear medium. The decaying  $\gamma$ -rays from the GDR vibration of nuclei have the characteristics of Lorentzian strength function. The centroid energy of this strength function is related to the nuclear symmetry energy which is useful for the investigation of equation of state of nuclear matter and also has astrophysical interest. Interestingly, the GDR couples with the nuclear shape degrees of freedom and therefore can directly probe the nuclear deformation. Along with that, the time scale of GDR vibration is very short and thus provides valuable information in different interesting nuclear phenomena like loss of collectivity, neutron-proton asymmetry at high temperatures, angular momentum driven exotic shapes, Jacobi shape transition at very high spins, super deformation of the alpha-cluster nuclei, etc.

The primary interest in GDR research lies in the understanding of the GDR width of hot and rapidly rotating excited nuclei, as it is the major source of information on nuclear damping and shape evolution at extreme conditions. The experimental studies on the evolution of GDR width, over the years, have shown that the GDR width increases with both temperature (T) and angular momentum (J), whereas its centroid energy remains mostly unchanged as T

and  $J$  vary. In this regard, it is worthwhile to mention that the effect of  $J$  and  $T$  on the GDR width becomes noticeable only above a critical angular momentum,  $J_c \sim 0.6A^{5/6}$  and  $T \sim 1$  MeV. Although, a wealth of data exists on the angular momentum dependence of GDR width in different mass regions, the measurement of GDR width at low temperatures ( $T < 1$  MeV) is rather scarce due to the experimental difficulties in populating the nuclei at low excitation energies. The present thesis presents a systematic as well as precise experimental data on the GDR width, specifically, at this very low temperature region ( $T < 1.5$  MeV). It is also our endeavor to systematically assess the different theoretical models and thereby understand the complete nature of the damping mechanism as a function of  $T$  inside the atomic nucleus.

A number of theoretical approaches have been proposed to demonstrate the behavior of the GDR width as a function  $T$  and  $J$ . Macroscopically, the evolution of GDR width as a function of  $T$  and  $J$  is well described by the widely accepted Thermal Shape Fluctuation Model (TSFM). The TSFM is based on the large-amplitude thermal fluctuations of the nuclear shape under the assumption (adiabatic assumption) that the time scale associated with thermal fluctuations is slow compared to GDR vibrations. According to TSFM, the nucleus does not possess a single well-defined shape at a given  $T$  and  $J$  but rather assumes a broad ensemble of mostly quadrupole shapes (deformation) due to thermal fluctuations. Thus, under the adiabatic assumption, the observed GDR width results from a weighted average over all frequencies associated with the possible shapes leading to the increase in the apparent GDR width as a function of  $T$ . Although, this model explains rather well the  $J$  dependence of the GDR width as well as the mass dependence of the critical angular momentum ( $J_c$ ) and Jacobi shape transition, it fails completely to explain the  $T$  dependence below 1.5 MeV. This has recently been observed in different mass regions ranging

from lower to higher masses. Microscopically, the increase of the GDR width as a function of  $T$  is described reasonably well within the Phonon Damping Model (PDM). The PDM calculates the GDR width and the strength function directly in the laboratory frame without any need for an explicit inclusion of thermal fluctuation of shapes. On the other hand, the macroscopic Thermal Shape Fluctuation Model (TSFM) is based on the thermal fluctuations of the nuclear shape which plays an important role in describing the increase of the apparent GDR width as a function of  $T$ .

Recently, a new model has been proposed by modifying the phenomenological parametrization (pTSFM) based on the TSFM framework and is called the Critical Temperature included Fluctuation Model (CTFM). The model emphasizes on an essential point, completely overlooked in the TSFM, that the GDR oscillation itself induces a quadrupole moment causing the nuclear shape to fluctuate even at  $T = 0$  MeV. Consequently, the GDR vibration cannot view those inherent thermal fluctuations that are smaller than its own intrinsic fluctuations. Therefore, the experimental GDR width should remain nearly constant at the ground state value up to a critical temperature ( $T_c$ ) and the effect of thermal fluctuations should be evident above  $T_c$  only when they become larger than the intrinsic GDR fluctuations. The CTFM gives good description of the GDR width behavior for both  $T$  and  $J$  in the entire mass region. Unfortunately, the existing number of GDR width measurements at  $T < 1$  MeV are highly inadequate to test the critical behaviour of the GDR width as well as to conclude that the GDR width remains nearly constant at the ground state value below  $T \sim 1$  MeV as predicted by both PDM and CTFM. Simultaneously, it is also important to verify experimentally with a major focus towards the understanding of the nature of the mass dependence of the critical behavior.

In order to understand the exact behavior of the GDR width at lower tem-

peratures, a systematic and precise measurement of the GDR widths in the unexplored region ( $T = 0.8 - 1.5$  MeV) for the medium mass nuclei  $^{97}\text{Tc}$  have been performed. Experimentally, the measurement of GDR width at low temperatures ( $T < 1.5$  MeV) is very complex and challenging problem and precise measurement of such low temperature is very difficult. Previously, low temperature measurements were performed via inelastic scattering of lighter projectile by heavier target with a disadvantage of getting imprecise excitation energy with an uncertainty about 10 MeV due to the large inelastic energy loss. On the other hand, heavy ion fusion reactions are limited to higher temperature with a broad J distributions due to the presence of large coulomb barrier. In this thesis work, alpha induced fusion reaction have been used to investigate the low temperature region. The experiments involved low angular momenta with an accurate measurement of temperatures and explored GDR width up to a temperature as low as 0.8 MeV. This is the first measurement of the GDR width at finite temperature in  $A \sim 100$  mass region both above and below the critical point and can be effectively used to verify the existing theoretical models.

The experiments were performed using the alpha beam from K-130 cyclotron at the Variable Energy Cyclotron Centre (VECC), Kolkata, India. A self supporting  $1 \text{ mg/cm}^2$  thick  $^{93}\text{Nb}$  target was bombarded with the alpha beams produced by the K-130 cyclotron at four different incident energies of 28, 35, 42 and 50 MeV to populate the compound nucleus  $^{97}\text{Tc}$  at the excitation energies of 29.3, 36.0, 43.0 and 50.4 MeV, respectively. The high-energy  $\gamma$ -rays from the GDR decay were measured using the Large Area Modular  $\text{BaF}_2$  Detector Array (LAMBDA), designed and fabricated in-house at VECC. The array was arranged in  $7 \times 7$  matrix and placed at a distance of 50 cm from the target (covering a solid angle 1.8% of  $4\pi$ ) and at an angle  $90^\circ$  with the beam axis. Since,

the GDR widths depend on both the excitation energies and populated angular momenta, it is important to disentangle the two effects in order to understand their individual contributions. Therefore, along with the LAMBDA spectrometer, a 50-element low energy  $\gamma$ -multiplicity filter was also used around the target to estimate the angular momenta populated in the compound nucleus (CN) as well as to get a fast start trigger for time-of-flight (TOF) measurement. The multiplicity filter was split into two blocks of 25 detectors each, in a staggered castle type geometry to equalize the solid angle for each multiplicity detector element, and placed at a distance of 5 cm above and below the centre of the target. The TOF technique was used to separate the neutron background in the high-energy  $\gamma$ -spectrum. Pile up events were rejected using the pulse shape discrimination (PSD) technique by measuring the charge deposition over two integrating time intervals (50 ns and 2  $\mu$ s) in each of the detectors. The effect of angular momentum on the GDR width starts showing up above the critical angular momentum  $J_c = 27 \hbar$  in this mass region. Therefore, the populated angular momenta ( $13\hbar - 21\hbar$ ) were kept below the critical angular momentum so that it does not have any effect on GDR width.

To interpret properly the experimental data with the statistical model calculation, nuclear level density (NLD) parameter plays an important role. The parameter is an important input in statistical model calculation as well as estimation of proper nuclear temperature. Recent measurements on the nuclear level density parameter have shown that the inverse level density parameter ( $k = A/a$ ) depends on the temperature and angular momentum populated in the compound nucleus. Hence, to fix the inverse level density parameter at experimental value of T and J, the evaporated neutrons from the  $^{97}\text{Tc}$  compound nucleus were also measured independently by employing a liquid organic scintillator (BC501A) based neutron detector in coincidence with the  $\gamma$ -multiplicities.

The neutron detector was placed at a distance of 1.5 m from the target position at an angle of  $125^\circ$  with respect to the beam axis. The neutron TOF spectra were converted to energy spectra by considering the prompt  $\gamma$ -peak as time reference. Efficiency correction for the neutron detector was carried out using GEANT4 simulation. The evaporated neutron energy spectra corresponding to different folds were compared with the statistical model calculation (CASCADE) to determine the nuclear level density parameter using a chi-square minimization technique in the energy range of 2–7 MeV in the evaporated neutron spectra.

The high energy  $\gamma$ -ray spectra were extracted by gating on different folds of the multiplicity events from the off-line analysis of the data recorded in event-by-event mode by applying the proper cuts on the TOF and PSD spectra. After applying all the necessary cuts and rejections in a valid event, the energy deposited in the detectors were summed up using nearest neighbor cluster summing technique. Next, the energies were Doppler corrected. The experimentally measured fold distributions from the multiplicity filter were converted into angular momentum distributions using a realistic technique based on GEANT4 simulation. Finally, the angular momentum gated high energy  $\gamma$ -ray spectra were compared with the modified version of statistical model calculation CASCADE along with a bremsstrahlung component folded with the detector response function to extract the GDR parameters.

In the statistical model calculation CASCADE, a single Lorentzian GDR strength function was assumed as  $^{97}\text{Tc}$  nucleus is nearly spherical, having centroid energy ( $E_{GDR}$ ) and width ( $\Gamma$ ) as variable parameters. The simulated spin distributions deduced from the experimental fold distributions were used as inputs for different folds for the analysis of both the neutron and high energy  $\gamma$ -ray analyses. In the CASCADE code, the Ignatyuk level density prescription

was adopted. This prescription implements shell effects at lower temperatures which gradually melts down with the increase in temperature. A few other prescriptions like BJK, Kataria etc also exist that incorporate the excitation energy dependent shell effects. But, those formalisms (BJK and Kataria) have been rigorously checked for different mass regions ( $^{63}\text{Cu}$ ,  $^{97}\text{Tc}$ ,  $^{113}\text{Sb}$  and  $^{201}\text{Tl}$ ) and has been found that the Ignatyuk prescription was found to be most suitable in explaining the high energy  $\gamma$ -ray spectra. The experimental GDR widths at different T and J were obtained from the best fit statistical model calculations using a  $\chi^2$  minimization technique (in the energy range of 10–20 MeV).

As  $\gamma$ -rays from the GDR are emitted from various steps of the compound nuclear decay chain, the average values of J and T have been considered. While estimating the average temperature, a lower limit in the excitation energy ( $E^*$ ) during the CN decay process was employed in the statistical model calculation. This lower limit in  $E^*$  is selected when the cut off in the excitation energy only affects the  $\gamma$ -emission at very low energy but does not alter the GDR region. The average value of  $T$  was calculated from the average excitation energy ( $\overline{E^*}$ ) using the relation  $\overline{T} = [(\overline{E^*} - \overline{E}_{rot} - E_{GDR} - E_p)/a(\overline{E^*})]^{1/2}$ , where  $a(\overline{E^*})$  is the excitation energy-dependent level density parameter and  $E_p$  is the pairing energy.  $\overline{E}_{rot}$  is the rotational energy and was computed at  $\overline{J}$  within the CASCADE corresponding to each fold.  $\overline{E^*}$  is the average of the excitation energy weighted over the daughter nuclei for  $\gamma$ -emission in the GDR region from  $E_\gamma = 10 - 20$  MeV given as  $\overline{E^*} = \sum E_i^* w_i / \sum w_i$ .  $E_i^*$  is the excitation energy of  $i^{th}$  nuclei in the decay steps and  $w_i$  is the yield in the region  $E_\gamma = 10 - 20$  MeV. The estimated average angular momentum lies in between  $13\hbar - 20\hbar$  with an uncertainty of  $\sim 5\hbar$ . The average temperatures were ranging from 0.8 to 1.51 MeV with an uncertainty of  $\sim 0.08$  MeV.

The measured GDR widths at very low temperatures (T=0.8 – 1.5 MeV)

were compared with the different theoretical calculations of GDR width such as macroscopic Thermal Shape Fluctuation Model (TSFM), phenomenological Critical Temperature Fluctuation Model (CTFM) and microscopic Phonon Damping Model (PDM).

In the TSFM calculation, the GDR strength function is calculated by averaging the line shapes corresponding to the different possible deformations of the nuclear shape. The averaging over the distribution of shapes is weighted with a Boltzmann factor  $e^{-F(\beta,\gamma)/T}$ , where  $F(\beta,\gamma)$  is the free energy and  $T$  is the nuclear temperature. The calculations were performed with and without considering the shell effect. As expected for  $^{97}\text{Tc}$ , the effect of shell correction on the GDR width is quite small and leads to similar results as obtained considering the liquid drop model without taking into account shell effect. The TSFM calculations also show that the effect of angular momentum on the GDR width below  $30 \hbar$  is very small and essentially remains unchanged below  $20 \hbar$ . The compound nuclear particle evaporation widths ( $\Gamma_{ev}$ ) were incorporated in the TSFM calculation to take into consideration the effect of evaporation of particles and the corresponding energy loss before and after the GDR  $\gamma$ -emission in the CN decay chain. In this low temperature region, the particle decay width is rather small ( $\sim 0.2$  MeV at  $T = 2$  MeV) and its inclusion within the TSFM marginally improves the prediction. It has been observed that the adiabatic TSFM differs significantly from the experimental data in the entire region. This interesting result clearly suggests that the suppression of the GDR width at these low  $T$  is a general feature for all nuclei and cannot be explained including only shell effects.

In order to compare the data with CTFM, the ground state GDR width was calculated using the ground state deformation ( $\beta = 0.134$ ) and spreading width parametrization  $\Gamma_s = 0.05E_{GDR}^{1.6}$  for each Lorentzian. The ground state

value was estimated to be 5.5 MeV which is consistent with the experimentally measured value in this mass region. The behavior of the GDR width within the CTFM was calculated as a function of  $T$  for  $J = 10$  and  $20 \hbar$ , the extreme values of experimental angular momenta. The  $\Gamma_{ev}$  was not included in the CTFM calculations as the model is purely phenomenological. Interestingly, the CTFM represents the data remarkably well over the entire  $T$  region of interest. This excellent agreement between the experimental data and the CTFM clearly suggests that the experimental GDR widths are not suppressed, rather TSFM overpredicts the GDR width at low temperatures as it does not take into account the intrinsic GDR fluctuations induced by the GDR vibrations. Moreover, the systematic trend of the data also shows that the critical temperature lies in between 1 and 1.2 MeV as predicted by the CTFM ( $T_c = 0.7 + 37.5/A$ ) and the GDR width remains constant below it at the ground state value.

The data were also compared with the results of microscopic PDM calculations. According to PDM, the GDR damping is caused by coupling of the GDR to non-collective particle-hole (ph) and particle-particle (pp) [hole-hole (hh)] configurations. The coupling to the various ph configurations leads to the quantal width (which exists even at  $T = 0$  MeV), whereas the thermal width arises owing to the coupling to pp and hh configurations, which appear at  $T > 0$  MeV because of the distortion of the Fermi surface. The model emphasizes the inclusion of thermal pairing, since in finite systems such as in atomic nuclei, thermal pairing does not collapse at the critical temperature  $T_{cp} = 0.57\Delta(T = 0)$  of the super fluid-normal phase transition in infinite systems, but decreases monotonically as  $T$  increases. The calculations were performed at  $J = 0$  by using the single-particle energies obtained within the deformed Woods-Saxon potentials with the deformation parameter  $\beta = 0.134$ , and including exact canonical-ensemble thermal pairing gaps for neutrons and protons. It has been shown

that, the PDM describes the data quite well in the entire  $T$  range using a width of around 5 MeV at  $T = 0\text{MeV}$ , which is close to the deformed ground state GDR width. It is intriguing to find that, even though the formalisms of PDM and CTFM seem to be completely different in origin, the two models gave very similar results. It would also be very interesting to compare the data with the TSFM by including the effect of thermal pairing, but is beyond the scope of this present work. Nevertheless, the present experimental study does provide a stringent testing ground of the theoretical models as a function of  $T$ .

The average deformations ( $\langle\beta\rangle$ ) were also extracted using the universal correlation between the experimental GDR width and the average deformation of the nucleus at finite  $T$ , and were compared with the TSFM. The correlation has been proposed recently by including the deformation induced by the GDR motion. The empirical deformations extracted from the experimental data match excellently well with the TSFM calculation above  $T_c$ . The good description of the CTFM as well as the validity of the universal correlation indicates that GDR induced quadrupole moment could play a decisive role in suppressing the GDR width at low  $T$ .

Apart from the GDR studies, the thesis also deals with the neutron response of the LAMBDA spectrometer consisting of 162 BaF<sub>2</sub> crystals (each having dimension of  $3.5\times 3.5\times 35\text{ cm}^3$ ) was initially developed for the measurement of high-energy  $\gamma$ -rays. As we know, neutrons are the major source of backgrounds in the high energy  $\gamma$ -rays spectra. Until now, the LAMBDA spectrometer has only been employed efficiently to reject the neutron contamination from the high-energy  $\gamma$ -ray spectrum by the time-of-flight (TOF) technique. However, instead of rejecting the neutrons, they can be utilized to extract the nuclear level density parameter which is an important ingredient for the statistical model calculation. In this thesis work, the neutron response of the LAMBDA spec-

trometer has also been studied and compared with a standard liquid organic scintillator (BC501A) based neutron detector.

The intrinsic neutron detection efficiency of the LAMBDA spectrometer has been measured using a  $^{252}\text{Cf}$  spontaneous fission source (62  $\mu\text{Ci}$ ).  $^{252}\text{Cf}$  decays via  $\alpha$  particle emission (96.91%) and spontaneous fission (3.09%) with a half-life of 2.65 years. Generally, the fission events are measured using fragment detectors such as surface-barrier detectors, PPAC and MWPC. However, since a large number of  $\gamma$ -rays are also emitted from the excited fission fragments, a fast-timing  $\gamma$ -ray detector (e.g.  $\text{BaF}_2$ ) can also be effectively used to select the fission events as well as to obtain the start trigger for neutron TOF measurement.

Four  $\text{BaF}_2$  detectors (a small part of the LAMBDA spectrometer), arranged in  $2 \times 2$  matrix, were kept at a distance of 80 cm from the  $^{252}\text{Cf}$  source to study the neutron response. A BC501A-based neutron detector (5 inch in diameter and 5 inch in length) of known efficiency was also employed to measure the neutron energies, in order to compare its efficiency with that of the  $\text{BaF}_2$  detectors. The neutron detector was kept on the other side of the source at a distance of 150 cm to equalize the solid angle of the two detector systems. Along with these detectors, a 50 element  $\text{BaF}_2$   $\gamma$ -multiplicity filter was also used to detect the low energy discrete  $\gamma$ -rays emitted from the decay of excited fission fragments to establish a correlation between the neutrons and the fission process. The multiplicity filter was split into two blocks of 25 detectors each, in staggered castle type geometry, and placed at a distance of 3 cm above and below the sealed  $^{252}\text{Cf}$  source. The neutron TOF technique was employed for neutron energy measurement in both detector systems using the start signal from the multiplicity filter. Along with the time spectrum, the pulse height spectrum of each detector was also measured to apply energy thresholds in off-line analysis.

The TOF spectrum was converted to energy spectrum using the prompt  $\gamma$  peak as a time reference. The efficiencies of both the detector systems were determined by dividing the neutron yield per fission by the expected neutron energy distribution of  $^{252}\text{Cf}$  (with temperature  $T = 1.42$  MeV), properly normalized with the detector solid angle and the total number of fission events detected. It was interesting to note that, starting at 4 MeV, the neutron efficiency of the BC501A detector decreased monotonically as a function of neutron energy, whereas, the efficiency of the  $\text{BaF}_2$  array increased sharply up to 2–3 MeV and reached a plateau at efficiency  $\sim 34\%$  which was comparable with that of the neutron detector at these energies. It should be mentioned that, the BC501A has an extra advantage in discriminating neutrons from  $\gamma$ -rays using PSD technique. The experimentally measured efficiencies were also compared with the corresponding GEANT4 simulation. It has been found that the experimentally measured efficiencies of the  $\text{BaF}_2$  array and BC501A detector were in good agreement with the corresponding GEANT4 simulations.

The time-of-flight (TOF) energy resolution of neutrons has also been calculated using the formula

$$\left(\frac{\delta E}{E}\right)^2 = \left(2\frac{\delta T}{T}\right)^2 + \left(2\frac{\delta L}{L}\right)^2 \quad (1)$$

where  $\delta E$  is the energy resolution,  $\delta T$  is the time resolution of the detector,  $L$  represents the mean flight length of the neutron and  $\delta L$  is the flight path length spread due to the detector size. Since the density of the  $\text{BaF}_2$  material is high, the neutrons will interact mostly in the initial part of the detector volume. Hence, the total size of the detector should not be taken as the uncertainty in length, rather the average interaction length should be estimated to precisely determine the TOF energy resolution. The interaction point of neutrons in the  $\text{BaF}_2$  crystals was measured using the detector elements (each having dimension of  $3.5 \times 3.5 \times 5.0$  cm<sup>3</sup>) of  $\gamma$  multiplicity filter. Ten  $\text{BaF}_2$  detectors of

multiplicity filter were arranged linearly one after another so that the effective length was 35 cm (same as the length of the LAMBDA detector). A  $^{241}\text{Am-}^9\text{Be}$  source was kept at a distance of 50 cm from the first one of the ten detectors kept in line to measure TOF spectrum for each detector elements. The start trigger for the TOF measurement was taken from another set of identical  $\text{BaF}_2$  detectors which were arranged in a  $2 \times 2$  matrix and kept at a distance of 5 cm on the other side of the source. In order to estimate the average interaction length, the total number of counts in the neutron TOF spectrum was calculated corresponding to an energy range of 3-6 MeV in each of the 10 detectors. It has been found that that the total number of counts is highest for the first detector and decreases for subsequent detectors, pointing towards the fact that the interaction of neutrons in the  $\text{BaF}_2$  detector decreases exponentially with increase in distance. A complete GEANT4 simulation was also carried out for this experimental set-up to calculate the average interaction length. This excellent match between the experimental data and the simulation provided us with the required confidence in GEANT4 simulation.

Next, a GEANT4 simulation was performed to estimate the average interaction length for the LAMBDA detector set-up. The interaction points of neutrons in the  $\text{BaF}_2$  material were found to decrease according to the relation  $\exp(-\mu x)$  where  $\mu = 0.13 \text{ cm}^{-1}$ . Using this distribution, the average interaction length of neutrons in the LAMBDA detector was estimated and found to be 7.6 cm when kept at a distance of 80 cm from the source. As a result, the energy resolution of neutrons at 4 MeV using equation (1) was found to be  $\pm 0.4 \text{ MeV}$ , corresponding to  $\delta T = 0.96 \text{ ns}$  (intrinsic time resolution of the detector). It has also been shown that the average interaction length remains almost constant for different neutron energies (1 – 10 MeV).

Finally, the LAMBDA spectrometer was employed in an in-beam-experiment

( $^4\text{He} + ^{93}\text{Nb}$ ) to measure the nuclear level density parameter by utilizing the neutron spectra detected in them. The experiment was performed at VECC, Kolkata using 35 MeV alpha beam from the K-130 cyclotron. A self-supporting foil of  $^{93}\text{Nb}$  (99.9% pure) with a thickness of  $\sim 1$  mg/cm<sup>2</sup> was used as the target. The compound nucleus  $^{97}\text{Tc}^*$  was populated at the initial excitation energy of 36 MeV. The experimental set-up was similar to that used for the efficiency measurement. The TOF technique was employed for neutron energy measurement in both the detectors ( $\text{BaF}_2$  array and BC501A detector) using the start trigger from the  $\gamma$ -multiplicity filter. The neutron energy spectra were extracted from the TOF spectra using the prompt gamma peak as a time reference. The angular momentum gated neutron energy spectra were compared with the statistical model calculation CASCADE to extract the nuclear level density parameter. The value of  $k$  was extracted from the experimental data by chi-square minimization technique (3–7 MeV). Interestingly, it has been observed that the values of  $k$  obtained from both the detector systems are very similar, indicating that the  $\text{BaF}_2$  detector can be efficiently used for the measurement of evaporated neutrons from an excited compound nucleus in an in-beam experiment along with its intended use in the measurement of high energy  $\gamma$ -rays.

In summary, the evolution of GDR width at very low temperatures (0.8 – 1.5 MeV) has been investigated, for the first time, in  $^{97}\text{Tc}$  nuclei below and above the critical temperature. This work infers that the GDR width remains constant up to a certain temperature and increases thereafter indicating that the GDR induced intrinsic fluctuation could play a decisive role in suppressing the GDR width at low temperatures. In this thesis, the LAMBDA spectrometer has also been used to study the nuclear level density parameter using neutron TOF spectra. Interestingly, the level density parameter obtained from the LAMBDA spectrometer are in good agreement with the value obtained from a known stan-

standard liquid scintillator based neutron detector, indicating that the LAMBDA spectrometer can also be efficiently used as a neutron detector.



# List of Figures

1.1	<i>Schematic representation of the GDR in atomic nuclei. . . . .</i>	4
1.2	<i>Schematic representation of various collective modes inside the nucleus with <math>L = 0</math> (monopole), <math>L = 1</math> (dipole) and <math>L = 2</math> (quadrupole) (adopted from thesis [Sup12b]). . . . .</i>	5
1.3	<i>Nuclear shape from GDR line shape. The strength function (<math>S_{GDR}</math>) directly gives the types of nuclear deformation. . . . .</i>	8
1.4	<i>[a] A typical high energy <math>\gamma</math>-ray spectrum (filled circles) from the decay of compound nucleus along with the CASCADE calculation (continuous line). Dashed line represents the bremsstrahlung contribution whereas dotted line represents the CASCADE calculation without bremsstrahlung component. [b] The GDR cross-section is Lorentzian in nature and its parameters. . . . .</i>	10
1.5	<i>Schematic diagram of Goldhaber-Teller and Steinwedel-Jensen dipole modes. For each cases, one half cycle of the vibration is shown as a function of time. . . . .</i>	11
1.6	<i>Microscopic picture of the GDR width built on excited states of atomic nuclei. The collective <math>1p</math>-<math>1h</math> state couples with the non-collective <math>1p</math>-<math>1h</math> state (<math>\Delta\Gamma</math>) and more complex <math>2p</math>-<math>2h</math>, <math>3p</math>-<math>3h</math>,.....<math>np</math>-<math>nh</math> configurations (<math>\Gamma_{\downarrow}</math>). It can also decay via particle emission (<math>\Gamma_{\uparrow}</math>). . . . .</i>	14
1.7	<i>Previous experimental data of GDR width at low temperatures with theoretical calculation (TSFM, CTFM) for <math>^{63}\text{Cu}</math>, <math>^{120}\text{Sn}</math> and <math>^{208}\text{Pb}</math>. (a) The filled circles are from Ref [Dee12a] while open circles are from Refs. [Kus98, Kic87]. (b) Our <math>^{119}\text{Sb}</math> data (filled circles) measured earlier [Sup12a] are shown along with the data of <math>^{120}\text{Sn}</math> (open circles [Bau98], open squares [Kel99], up triangle [Kus98], down triangle [Hec03a]). (c) <math>^{201}\text{Tl}</math> data (filled circles) [Dee12a] along with <math>^{208}\text{Pb}</math> [Bau98] data (open circles). The dashed lines correspond to the TSFM calculation while the continuous lines are the results of CTFM calculation. . . . .</i>	20
2.1	<i>Schematic diagram of compound nuclear decay. . . . .</i>	28

2.2	<i>The deformation probability distributions of the free energy surface in the <math>(\beta, \gamma)</math> plane for <math>^{97}\text{Tc}</math> nucleus at different temperatures. . . . .</i>	36
2.3	<i>Evolution of the equilibrium deformation, <math>\beta_{eq}</math> for <math>^{106}\text{Sn}</math> at <math>T = 1.8</math> MeV as a function of angular momentum <math>J</math>. The dashed line shows the value of <math>\Delta\beta</math> [Bor98]. . . . .</i>	40
2.4	<i>[Top Panel] The deformation due to GDR induced intrinsic fluctuation for different nuclei. [Bottom Panel] The temperature dependence of <math>\Delta\beta</math> for <math>^{97}\text{Tc}</math>, where <math>\Delta\beta</math> is the variance of the deformation due to thermal fluctuation of nuclear shape. . . . .</i>	42
2.5	<i>The GDR width as a function of temperature according to TSFM (Black dashed line), CTFM (Blue continuous line) and PDM (Green dot-dashed line) calculation. The red dotted line represent the TSFM calculation with shell effect. . . . .</i>	44
2.6	<i>The GDR line shapes at different temperatures calculated from Phonon Damping Model. . . . .</i>	45
3.1	<i>The LAMBDA spectrometer arranged in three <math>7 \times 7</math> matrix configurations. . . . .</i>	54
3.2	<i>The <math>\gamma</math>-multiplicity filter, split into two blocks of each 25 detectors arranged in <math>5 \times 5</math> matrix configurations. . . . .</i>	56
3.3	<i>Liquid organic scintillator (BC501A) based neutron time-of-flight detector array. . . . .</i>	57
3.4	<i>Detector geometry of the LAMBDA spectrometer arranged in <math>7 \times 7</math> matrix configuration using GEANT4 simulation code. The <math>\gamma</math>-rays are thrown isotropically to the front face of the spectrometer. . . . .</i>	59
3.5	<i>The GEANT4 simulated line shapes at <math>E_\gamma = 5, 10, 15, 20, 25</math> and <math>30</math> MeV for the LAMBDA array arranged in <math>7 \times 7</math> matrix configuration. . . . .</i>	60
3.6	<i>Detector geometry of the <math>\gamma</math>-multiplicity filter using GEANT4 simulation code. The <math>\gamma</math>-rays are thrown using the Landau distribution. . . . .</i>	63
3.7	<i>(a) Experimental fold distributions (filled circles) along with GEANT4 simulation (continuous line). (b) Angular momentum distribution for different folds (<math>F</math>). The continuous, dotted and dashed lines represent the angular distributions for <math>F=2, 3</math> and <math>4+</math>, respectively. The symbols with dash-dotted line represent the total incident distribution (<math>F \geq 2</math>). . . . .</i>	64
3.8	<i>Detector geometry of the liquid organic scintillator (BC501A) based neutron detector using GEANT4 simulation code. . . . .</i>	65

3.9	<i>Energy dependent intrinsic neutron detection efficiency for neutron detector. The symbols represent the experimental data using <math>^{252}\text{Cf}</math> source and the continuous line represent GEANT4 simulation. . . . .</i>	66
4.1	<i>Schematic diagram of experimental set-up for GDR studies. . . . .</i>	70
4.2	<i>Schematic diagram of electronics set-up for LAMBDA array and multiplicity filter. . . . .</i>	73
4.3	<i>Schematic diagram of electronics set-up for BC501A neutron detector.</i>	74
4.4	<i>The pulse shape discrimination and time-of-flight spectrum of liquid scintillator. . . . .</i>	75
4.5	<i>LAMBDA detector calibration using laboratory standard sources <math>^{22}\text{Na}</math> and <math>^{241}\text{Am}</math>-<math>^9\text{Be}</math>. The cosmic muons are used for high energy (23.1 MeV) calibration point. . . . .</i>	76
4.6	<i>A typical energy calibration curve obtained from a single <math>\text{BaF}_2</math> detector using low energy lab standard sources <math>^{22}\text{Na}</math> (0.511 MeV, 1.274 MeV) and <math>^{241}\text{Am}</math>-<math>^9\text{Be}</math> (4.43 MeV). The high energy (23.1 MeV) calibration point was taken by measuring the cosmic muons. . . . .</i>	77
4.7	<i>The experimental time-of-flight spectrum obtained from a single <math>\text{BaF}_2</math> detector of the LAMBDA array. The selection of prompt <math>\gamma</math>-band is shown with the filled region. . . . .</i>	78
4.8	<i>A two dimensional pulse shape discrimination spectrum. The selection of the <math>\gamma</math>-band is shown with continuous line. . . . .</i>	79
4.9	<i>The effect of different cuts and rejections on the raw high energy <math>\gamma</math>-ray spectrum. The red opened circles are the raw high energy <math>\gamma</math>-ray spectrum, black filled circles are PSD gated high energy <math>\gamma</math>-ray spectrum and blue filled circles are PSD and time gated high energy <math>\gamma</math>-ray spectrum. . . . .</i>	80
4.10	<i>The typical cosmic muon tracks in LAMBDA spectrometer arranged in <math>7\times 7</math> matrix. The direction of the muon tracks are shown by the arrows along with the actual energy deposits in the detector elements. . . . .</i>	82
4.11	<i>The cluster summing technique of the LAMBDA spectrometer arranged in a <math>7\times 7</math> matrix. The cluster is shown as a shaded rectangle (<math>3\times 3</math>, Yellow color) while the central detector of cluster is marked with pink color. . . . .</i>	83
4.12	<i>The high energy <math>\gamma</math>-ray spectra (filled circles) along with the statistical model CASCADE calculation (continuous line) for the system <math>^4\text{He} + ^{93}\text{Nb}</math> at four incident energies <math>E_{\text{lab}} = 28, 35, 42</math> and <math>50</math> MeV. Dashed line represents the bremsstrahlung contribution whereas dotted line represents the CASCADE calculation without bremsstrahlung component. . . . .</i>	84

4.13	<i>The high energy <math>\gamma</math>-ray spectra (filled circles) along with the statistical model CASCADE calculation (continuous line) for the system <math>{}^4\text{He} + {}^{93}\text{Nb}</math> at four incident energies <math>E_{lab} = 28, 35, 42</math> and <math>50</math> MeV. . . . .</i>	85
4.14	<i>Simulated angular momentum distributions for the system <math>{}^4\text{He} + {}^{93}\text{Nb}</math> at four incident energies <math>E_{lab} = 28, 35, 42</math> and <math>50</math> MeV. . . . .</i>	86
4.15	<i>The neutron energy spectra (filled triangles) measured using liquid organic scintillator (BC501A) based neutron detector along with the statistical model CASCADE calculation (continuous line) for the system <math>{}^4\text{He} + {}^{93}\text{Nb}</math> at four incident energies <math>E_{lab} = 28, 35, 42</math> and <math>50</math> MeV for different fold values. . . . .</i>	87
4.16	<i>Panels (a) to (d): The experimental linearized plots for the reaction <math>{}^4\text{He} + {}^{93}\text{Nb}</math> at projectile energies <math>28, 35, 42</math> and <math>50</math> MeV along with CASCADE predictions utilizing KRK (open circles with red dashed line) and IST (filled circles blue continuous line) level density formalisms. Panels (e) to (h): Same as above but utilizing BJK (open circles with green dotted-dashed line) and IST (filled circles with blue continuous line) level density formalisms. . . . .</i>	91
4.17	<i>Linearized plots of the measured <math>\gamma</math>-spectra (filled circles) and the best fitted CASCADE calculations (continuous lines) for different folds (F) at incident energies of <math>28, 35, 42</math> and <math>50</math> MeV. . . . .</i>	93
5.1	<i>Experimental GDR width (symbols) as a function of temperature along with the TSFM calculation. Dashed line without shell effect and dotted line with shell effect. . . . .</i>	98
5.2	<i>Experimental GDR width (symbols) as a function of temperature along with the CTFM calculation (continuous line). . . . .</i>	99
5.3	<i>Experimental GDR width (symbols) as a function of temperature along with the microscopic PDM calculation (dot-dashed line). . . . .</i>	101
5.4	<i>The average deformation measured from GDR width for <math>{}^{97}\text{Tc}</math> nucleus as a function of temperature with TSFM calculation (dashed line). . . . .</i>	102
5.5	<i>Experimentally measured GDR width (symbols) as a function of temperature with different theoretical predictions. The dotted line represents the TSFM calculation with shell effect whereas dashed line without shell effect, the continuous line represents CTFM calculation and dashed-dotted line represents the microscopic PDM calculation for <math>{}^{97}\text{Tc}</math>. . . . .</i>	103
6.1	<i>Schematic view of the experimental set-up for neutron studies using LAMBDA array. . . . .</i>	108

6.2	<i>[a]</i> TOF spectrum for one of the BaF <sub>2</sub> detectors in the array. <i>[b]</i> Neutron energy spectrum of the BaF <sub>2</sub> array (filled circle) compared with the expected neutron energy spectrum from <sup>252</sup> Cf (continuous line) [Knol]. . . . .	109
6.3	<i>[a]</i> Energy dependent neutron detection efficiency of BC501A detector. <i>[b]</i> Energy dependent neutron detection efficiency of BaF <sub>2</sub> array. Filled circles are the experimental data points and cross symbols represent GEANT4 simulation. <i>[c]</i> Neutron detection efficiency at different energy thresholds. . . . .	111
6.4	Experimental set-up for the measurement of average interaction length of neutrons in BaF <sub>2</sub> crystal. . . . .	113
6.5	Variation of the number of events as a function of distance corresponding to the number of detectors. Filled circles are the experimental data points and continuous line represents GEANT4 simulation . . . . .	113
6.6	Simulated average interaction length (symbols) of neutron in a 35 cm BaF <sub>2</sub> crystal at different incident energies . . . . .	114
6.7	<i>[Top panel]</i> Measured fold distribution along with the GEANT3 simulation fit. <i>[Bottom panel]</i> Angular momentum distribution for different folds for the <sup>4</sup> He + <sup>93</sup> Nb system . . . . .	116
6.8	<i>[a]</i> Experimental neutron energy spectra (open circles) of BC501A detector along with the CASCADE fit (continuous line) for different folds. <i>[b]</i> Experimental neutron energy spectra (open circles) of BaF <sub>2</sub> detector along with the CASCADE fit (continuous line) for different folds. . . . .	118



# List of Tables

3.1	<i>BaF<sub>2</sub> scintillator properties . . . . .</i>	51
3.2	<i>Merits and de-merits of BaF<sub>2</sub> scintillators (adopted from [Sup12b]) . . . . .</i>	52
4.1	<i>Average temperatures and average angular momenta along with level density parameters, GDR widths, centroid energies and bremsstrahlung parameters at different beam energies. . . . .</i>	95
6.1	<i>The values of <math>k</math> corresponding to different folds of BaF<sub>2</sub> and BC501A detectors. . . . .</i>	119



# Chapter 1

## Introduction

The atomic nucleus is a complex many body quantum system composed of nucleons bound by the strong interaction within a very small volume of dimensions  $\sim 10^{-15}$  m. Though very complex in nature, the nucleus is a very fascinating object and intense research in this field has provided useful applications in many fields e.g., nuclear medicine, imaging, dating in geology & archeology, power, weapons to name a few. In spite of tremendous advances in nuclear physics research many facets of the properties of the nucleus is still unknown.

A natural approach to explore the properties of the atomic nucleus is to excite it and measure the frequencies of the emitted electromagnetic radiations. The nuclear excitation is one of the finest and the most important tool to get a deep insight into the atomic nucleus viz., the single particle excitation and the collective excitation. In order to study the properties of nucleus or nuclear structure under extreme conditions of excitation energy, spin and iso-spin, the collective excitation modes come in handy as they enable one to study the nucleus in terms of macroscopic variables which in turn give a deeper insight into it.

Among all the collective modes, the giant dipole resonance is very special due to its unique properties. The high frequency, small amplitude collective mode of nuclei bears large resonance widths indicating large damping inside the

nuclear matter. The present thesis deals with these resonance phenomena and their damping mechanism within the nuclear system.

## 1.1 Giant resonances (GR)

Giant resonance is a collective mode of vibration of nucleons in a nucleus where all the nucleons take part. It can be viewed as a high frequency, damped and nearly harmonic shape vibration around the equilibrium shape of the nuclear system. It occurs in all nuclei starting from very light nuclei  ${}^4\text{He}$  to the very heavy nuclei  ${}^{238}\text{U}$ . The resonance energy is inversely proportional to the nuclear radius. The resonance is called ‘giant’ since it has large resonance width which indicates towards the large damping mechanism present within the nuclear system. The amplitude of this giant vibration is very small (a few percent of nuclear radius) because of large damping width (5–10 MeV) and the frequency of the vibration is very high ( $3 \times 10^{21}$ ). The nature of the giant resonance is Lorentzian which is characterized by three observables (Strength function, Centroid energy and width of the resonance) [Har01] which are discussed in section 1.4.

## 1.2 Classification of Giant resonances

In quantum mechanical terms, the resonance corresponds to a transition between the ground states and the collective states, which depends on the different quantum numbers such as multi polarity, spin and isospin. Giant resonances are generally classified according to their transferred multi polarity ( $\Delta L$ ), spin ( $\Delta S$ ) and isospin ( $\Delta T$ ) quantum number. The transition operators for the excitation of giant resonance are the electromagnetic operator which is, in long wavelength approximation ( $kr \ll 1$ ), given as [Har01, Sri08a]

$$O(L, M) = \int r^L Y_{LM}^* \rho d^3x \quad (1.1)$$

where  $L$  is the order of multi poles,  $Y_{LM}^*$  are the spherical harmonics,  $r$  is the radius of the nucleus,  $\rho$  is the charge density and  $k$  is the wave vector. The transition operator can be electric or magnetic depending on the spin quantum number. In the electric vibrational mode, no spin ( $\Delta S = 0$ ) is involved. The magnetic vibrational mode ( $\Delta S = 1$ ) involves the coordinated precession of the nucleon spins and thus the nucleus can acquire a net spin or net magnetic moment that oscillates at the precession frequency. Depending on the nuclear isospin quantum number ( $T$ ), the electric and magnetic GRs are further classified as isoscalar (IS) and isovector (IV) modes. In the IS mode ( $\Delta T = 0$ ), the neutron and proton fluids vibrate in phase whereas the IV mode ( $\Delta T = 1$ ) corresponds to their vibrations out of phase. The isoscalar and isovector mode of vibration can be excited for different multi polarities depending on the value of  $L$  such as monopole, dipole, quadrupole, etc.

$\Delta L = 0$  means the monopole vibration which is basically the radial vibration of the nucleus.  $\Delta L = 0, \Delta T = 0$  mode, the breathing mode, is the isoscalar giant monopole resonance (ISGMR). This “breathing mode” is of particular interest since its excitation energy is directly related to the incompressibility ( $K_A$ ) of the nucleus, which is a fundamental quantity of nuclear matter and important input parameter in the nuclear equation of state [Spe91].  $\Delta L = 0, \Delta T = 1$  correspond to the isovector giant monopole resonance (IVGMR) which is the compression modes of the nucleus that can be thought of as a compression and expansion of the whole nucleus which leads to a fluctuation of the nuclear radius. GMR is also studied very extensively.

$L = 1$  means the collective dipole vibration.  $\Delta L = 1, \Delta T = 0$ , the isoscalar

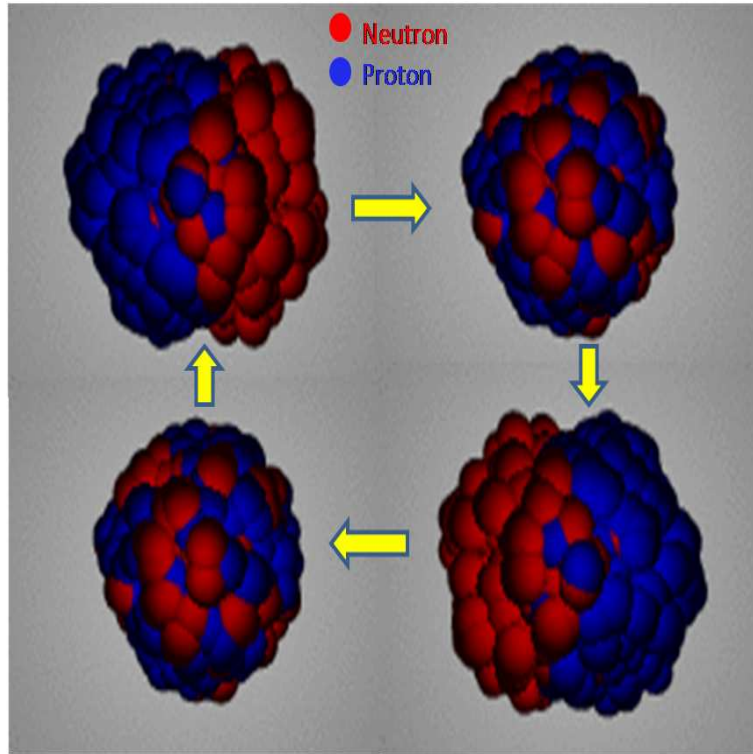


Figure 1.1: *Schematic representation of the GDR in atomic nuclei.*

giant dipole resonance mode is the translation of the nucleus as a whole, and this mode of excitation generally can not exist within the nucleus.  $\Delta L = 1$ ,  $\Delta T = 1$  is the isovector giant dipole resonance (IVGDR) mode in which the neutrons and protons oscillate out of phase against each other. The IVGDR mode is the most cleanly observed and best known of the various giant resonance modes.

$L \geq 2$  represents the shape vibration of the nucleus.  $L = 2$  represents the quadrupole vibration which means a change in electric quadrupole moment of the nucleus. A pictorial representation of the different collective vibration is shown in Fig 1.2. The resonance energy of the GR can be well described by  $A^{-1/3}$  dependence, where  $A$  is the mass number and the proportionality constant being equal to about 79 MeV for GDR, 80 MeV for GMR, 65 MeV for isoscalar giant quadrupole resonance (ISGQR) and 140 MeV for isovector

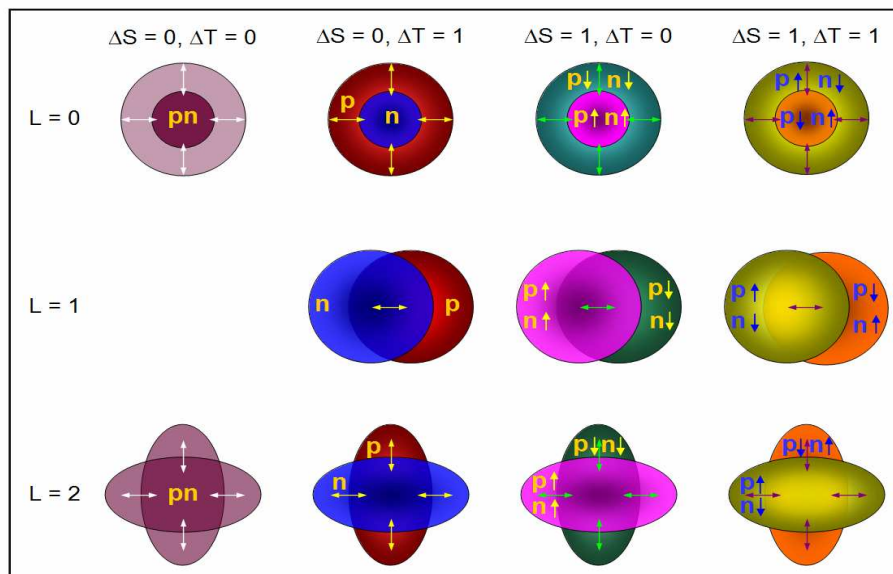


Figure 1.2: Schematic representation of various collective modes inside the nucleus with  $L = 0$  (monopole),  $L = 1$  (dipole) and  $L = 2$  (quadrupole) (adopted from thesis [Sup12b]).

giant quadrupole resonance (IVGQR) [Har01]. This thesis deals with the study of IVGDR built on excited states, mainly focussing on the evolution of IVGDR width at very low temperatures ( $T = 0.8\text{--}1.5$  MeV).

### 1.3 Isovector giant dipole resonance (IVGDR)

The first experimental evidence for the giant resonance type phenomenon was observed in 1937 in the measurements of the radioactivity produced in variety of targets by a source of 14 MeV photons from  $\text{Li}(p, \gamma)$  reactions [Bot37]. They observed an increase in experimental cross sections compared to the averaged theoretical cross sections, which led to the conclusion of strong resonance absorption in those nuclei. Later on (In 1947), Baldwin and Klaiber conducted photo absorption experiments at higher excitation energies that also showed the resonance behavior [Bal47]. These resonances were found to exhibit electric dipole character which means an out of phase vibration of neutron and proton

fluids in a spatial dipole pattern and hence named as giant dipole resonance. The isovector giant dipole resonance (IVGDR) is the best known giant resonance due to the fact that the IVGDR has a very specific decay ( $\gamma$ -decay) mode with the highest probability compared to other higher multi polar modes. The spin-parity of these resonance states are  $1^-$  and they lie at the energy  $\sim 80A^{-1/3}$  MeV [Har01]. The phenomena of GDR can be classified into two categories, the cold GDR i.e GDR built on ground state and the hot GDR i.e GDR built on excited states of atomic nuclei.

### 1.3.1 IVGDR built on ground state

The GDR built on ground state means all the available excitation energy transferred to the nucleus goes into the GDR vibration. This was studied historically via photon-absorption process where a beam of monochromatic photons is illuminated on the target nucleus and the absorbed frequencies are determined through  $(\gamma, n)$  reaction channels [Bot37]. In this case, the wavelength of the photon ( $\lambda \approx 100$  fm) exciting the vibration is large compared to the diameter of the system ( $R = 5-7$  fm). Hence, all the protons experience a time dependent, uniform electric field and move in the same direction under the influence of the field. Since in the photo-absorption process, the center of mass of the nucleus is at rest or in uniform motion, the neutrons, although unaffected by the field have to move in opposite direction. The strong force acting among the nucleons provides the restoring force of this vibrational mode.

### 1.3.2 IVGDR built on excited state

The GDR built on excited states implies that the GDR is actually built on one of the excited states of atomic nuclei. In this case, the nucleus remains in excited states and oscillates collectively. David Brink first suggested that the GDR can be populated on any excited state of atomic nucleus [Bri55]. The

first evidence of GDR built on excited states in favour of Brink hypothesis was found in 1974, during the study of high energy  $\gamma$ -rays from the fission fragments in spontaneous fission of  $^{252}\text{Cf}$  [Die74]. The existence of GDR built on excited states using a reaction study was first observed in a proton capture ( $p,\gamma$ ) experiment on  $^{11}\text{B}$  [Kov79] where the GDR built on first excited states of  $^{12}\text{C}$  was observed. For studying the GDR built on excited states, one must excite the nucleus and then measure the frequencies of the photons it emits during the de-excitation of the nucleus. There are two experimental methods to study the GDR built on excited states. First one is the nuclear fusion reactions where a large amount of excitation energy and angular momentum can be imparted to the compound nucleus. In these reactions, a compound nucleus is formed at high excitation energy with a broad angular momentum distribution. Another one is the inelastic scattering of light/heavy ion on a target where the excitation energy would be large but the populated angular momentum would be relatively low. In analogy to the cooling process, the hot nucleus de-excites via particle evaporation (neutron, proton, alpha etc). In competition with the particle emission, the system can also decay by high energy ( $> 8$  MeV)  $\gamma$ -emission with a much smaller probability, of the order  $10^{-3}$  -  $10^{-5}$ . This high energy  $\gamma$ -rays are emitted due to the decay of giant dipole resonance. Experimentally, these  $\gamma$ -rays appear as a prominent bump around 10–25 MeV in the energy spectrum, riding over the exponentially decreasing statistical  $\gamma$ -rays (as shown in Fig 1.4a).

### 1.3.3 High energy $\gamma$ -ray spectrum from the decay of GDR built on excited state

The high energy  $\gamma$ -ray spectrum from an excited compound nucleus can be divided into different regions in terms of  $\gamma$ -ray energies. A high energy  $\gamma$ -ray spectrum of  $^{97}\text{Tc}$  compound nucleus is shown in Fig 1.4a. The spectrum for 4

$< E_\gamma < 10$  MeV is mainly dominated by the statistical E1  $\gamma$ -rays emitted from the decay of the excited compound nuclei below the particle threshold line. The exponentially decaying slope of the spectrum is due to the fact that the  $\gamma$ -decay probability decreases approximately exponentially with increasing  $E_\gamma$  [ $P(E_\gamma) \propto e^{-E_\gamma/T}$ ]. For  $E_\gamma > 10$  MeV, a broad bump is observed which is the signature of the GDR decay. Above  $E_\gamma = 25$  MeV, the slope of the spectrum changes and is mainly dominated by the bremsstrahlung  $\gamma$ -rays due to the nucleon-nucleon collisions during the early stages of the compound nucleus formation.

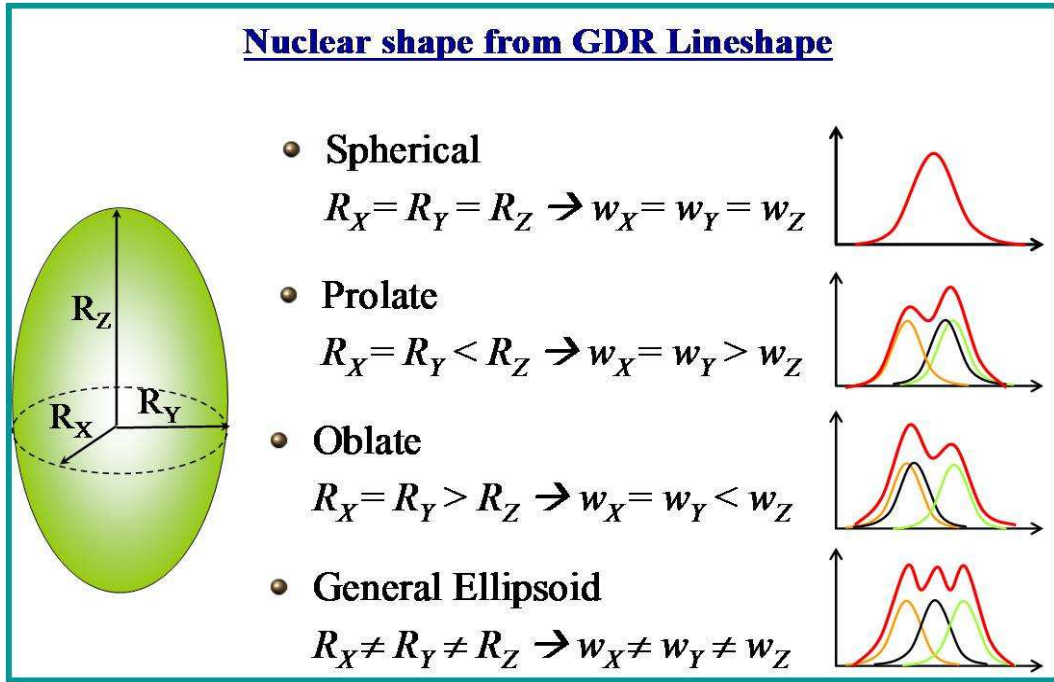


Figure 1.3: Nuclear shape from GDR line shape. The strength function ( $S_{GDR}$ ) directly gives the types of nuclear deformation.

## 1.4 Parameters for characterizing the GDR vibration

Like any other damped oscillation, the GDR excitation function  $\sigma_{GDR}(E_\gamma)$  is Lorentzian in shape and characterized by three parameters : Centroid energy

( $E_{GDR}$ ), width of the resonance ( $\Gamma_{GDR}$ ) and strength function ( $S_{GDR}$ ). The excitation function of the GDR is given by

$$\sigma_{abs}(E_\gamma) = \frac{\sigma_m \Gamma_{GDR}^2 E_\gamma^2}{(E_\gamma^2 - E_{GDR}^2)^2 + \Gamma_{GDR}^2 E_\gamma^2} \quad (1.2)$$

where  $\sigma_m$  is the peak cross section.

### 1.4.1 Strength function $S_{GDR}$

The strength of the resonance is given by

$$S_{GDR} = \int_0^\infty \sigma_{abs}(E_\gamma) dE_\gamma \quad (1.3)$$

The GDR strength function is directly coupled to the nuclear shape degrees of freedom and therefore can be used to probe the nuclear deformation (as shown in Fig 1.3). In case of spherical nuclei, the vibrations along all three axes are identical and correspond to a single Lorentzian strength function. However, in case of deformed nuclei the vibration along each axis will have a different energy corresponding to different axial dimensions leading to more than one component in GDR line shape. For example, in a prolate or oblate system there will be two components. The separation between these various components and their relative strengths directly provides quantitative information of the nuclear shape. On the other hand, the strength function is a very useful benchmark to check whether a resonance qualifies as giant resonance or not. The parameter  $S_{GDR}$  is basically the area subtended by the Lorentzian curve and thus gives the total resonance cross-section. The number of nucleons participating in the collective vibration can be obtained by comparing the experimentally obtained cross-section to the theoretical limit, known as Thomas-Reiche-Kuhn (TRK) sum rule given by  $\sim 60NZ/A$  [Sno86], where N, Z and A are neutron, proton and mass number, respectively. If the experimentally observed resonance exhaust

a major part ( $> 50\%$ ) of the corresponding sum rule, then it is called a giant resonance [Har01]. Here, it has been observed that the dipole vibration exhausts essentially 100% of the oscillator strength which confirms that all the nucleon participate in the collective dipole vibration.

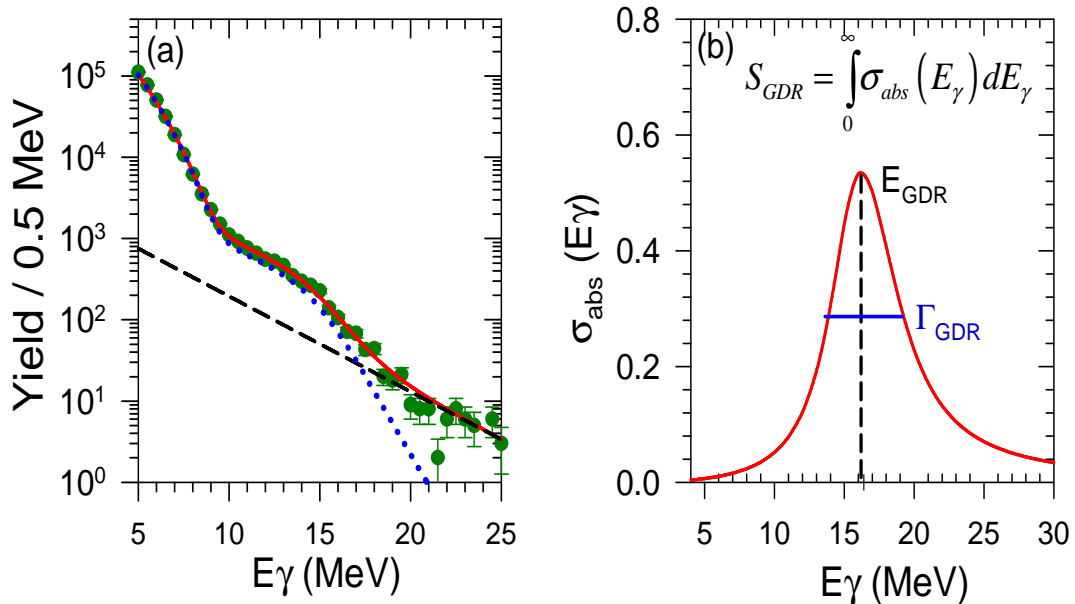


Figure 1.4: [a] A typical high energy  $\gamma$ -ray spectrum (filled circles) from the decay of compound nucleus along with the CASCADE calculation (continuous line). Dashed line represents the bremsstrahlung contribution whereas dotted line represents the CASCADE calculation without bremsstrahlung component. [b] The GDR cross-section is Lorentzian in nature and its parameters.

#### 1.4.2 Resonance energy, $E_{GDR}$

The centroid energy of the resonance is inversely proportional to the nuclear radius and provides an idea about the nuclear size. Moreover, the centroid energy is strongly correlated with the nuclear symmetry energy, which is a fundamental quantity for studying the properties of a highly asymmetric nuclear medium e.g the structure of a neutron star [Tri08]. Macroscopically, the systematics of centroid energy of the GDR built on ground state of the nucleus, is generally expressed as a combination of two different mechanisms of vibration as given by

two theoretical models, Goldhaber-Teller (GT) [Gol48] and Steinwedel-Jensen (SJ) [Ste50] model, given by  $E_{GDR} = 31.8A^{-1/3} + 20.6A^{-1/6}$ .

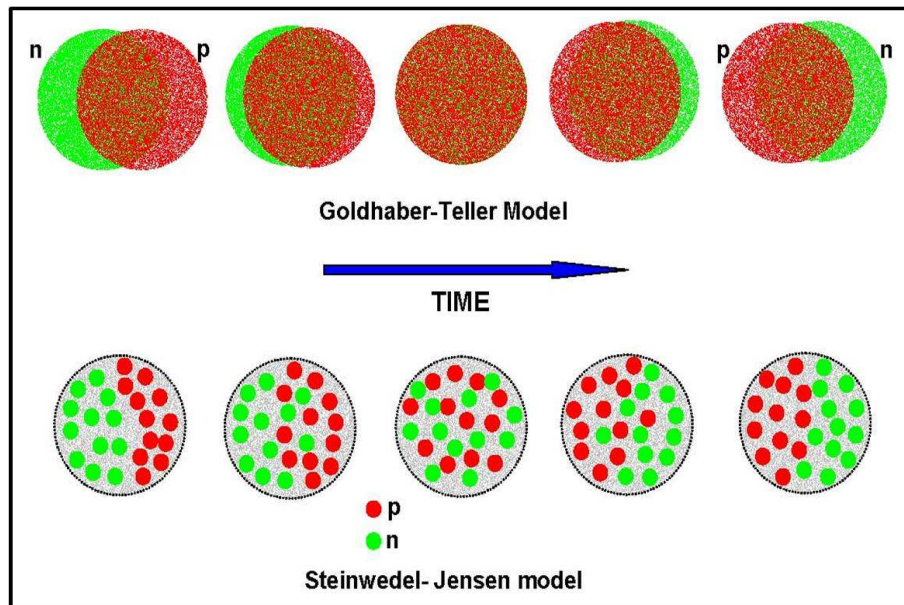


Figure 1.5: Schematic diagram of Goldhaber-Teller and Steinwedel-Jensen dipole modes. For each cases, one half cycle of the vibration is shown as a function of time.

Steinwedel-Jensen (SJ) model assumes that the nucleus is like a resonating cavity [Ste50]. Motion of neutrons and protons cause density changes in the neutron and proton field. The restoring force per unit mass will be proportional to the gradient of these densities. Therefore, for a given displacement the density change is inversely proportional to the nuclear radius  $R$  and the gradient will be proportional to  $1/R^2$ . Thus, the frequency of the density vibration is proportional to  $1/R$  and thus to  $A^{-1/3}$ .

Goldhaber-Teller (GT) Model assumes that the neutrons and protons are two separate rigid interpenetrating distributions [Gol48]. During the dipole vibration, they undergo harmonic motions with respect to each other. The restoring force of this harmonic vibration will be proportional to surface area, i.e  $R^2$ . The frequency of the vibration will be proportional to  $\sqrt{(F/A)}$  and hence

to  $A^{-1/6}$ . Thus, the centroid energy of the GDR built on ground state of the nucleus, is expressed as the combination of the above two model description and is given by  $E_{GDR} = 31.8A^{-1/3} + 20.6A^{-1/6}$  [Gaa92]. The schematic diagrams of Goldhaber-Teller and Stenwedel-Jensen dipole modes are shown in Fig 1.5.

Microscopically, the GDR can be viewed as a coherent superposition of non-collective 1 particle-1 hole configurations, known as collective particle-hole doorway resonance state [Wil56]. The term doorway implies that the excited nucleus passes from the entrance channel through the doorway state before the full complexity of the compound nuclear states are populated. The energy for this 1p-1h excitation is  $\sim 41A^{-1/3}$ . However, the experimental systematic show twice of this value i.e  $80A^{-1/3}$ . This difficulty was overcome by Brown and Bolsterli [Bro59] who suggested that the residual p-h interaction has to be taken into account in describing such configurations.

### 1.4.3 Width of the resonance, $\Gamma_{GDR}$

One of the basic problems in the study of giant dipole resonance is the understanding of how the collective vibration of nucleons (GDR vibration) get damped. The width of the GDR is a very special observable as it gives an idea about the damping mechanism of the GDR vibration and has been the focus of many experimental and theoretical studies for last few decades. The width of the resonance arises due to the transfer of energy from the orderly vibration into other modes of nuclear motion. The typical value of the GDR width for heavy nuclei is  $\sim 5$  MeV implying that the vibration is completely damped after a few vibrations. The general trend of the GDR width as observed from the experimental results shows that it is smallest for the closed shell nuclei,  $\sim 4$  MeV for nuclei around  $^{90}\text{Zr}$  and  $^{208}\text{Pb}$ , and increases to 5-6 MeV for nuclei between shells. The present thesis is related to the GDR width and its evolution as a

function of temperature. The details of the origin of GDR width, experimental observation and theoretical explanation are discussed as below.

## 1.5 Origin of the GDR width

### 1.5.1 Macroscopic description

Macroscopically, the large GDR width built on ground state is mainly caused by two processes, which are collisional damping and in-homogeneous damping. Collisional damping occurs due to the binary collisions between nucleons and collisions between a nucleon & the nuclear surface. In the binary collision between two nucleons, a nucleon can change its state of motion by promoting a particle in the Fermi sea into a state above the Fermi surface. Since the particle-particle correlations are considerable larger than the particle-hole correlations and Pauli blocking is more effective in the bulk than in the nuclear surface, the probability of nucleon-nucleon collision (2-body collision) is negligible compared to the nucleons colliding with the nuclear surface. Thus, the nuclear surface plays a central role in the collisional damping process. On the other hand, inhomogeneous damping occurs due to the deformation of the nucleus. If the ground state of the nucleus is deformed, there is a possibility of nucleons vibrating along the different principle axes, producing different centroid energy components. Thus, the GDR line shape splits according to the dimension of different principle axes producing a large width [Bor98].

### 1.5.2 Microscopic description

Microscopically, the GDR can be described as a coherent superposition of the non-collective 1p-1h configuration [Wil56] and it is found to have large width even if it is built on the nuclear ground state. The width mainly comprises of three different parts: Landau width ( $\Gamma_{landau}$ ), Escape width ( $\Gamma^\dagger$ ) and the

spreading width ( $\Gamma^\downarrow$ ) in general [Har01], and is given by

$$\Gamma_{GDR} = \Gamma_{landau} + \Gamma^\uparrow + \Gamma^\downarrow \quad (1.4)$$

The Landau width ( $\Gamma_{landau}$ ) arises owing to the coupling of collective 1p-1h state (GDR state) with the non-collective 1p-1h configuration in the same excitation energy range.

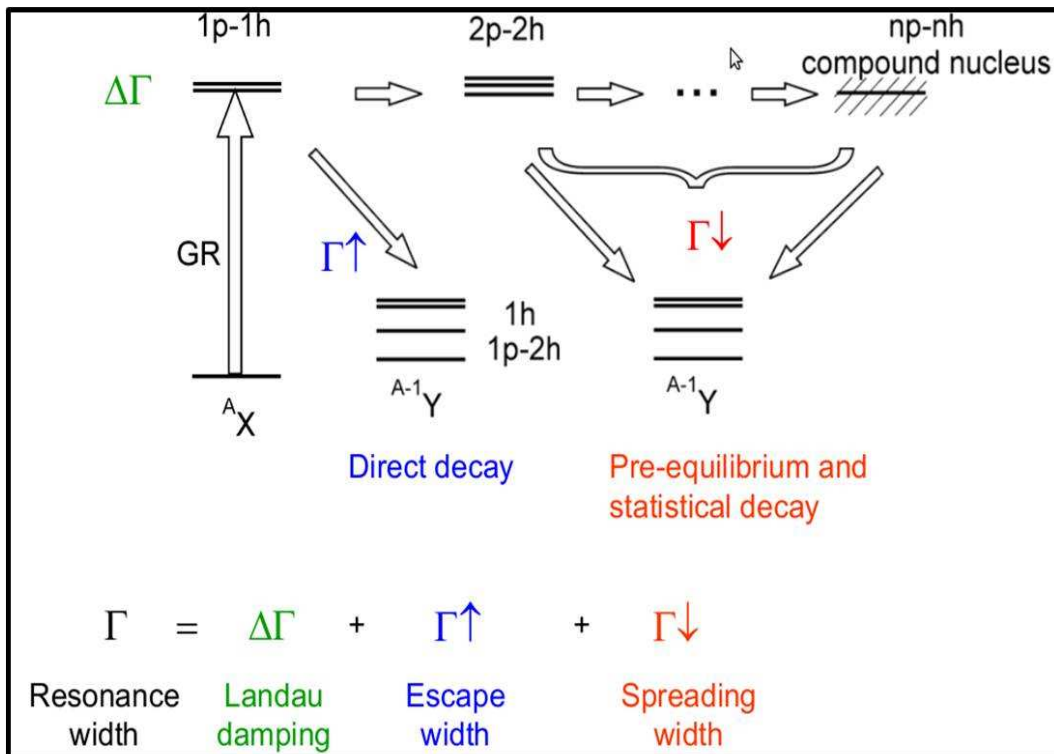


Figure 1.6: Microscopic picture of the GDR width built on excited states of atomic nuclei. The collective 1p-1h state couples with the non-collective 1p-1h state ( $\Delta\Gamma$ ) and more complex 2p-2h, 3p-3h,.....np-nh configurations ( $\Gamma^\downarrow$ ). It can also decay via particle emission ( $\Gamma^\uparrow$ ).

The Escape width ( $\Gamma^\uparrow$ ) arises due to coupling of GDR state to the continuum. This is because the GDR state remains above the particle threshold line and it can directly decay to state in the daughter nuclei and attain the escape width. For heavy nuclei, it comprises mainly of neutron decay width and for light nuclei the charged particle decay width has also to be taken into account.

The spreading width ( $\Gamma^\downarrow$ ) arises due to the coupling of coherent 1p-1h state with more complex and numerous 2p-2h configuration which have the same spin and parity. The resulting state can also be coupled to more complex 3p-3h, 4p-4h,.... np-nh states till a completely equilibrated system is reached. In medium and heavy nuclei, it turns out that the escape and landau widths only account for a small fraction and the major contribution of the large resonance width comes from the spreading width. Recently, an empirical formula has been derived for the spreading width with only one free parameter by separating the deformation induced widening from the spreading effect, and is expressed as  $\Gamma^\downarrow = 0.05E_{GDR}^{1.6}$  [Jun08]. The microscopic description of GDR width has been displayed in Fig 1.6 schematically.

## 1.6 Evolution of GDR width built on excited states of atomic nuclei

### 1.6.1 Experimental observation

In the past few decades, a lot of experiments have been performed to study the evolution of GDR width as a function of temperature (T) and angular momentum (J) of the system. These experiments and their results are discussed in this section.

In 1981, Drapper et al., [Dra82] first suggested the excitation energy dependence of GDR properties. They performed an experiment of 1150 MeV  $^{136}\text{Xe}$  beam on  $^{181}\text{Te}$  target. They suggested that the 10–20 MeV  $\gamma$ -ray spectra at low excitation energy are reproduced by theoretical calculation using the ground state value of resonance energy and resonance width, but at high excitation energy the better agreement is obtained with a smaller resonance energy and increasing the resonance width.

In 1983, Germann et al., [Ger83] studied the spectral line shape of  $\gamma$ -rays

emitted from  $^{76}\text{Kr}$ ,  $^{63}\text{Cu}$  and  $^{127}\text{Cs}$  to study the J-dependence of line shape. But they could not find any J-dependence of line shapes because the populated angular momenta were very low.

In 1984, Gaardhoje et al., [Gaa84] observed the increase of GDR width with excitation energy. They populated  $^{108}\text{Sn}$  nuclei at excitation energy  $E^* = 51$  and  $61$  MeV and obtained  $\Gamma_{GDR} = 6$  and  $6.5$  MeV, respectively. The same group in 1986, studied the GDR  $\gamma$  decay from  $^{111}\text{Sn}$  nuclei populated at excitation energy  $E^* = 66$  and  $110$  MeV and extracted  $\Gamma_{GDR} = 7.5$  and  $11$  MeV, respectively [Gaa86].

In 1987, Chakraborty et al., [Cha87] studied the excitation energy dependence of GDR width in  $^{110}\text{Sn}$ ,  $^{112}\text{Sn}$  nuclei. They found that the GDR width increases almost quadratically up to the highest excitation energy. This group also suggested an empirical formula to explain the excitation energy dependence of GDR width which is  $\Gamma_{GDR} = 4.8 + 0.0026E_{GDR}^{1.6}$ , where  $4.8$  is the ground state GDR width. In 1988, Chakraborti et al., [Cha88] gave a new parametrization  $\Gamma_{GDR} = 4.5 + 0.0004E_{GDR}^2 + 0.003J^2$  and included it within the statistical model code CASCADE, instead of taking GDR width as a free parameter.

In 1989, Bracco et al., [Bra89] populated  $^{110}\text{Sn}$  nuclei at  $E^* = 230$  MeV for measuring the GDR width at very high excitation energy and found an abrupt change in the smooth dependence of GDR width with excitation energy. They measured the GDR width at  $E^* = 230$  MeV in this mass region which is similar the one observed at  $E^* = 130$  MeV, indicating the onset of saturation effect above  $130$  MeV, which correspond to  $T \sim 2.5$  MeV. Further evidence of saturation effect at very high excitation was also obtained by Enders et al., [End92] in 1992 and Hofmann et al., [Hof94] in 1994.

In 1992, Kasagi et al., [Kas92] performed an experiment at RIKEN, Japan

by populating the nuclei  $^{132}\text{Ce}$  and observed that the GDR width increased from 8 to 13 MeV due to the increase of  $E^*$  from 80 to 120 MeV.

In 1994, Noormann et al., [Noo94] studied the angular momentum dependence of GDR width in the temperature domain  $1 \leq T \leq 1.6$  MeV. They measured the GDR  $\gamma$ -rays emitted from the compound nucleus  $^{154}\text{Dy}$  populated at an excitation energy of 69 MeV in three angular momentum windows  $\langle J \rangle = 31, 42$  and  $50 \hbar$  and showed that the GDR width increased with increasing angular momentum.

In 1996, Viesti et al., [Vie96] did an experiment by employing a high resolution  $4\pi$   $\gamma$ -ray spectrometer to select the spin region in the fusion evaporation reaction ( $^{64}\text{Ni} + ^{92}\text{Zr}$  @  $E_{lab} = 241$  MeV) forming the excited  $^{156}\text{Er}$  nuclei. They also showed that the GDR width increased with increasing angular momentum.

The above experimental investigations were performed mostly using the heavy ion fusion reactions where the compound nuclei are populated at very high excitation energy with broad angular momentum distributions. These experimental data showed that the GDR width increased up to  $\Gamma_{GDR} = 11$  MeV when the excitation energy increases up to  $E^* = 130$  MeV. This increase was interpreted as arising from the change of nuclear shape deformation induced by the combined effect of temperature and angular momentum. In order to understand their individual effect on GDR width, these two effects must be separated and measurement should be carried out at fixed temperature for different angular momenta, and for different temperatures at fixed (or low) angular momentum.

In 1995, Bracco et al., [Bra95] studied the GDR width and angular distributions as a function of angular momentum at an approximately constant temperature  $T \sim 1.8$  MeV, in order to see only the angular momentum effect

on GDR width. They populated  $^{109,110}\text{Sn}$  nuclei by fusion evaporation reaction at excitation energy  $E^* = 80,92$  MeV and at the angular momentum region  $40 - 54 \hbar$ . They found that the GDR width increased from 10.8 to 12.8 MeV due to increase of angular momentum from 40 to  $54 \hbar$

In 1996, Ramakrishnan et al., [Ram96] performed a pioneering experiment to decouple the effects of angular momentum and temperature on GDR width through inelastic scattering of  $\alpha$  particles at 30 and 40 MeV/nucleon. They populated  $^{120}\text{Sn}$  nuclei in the excitation energies range of 30 – 130 MeV and at very low angular momentum states ( $\langle J \rangle = 15 \hbar$ ). Because of the low angular momentum populated, it was possible to study the variation of GDR width with excitation energy without having any significant effect of  $J$ .

From the experimental results of Bracco et al., [Bra95] and Ramakrishnan et al., [Ram96], it was clear that at low angular momentum the GDR width is controlled by the temperature induced effect and at high angular momentum the GDR width is controlled by the angular momentum effect. It seems that at particular temperature, the angular momentum effects begin to be important only above a certain value. The experimental confirmation of this hypothesis required a large number of experimental data and it was later confirmed by several works.

In 1997, Mattiuzzi et al., [Mat97] measured the GDR width in  $^{106}\text{Sn}$  nuclei at  $E^* = 80$  MeV ( $T \sim 2$  MeV) and for average spin values of 24 and  $36 \hbar$ . These results, together with the previous existing exclusive measurements in the same excitation energy and mass region, confirmed that the GDR width is roughly constant up to spin  $J \leq 35 \hbar$  for Sn mass region and thereafter increases with the angular momentum.

In 1998, Baumann et al., [Bau98] studied the evolution of the giant dipole

resonance in  $^{120}\text{Sn}$  and  $^{208}\text{Pb}$  nuclei at excitation energies in the range of 30 – 130 MeV and 40 – 110 MeV, respectively through inelastic scattering of  $\alpha$  particles. They showed that the width increases from 5.5 MeV to 12 MeV for the temperature range of 1.2 – 3.1 MeV in case of  $^{120}\text{Sn}$  nuclei and the width increases from 5.7 – 8.0 MeV for the temperature range of 1.3 – 2.0 MeV in case of  $^{208}\text{Pb}$  nuclei. They concluded that the observed width increase was attributed to thermal fluctuation of nuclear shape and the angular momentum does not have any effect on GDR width because of low angular momentum populated in the nuclei.

In 1999, Kelly et al., [Kel99] did an interesting experiment by populating  $^{118}\text{Sn}$  nuclei using  $^{18}\text{O}$  as beam and  $^{100}\text{Mo}$  as target. They pointed out that at higher bombarding energies ( $E_{lab} > 5$  MeV/nucleon), pre-equilibrium effects come into picture which substantially lowers the average excitation energy and hence the nuclear temperature. They measured the corresponding loss of excitation energy of the compound nucleus due to pre-equilibrium particle emissions. Their detailed measurements along with the re-analysis of previous experimental results, showed that the GDR width does not saturate at  $T > 2.5$  MeV but continues to increase up to temperatures of  $T \sim 3.2$  MeV. Later, in 2006, Wieland et al., [Wie06] did an experiment by populating highly excited  $^{132}\text{Ce}$  compound nucleus through heavier target-projectile combinations where pre-equilibrium effects were very small and found that the GDR width does not saturate but increases steadily with temperature of at least up to 4 MeV. At very high temperatures ( $T > 4$  MeV), Gaardhoje et al., [Gaa87] observed the lower  $\gamma$ -ray yield from GDR decay which signified the quenching of GDR at very high temperature and suggested that there might be loss of collectivity within the nucleus. This quenching of  $\gamma$ -ray yield with increasing  $E^*$  was also observed by Faou et al., [Fao94] when they studied GDR  $\gamma$ -rays emitted from

hot nuclei of  $A \sim 115$  and  $E^*$  between 350 to 500 MeV.

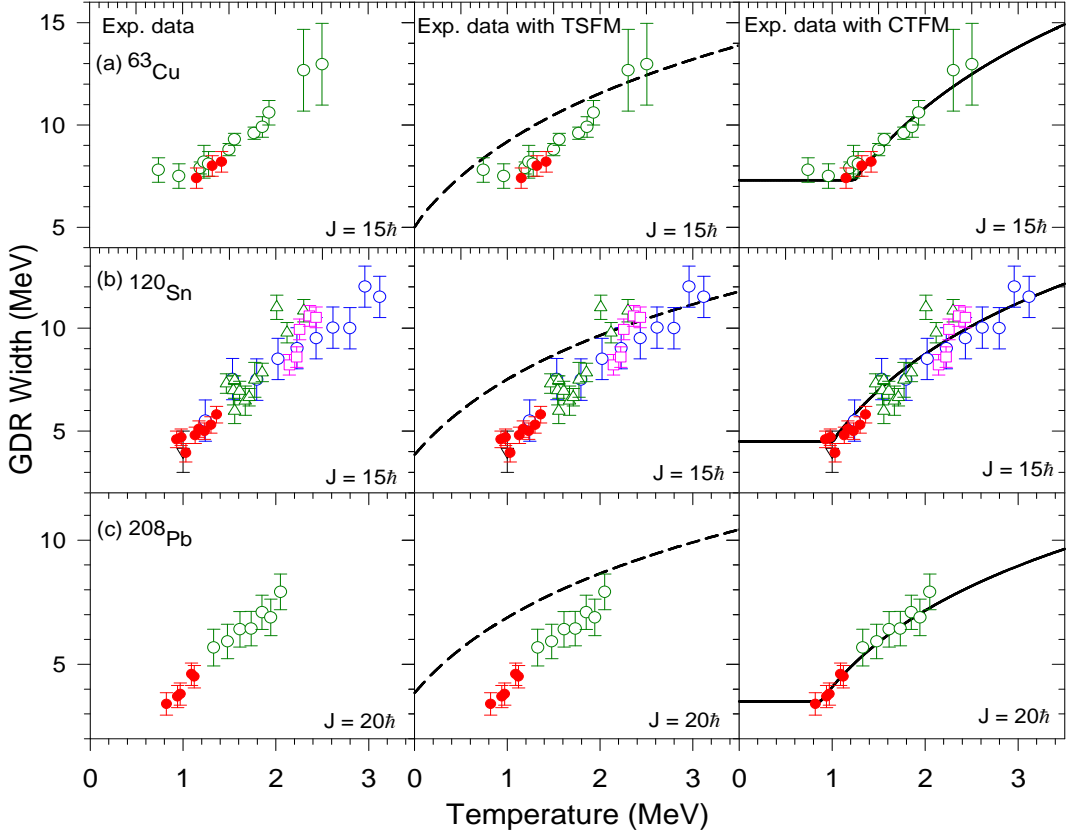


Figure 1.7: Previous experimental data of GDR width at low temperatures with theoretical calculation (TSMF, CTFM) for  $^{63}\text{Cu}$ ,  $^{120}\text{Sn}$  and  $^{208}\text{Pb}$ . (a) The filled circles are from Ref [Dee12a] while open circles are from Refs. [Kus98, Kic87]. (b) Our  $^{119}\text{Sb}$  data (filled circles) measured earlier [Sup12a] are shown along with the data of  $^{120}\text{Sn}$  (open circles [Bau98], open squares [Kel99], up triangle [Kus98], down triangle [Hec03a]). (c)  $^{201}\text{Tl}$  data (filled circles) [Dee12a] along with  $^{208}\text{Pb}$  [Bau98] data (open circles). The dashed lines correspond to the TSMF calculation while the continuous lines are the results of CTFM calculation.

In 2003, Rathi et al., [Rat03a] observed that the experimental GDR width was almost constant with increasing  $J$  at a particular temperature but increased with increasing temperature for a particular angular momentum, for the study of GDR width in excited  $^{86}\text{Mo}$  nuclei. In the same year, Heckmann et al., [Hec03a] did an another inelastic scattering experiment and extracted  $\Gamma_{\text{GDR}} = 4$  MeV at  $T = 1$  MeV in the decay of  $^{120}\text{Sn}$  nuclei. This was the lowest finite-

temperature GDR width measurement at that time. Surprisingly, the extracted GDR width shows almost same value as that of the ground state.

In 2008, Srijit Bhattacharya et al., [Sri08b] measured the angular momentum gated GDR width at low temperatures ( $T \leq 2$  MeV) and high angular momentum ( $J = 49 - 59 \hbar$ ) on  $^{113}\text{Sb}$  nuclei. They observed that the GDR width increased with increasing temperature (or angular momentum) for a given angular momentum (or temperature). There is an extensive compilation of GDR parameters built on excited states for  $A=39-240$  by A Schiller and M Thoennessen in Ref [Sch07].

Until now, there are very few experimental data on the measurement of GDR width at low temperature ( $T < 1.5$  MeV). Experimentally, the measurement of GDR width at low temperature ( $T < 1$  MeV) is a very complex and challenging problem due to the difficulties in populating the nuclei at low excitation energies. Previously, the low temperature measurements were performed through inelastic scattering of lighter projectile by heavier target with a disadvantage of getting imprecise excitation energies with an uncertainty about 10 MeV. The heavy ion induced fusion reactions are limited to the excitation at higher temperature due to presence of Coulomb barrier in the entrance channel and are always associated with broad  $J$  distributions. Recently, at the Variable Energy Cyclotron Centre (VECC), Kolkata, India, exclusive experiments were performed using the alpha beams to investigate the low temperature region [Sup12a, Dee12a]. The previous experimental data at low temperatures are shown in Fig 1.7. It has been shown that the effect of  $T$  and  $J$  becomes noticeable only above a critical angular momentum ( $J_c = 0.6A^{5/6}$ ) and  $T \sim 1$  MeV, and after that the GDR width increases with increase in  $J$  and  $T$ . Till now, there are no experimental data at low temperatures in  $A \sim 100$  mass region. This thesis deals with the measurement of GDR width at very low temperatures

for  $^{97}\text{Tc}$  nuclei.

### 1.6.2 Theoretical explanation

Along with the experimental efforts, a number of theoretical approaches have been proposed to demonstrate the behavior of GDR width as a function of  $T$  and  $J$ . Microscopically, the increase of GDR width as a function of  $T$  is described reasonably well within the Phonon Damping Model (PDM) [Dan98]. The PDM calculates the GDR width and the strength function directly in the laboratory frame without any need for an explicit inclusion of thermal fluctuation of nuclear shapes. According to PDM, the increase of GDR width with  $T$  is due to the coupling of GDR phonons to the incoherent particle-particle, hole-hole and particle-hole configurations, which appears due to the distortion of the Fermi surface at finite  $T$ . This model can predict the data at low temperature as well as the saturation of GDR width at higher temperature by including the thermal pairing fluctuation.

On the other hand, the macroscopic Thermal Shape Fluctuation Model (TSFM) [Alh88] is based on the fact that large amplitude thermal fluctuations of nuclear shape play an important role in describing the increase of GDR width as a function of  $T$ . According to TSFM, at finite temperature, the nucleus does not have any particular shape, rather it will be an weighted average of all possible shapes and orientations. The nuclear shape fluctuates around the equilibrium deformation and this fluctuation increases with increase in temperature. As a result, the GDR line shape will also be a superposition of line shapes due to all possible nuclear shapes and thus producing a larger width. Therefore, the GDR width has been found to increase monotonically with temperature. The basic assumption (adiabacity) of this model is that the nuclear shape does not change during the time GDR takes to damp. This model explains the experi-

mental data very well at the temperature region  $1.5 < T \leq 3.0$  MeV and at low angular momentum region ( $J < 50\hbar$ ). However, it is unable to explain the T dependence below 1.5 MeV and at higher angular momentum in different mass regions [Sup12a, Dee12a, Sri08b]. Later, Kusnezov et al., [Kus98] proposed a very simple parametrized formula for the GDR width as a function of T and J of the system under the framework of the TSFM. The Kusnezov parametrization has been tested for large number of nuclei and found to be consistent with the prediction of TSFM calculation only above  $T = 1.5$  MeV.

In order to understand the discrepancy between experimental data and TSFM prediction at lower temperature, very recently, Deepak Pandit et al., [Dee12a] have proposed a new phenomenological model under the framework of pTSFM (kusnezov parametrization), named as Critical Temperature Fluctuation Model (CTFM). This new model emphasizes on an essential point, overlooked in the TSFM, that the GDR oscillations itself induce a quadrupole moment causing the nuclear shape to fluctuate even at  $T = 0$  MeV. Consequently, the GDR vibrations cannot view those thermal shape fluctuations that are smaller than its own intrinsic fluctuations. Therefore, the experimental GDR width should remain nearly constant at the ground state value up to a critical temperature ( $T_c$ ) and the effect of thermal fluctuations should become evident above  $T_c$  once they become larger than the intrinsic GDR fluctuations. It has been shown that the CTFM better explain the experimental data of Mukhopadhyay et al., [Sup12a] and Heckmann et al., [Hec03a]. To verify this critical behavior, Deepak Pandit et al., [Dee12a] have performed another experiment in two other mass regions ( $^{63}\text{Cu}$  and  $^{201}\text{Tl}$ ) and they have also observed that the CTFM better explain the experimental data than that of TSFM. They have concluded that the GDR width is not suppressed, rather the TSFM over predicts the experimental data at lower temperature. Therefore, the GDR in-

duced intrinsic fluctuation should be included in the TSFM calculation.

There was another theoretical calculation known as Collisional damping Model (CDM) [Bar96, Sme91], according to which the increase of GDR width is due to two body nucleon-nucleon or one body nucleon-nuclear surface collisions. This calculation showed that the one body collisional damping width has very weak dependence on  $T$  and remains almost similar to the ground state value. The two body collision comes into picture at higher temperature ( $T > 3$  MeV) and leads to an extra contribution in the GDR width showing a  $T^2$  dependence. However, this model is not suitable for the evolution of GDR width at low temperatures ( $T < 1.5$  MeV).

The macroscopic TSFM is very easy to use and predicts the experimental data in the range of temperature  $1.5 < T < 2.5$  MeV well. On the other hand, the PDM depends on the complex microscopic configuration. But, the phenomenological CTFM explain the data better than that of TSFM in all the mass regions. Therefore, CTFM should be used universally in describing the GDR width as a function of  $T$  and  $J$ . The detailed description of TSFM, PDM and CTFM has been discussed in the next Chapter 2 (Section 2.3).

## 1.7 Motivation of the present work

The basic aim of the present work is to understand the evolution of GDR width at very low temperatures. The experimental studies, over the years, have shown that the GDR width increases with both the temperature ( $T$ ) and angular momentum ( $J$ ) after a certain critical value. The angular momentum effect on GDR width is now well established and well explained by the theoretical models. A wealth of experimental data on the measurement of GDR width at  $T > 1.5$  MeV exists. The measured GDR widths for  $T > 1.5$  MeV were well described by the most popular thermal shape fluctuation model (TSFM). However, at

lower temperature ( $T < 1.5$  MeV) the picture is still unclear due to insufficient data. There are only a few experimental data in the mass region of  $^{120}\text{Sn}$ ,  $^{63}\text{Cu}$  and  $^{201}\text{Tl}$  at lower temperature ( $1.0 < T \leq 1.5$  MeV) where TSFM is not able to explain the data. Therefore, much more experimental data are required in other mass regions at this low temperatures to verify whether such a behavior is really true or not.

In order to understand the discrepancy between experimental observation and theoretical prediction at lower temperature, a new phenomenological model (CTFM) has been proposed. In CTFM, it was pointed out that the GDR width remains constant up to a critical temperature and thereafter increases with the increase in temperature. A very few experimental data exist for the confirmation of this critical behavior. Unfortunately, There are no experimental data below the critical point except for one measurement in  $^{63}\text{Cu}$  where only two data points exist below the critical value. As the situation stands now, the number of GDR width measurement till now at  $T < T_c$  are inadequate to test the critical behavior or to conclude that the GDR width remains constant at its ground state value below the critical point and deserves further investigation in the wide range of mass at below and above the critical point.

In order to address the above queries regarding the critical behavior of the GDR width as a function temperature, a systematic measurement of GDR width in the unexplored region ( $T = 0.8 - 1.5$  MeV) has been performed for  $^{97}\text{Tc}$  nucleus. The compound nucleus  $^{97}\text{Tc}$  has been taken mainly for two reasons. Firstly,  $^{97}\text{Tc}$  nucleus is very nearly spherical ( $\beta = 0.134$ ), secondly, in  $^{97}\text{Tc}$  nucleus, no such GDR measurement exists till now. In the present work, alpha induced fusion reactions have been employed to investigate the low temperature region. The alpha beam has been chosen because of the low Coulomb barrier in the entrance channel so that a wide range of low excitation energies can be

achieved in the compound nucleus.

The present thesis is organized in seven chapters. In the present chapter, the basic introduction of GDR and the motivation of this work are discussed. In the 2<sup>nd</sup> chapter, theoretical tools to interpret the GDR  $\gamma$ -ray spectra and different theoretical models (TSFM, CTFM, PDM) for the T and J dependence of GDR width are discussed. In the 3<sup>rd</sup> chapter, the detector systems and their GEANT4 simulations are discussed. In the 4<sup>th</sup> chapter, the details of experiments performed, data taking and analysis of the data are discussed. In the 5<sup>th</sup> chapter, the results obtained from the data and their interpretations from different theoretical calculations are discussed. Along with the GDR studies, the neutron response of the LAMBDA spectrometer also forms a part of this thesis work, which has been presented in 6<sup>th</sup> chapter. Finally, summary and conclusion with future outlook have been presented in 7<sup>th</sup> chapter.

## Chapter 2

# Theoretical tools to interpret the high energy $\gamma$ -ray spectra

In this chapter, the statistical model calculation for the interpretation of high energy  $\gamma$ -ray spectra and the different theoretical models to explain the temperature dependence of GDR width have been discussed.

### 2.1 Statistical Model Calculations

The theoretical description of nuclear reactions with microscopic models (shell model) with the full complexity of interaction of the individual nucleons involved is a very challenging problem. Therefore, other approaches have been developed. One of those is the statistical model of nuclear reactions. In the statistical model, it is assumed that a compound nucleus (CN) is formed with an excitation energy high enough so that many states may be excited by the interaction of projectile nucleons with the target nucleons. Moreover, all the degrees of freedom (Energy, Angular momentum, Mass) are equilibrated before the decay process takes place. The equilibrated compound nucleus decays without remembering the way it has been formed in the entrance channel except for the conserved quantities such as excitation energy ( $E^*$ ), angular momentum ( $J$ ), parity ( $\pi$ ), isospin ( $T$ ). The compound nucleus mainly decays via particle ( $n$ ,  $p$  and  $\alpha$ ) evaporation or  $\gamma$ -emission. The decay probabilities generally de-

pend on the statistical weight of the final states and barrier penetrabilities for various channels. The decay rate through any exit channel is determined by the reciprocity theorem i.e the transition matrix element associated with the CN formation are the same with those associated in the inverse decay process. The total decay rates, which is related to the life time of CN, is just the sum of all partial decay rates for each of the exit channels. The cross-section for the decay of CN into a particular channel is provided by the branching probability multiplied by the fusion cross-section for the formation of compound nucleus [Puh77, Sup12b]. A schematic diagram of CN decay is shown in Fig 2.1.

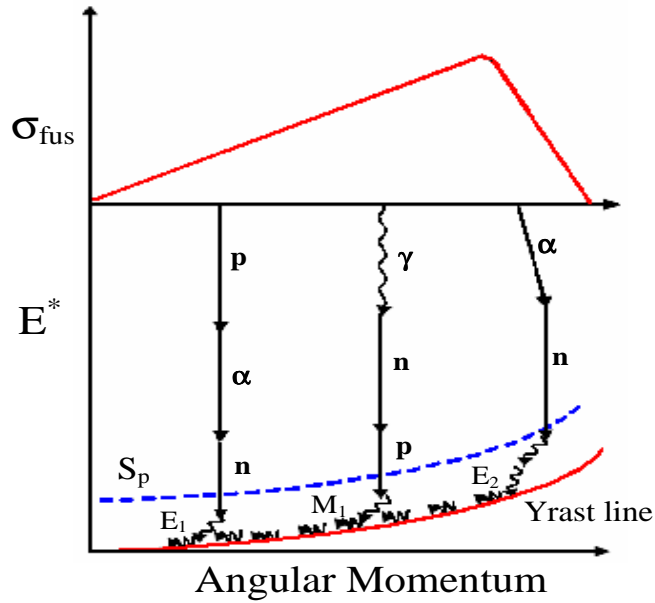


Figure 2.1: Schematic diagram of compound nuclear decay.

The reaction cross-section for the formation of compound nucleus from a projectile and target nucleus at a centre of mass energy ( $E_{cm}$ ) is calculated in terms of transmission co-efficient  $T_L(E_{cm})$  using the expression :

$$\sigma(J, \pi) = \frac{\lambda^2}{4\pi} \frac{(2J+1)}{(2J_p+1)(2J_T+1)} \sum_{S=|J_p-J_T|}^{S=J_p+J_T} \sum_{L=|J-S|}^{L=J+S} T_L(E_{CM}) \quad (2.1)$$

where  $J$ ,  $\pi$  are the spin and parity of the CN and  $J_P$ ,  $J_T$  are the spin of projectile and target nucleus, respectively.  $S = J_P + J_T$  is the total channel spin and  $\lambda$  is the wavelength. The summation over  $L$  is restricted by the parity selection rule  $\pi_P \pi_T (-1)^L$ . The transmission coefficients  $T_L$  have a very simple behavior as a function of  $L$  approximated by a Fermi distribution, given by

$$T_L = \frac{1}{1 + \exp[(L - L_0)/d]} \quad (2.2)$$

where  $d$  is the diffuseness parameter,  $L$  is the angular momentum. Here  $L_0$  is chosen in such a way that total CN cross-section  $\sigma_{CN} = \sum_{J,\pi} \sigma(J, \pi)$  is reproduced.

In this work, a modified version of statistical model code CASCADE [Puh77] has been used to explain the experimentally obtained data. Some basic parameters of the statistical model calculation of nuclear reactions have been discussed in the next section.

## 2.2 CASCADE : A statistical model code

CASCADE is a statistical model code for the decay of a compound nucleus populated in nuclear reaction. Originally, it was developed by Puhlhofer in 1977 [Puh77] and with time different scientific groups have modified, revised and improved the original code for their own need [Rat03a, Ram95, Sri08a, Hec03b, Sha99]. The code is based on Hausher-Feshback formalism of statistical decay of compound nucleus. This code actually calculates the CN decay probabilities where the excited CN is characterized by an initial excitation energy ( $E^*$ ) and angular momentum distribution ( $J$ ) in the form of ( $E^*, J$ ) matrix. For each matrix element, the neutron, proton,  $\alpha$ ,  $\gamma$  and fission probabilities are calculated and the corresponding populations go to new ( $E^*, J$ ) matrices. This process is continued until the excited nucleus reach below the particle threshold energy.

Below the particle threshold energy, the compound nucleus emits the statistical  $\gamma$ -rays in between particle threshold and yrast line (as shown in Fig 2.1) and go to another  $(E^*, J)$  matrices. And finally, it is finished off by the subsequent emission of low energy discrete yrast  $\gamma$ -rays. Based on the initial population, the code calculates the energy spectra for neutron, proton,  $\alpha$  and  $\gamma$ -rays. The calculated  $\gamma$ -ray spectrum folded with the detector response function has been compared with the experimentally obtained  $\gamma$ -ray spectrum to extract the GDR parameters. There are two main important ingredients in the statistical model calculation, the decay probabilities and the nuclear level density.

### 2.2.1 Decay probabilities

A compound nucleus populated at high excitation energy and angular momentum, decays via particle (mainly n,p, $\alpha$ ) or  $\gamma$ - emission. There is also a probability for the compound nucleus to undergo fission.

The particle emission probability is generally determined by the statistical weight of the initial and final states and transmission coefficients (barrier penetrabilities) using the reciprocity theorem. The decay rate  $R_p d\epsilon_p$  for emitting a particle p from an excited nucleus i (at excitation energy  $E_i$ , spin  $J_i$ , parity  $\pi_i$ ) to form a daughter nucleus f (at  $E_f$ ,  $J_f$ ,  $\pi_f$ ) is given by:

$$R_p d\epsilon_p = \frac{\rho_2(E_f, J_f, \pi_f)}{2\pi\hbar\rho_1(E_i, J_i, \pi_i)} \sum_{S=J_f-s_p}^{S=J_f+s_p} \sum_{L=J_i-S}^{L=J_i+S} T_L^p(\epsilon_p) d\epsilon_p \quad (2.3)$$

where  $\epsilon_p = E_i - E_f - B_p$  is the kinetic energy of particle p.  $B_p$ ,  $s_p$  and  $L$  are binding energy, spin and orbital angular momentum of the emitting particle, respectively.  $\rho_i$  and  $\rho_f$  are the level densities of the initial and final states of the nuclei.  $T_L^p$  is the transmission coefficient for a particle of energy  $\epsilon_p$ . The particle transmission coefficients are calculated by solving optical model equations of the nuclear system. In this thesis, the optical model parameters of Perey [Per63] and

Huizenga & Igo [Hui62] have been used for the protons and the alpha particles where as for neutrons, the parameters of Wilmore and Hodgson [Wil64] have been used.

The rate of  $\gamma$ -emission is also determined by similar type of formula given as:

$$R_\gamma d\epsilon_\gamma = \frac{\rho_f(E_f, J_f)}{2\pi\hbar\rho_i(E_i, J_i)} \sum_L f_L(E_\gamma) E_\gamma^{(2L+1)} dE_\gamma \quad (2.4)$$

where L denotes the multi polarity of the  $\gamma$ -decay. The emission of  $\gamma$ -rays due to the decay of GDR built on excited state is included in the modified CASCADE code. The absorption cross-section of GDR in case of spherical nuclei is well reproduced by a single Lorentzian distribution. The GDR strength functions is given by:

$$\begin{aligned} f(E_\gamma) &= \frac{4e^2}{3\pi\hbar Mc^3} S \frac{NZ}{A} \frac{\Gamma_{GDR} E_\gamma}{(E_\gamma^2 - E_{GDR}^2)^2 + \Gamma_{GDR}^2 E_\gamma^2} \\ &= 2.09 \times 10^{-5} \frac{NZ}{A} S f_{GDR}(E_\gamma) \end{aligned} \quad (2.5)$$

where S is the fraction of the energy weighted dipole sum rule (EWSR),  $E_{GDR}$  and  $\Gamma_{GDR}$  are the centroid energy and width of the GDR. For an axially symmetric deformed nucleus, the strength function is split and can be expressed as the superposition of two Lorentzian ( $f_1(E_\gamma)$  and  $f_2(E_\gamma)$ ) since the GDR resonance will vibrate along the principle axes with frequencies inversely proportional to the length of these axes. In that case,  $S_1$  and  $S_2$  are the sum rule strengths of the two components, and given as  $S_1 + S_2 = 1$  corresponding to 100% sum rule strength.  $S_1/S_2 = 2$  and  $1/2$ , respectively denote the GDR in a prolate and oblate deformed nuclei. The strength function can be expressed as

$$f_{GDR}(E_\gamma) = 2.09 \times 10^{-5} \frac{NZ}{A} \frac{S_1 f_1(E_\gamma) + S_2 f_2(E_\gamma)}{S_1 + S_2} \quad (2.6)$$

The above equation is derived only for  $L = 1$  multipolarity (E1 radiation). Others higher multiplicities ( $L > 1$ ) have not been considered. However, the contributions from higher multi polarities (such as quadrupole resonance) can be included but they have very small contributions to the high energy  $\gamma$ -ray spectra.

The fission probability (per unit time)  $W_{fiss}$  for the nucleus at an initial excitation energy  $E^*$  and angular momentum  $J$  in the Bohr and Wheeler theory [Boh39] of fission is proportional to the level density  $\rho_{fiss}(T)$

$$W_{fiss} = \frac{1}{2\pi\hbar\rho_{fiss}(E^*, J)} \int_0^{E^* - E_B} \rho_{fiss}(E^* - E_B - T) dT \quad (2.7)$$

where  $T$  is the kinetic energy of the nucleus at the saddle point and  $E_B$  is the angular momentum dependent fission barrier. For the decay of excited  $^{97}\text{Tc}$  considered here, there is no appreciable contribution to the decay cross section from the fission process due to the height of the fission barrier.

### 2.2.2 Nuclear level density

The basic nuclear level density formula, which is widely used in statistical model calculations, derived from the Fermi gas model, based on the pioneering work of Bethe [Bet36], is given by [Pra12],

$$\rho(E^*, J) = \frac{2J + 1}{12\mathcal{I}^{3/2}} \sqrt{a} \frac{\exp(2\sqrt{aU})}{U^2} \quad (2.8)$$

Where  $U = E^* - \Delta - J(J + 1)\hbar^2/2\mathcal{I}$  is the available energy,  $\mathcal{I} = \mathcal{I}_0 (1 + \delta_1 J^2 + \delta_2 J^4)$  is the effective moment of inertia of the compound nucleus in the form of deformed liquid drop with coefficients  $\delta_1$  and  $\delta_2$  and spherical rigid body moment of inertia  $\mathcal{I}_0$ . The excitation energy is back-shifted by the pairing energy  $\Delta = 12/\sqrt{A}$ ,  $A$  is the mass number of the nucleus. ‘ $a$ ’ is level density parameter taken as a free and user dependent parameter. In the Fermi Gas

Model, the level density depends on level density parameter ‘a’, that is in turn related to the finite size effect of the nuclear matter and the effective mass of the nucleon as well as the number of single particle levels near the Fermi surface. All of these depend on nuclear shell structure and deformation and also how the shell structure gradually melts with the increase in  $E^*$  of the nucleus. Puhlhofer’s statistical model code CASCADE includes formulation of level density parameter ‘a’ as per Dilg [Dil73] for  $E^* < 10$  MeV. For  $E^* > 20$  MeV,  $a = A/k$  was used based on the liquid drop model, where  $k$  is user dependent free inverse level density parameter and  $A$  is the nuclear mass. For  $E^*$  ranging from 10–20 MeV, a linear interpolation of ‘a’ and  $\Delta$  is done in midway between the parametrization of Dilg [Dil73] and that of liquid drop model. But the non-inclusion of the proper treatment of the shell corrections and its washing out at higher excitation energies along with the effect of nuclear deformation induces large uncertainty in explaining high energy  $\gamma$ - ray spectra if Dilg formulation is used. Ignatyuk et al., [Ign75] proposed an improved excitation energy dependent parametrization of the nuclear level density parameter which incorporated the effect of nuclear shell structure at low excitation energy and goes smoothly to the liquid drop value at higher excitation energy. This is expressed as

$$a(U) = \tilde{a} \left[ 1 + \frac{\delta W}{U} (1 - \exp(-\gamma U)) \right] \quad (2.9)$$

Here,  $\tilde{a}$  is the asymptotic Fermi-gas value of the level density parameter at high excitation energy where shell effects are believed to be damped, leading to a smooth dependence on  $A$ .  $\delta W$  is the shell correction obtained from the difference of the experimental and the liquid drop model (*LDM*) mass and  $\gamma^{-1} = 2A^{4/3}/5\tilde{a}$  is the rate at which the shell effects are damped with increasing excitation energy.  $\tilde{a}$  is asymptotic Fermi Gas level density parameter that is taken as free i.e user dependent parameter. In partial modification of this formula, Reisdorf

et al., [Rei81] showed that asymptotic level density parameter depends on the mass of the compound nucleus as well as the nuclear deformation, given by:

$$\tilde{a} = 0.04543r_0^3 + 0.1355r_0^2A^{-1/3}B_s + 0.1426r_0A^{-2/3}B_k \quad (2.10)$$

Where,  $B_s = 1$  and  $B_k = 1$  (for spherical nucleus) are the nuclear surface and curvature terms,  $r_0$  is the radius parameter.

In this thesis work, Ignatyuk formalism of level density has been used and instead of keeping  $\tilde{a}$  as a free parameter, the level density parameter is determined experimentally by measuring the evaporated neutron spectra in the same reaction.

### **2.3 Theoretical treatment of GDR width at finite T & J**

A number of theoretical approaches have been proposed to demonstrate the behavior of GDR width as a function of T and J. Among them, the macroscopic adiabatic thermal shape fluctuation model (TSFM) [Alh88] is the most popular and successful till date. Subsequently, Kusnezov et al., [Kus98] proposed a parametrized form of TSFM, from which one can easily calculate the temperature and spin dependence of GDR width for any nuclear mass. Recently, our group has proposed a new model by modifying the phenomenological parametrization (pTSFM) based on the TSFM and is called the Critical Temperature included Fluctuation Model (CTFM) [Dee12a]. The CTFM provides a good description of the behavior of GDR width for both T and J in the entire mass region compared to TSFM. Microscopically, the increase of GDR width as a function of T is described reasonably well within the Phonon Damping Model (PDM). In this section, all of the above models (TSFM, pTSFM, CTFM, PDM) have been discussed to explain the experimental data.

### 2.3.1 Thermal Shape Fluctuation Model (TSFM) : A macroscopic calculation

The thermal shape fluctuation model is the most popular model which describes the damping mechanism of the GDR vibration inside the nucleus. This model is based on the fact that the large amplitude fluctuation of nuclear shape plays an important role in describing the increase of GDR width as a function of temperature. Theoretically, the shape evolution of a nucleus as a function of temperature and angular momentum was calculated under the framework of Landau theory of shape transition by Y Alhassid et al., [Alh86] and S Levit et al., [Lev84]. They proposed that the shape fluctuation around the mean field values can not be neglected in finite nuclear systems. The effect of shape fluctuation on the GDR cross-sections were first investigated by M Gallardo et al., [Gal85, Gal87]. A few years later, Y Alhassid and B Bush [Alh88] proposed a macroscopic approach, based on the Landau theory, for GDR built on excited state and suggested that the quadrupole shape parameters play an important role in describing the GDR line shapes as a function of temperature. This macroscopic approach is known as Thermal Shape Fluctuation Model (TSFM). The details of this approach has been discussed as follows.

When in ground state, the nucleus remains in a definite shape i.e. either in a spherical or in a deformed configuration. The nuclear radius for a deformed nucleus in general can be expressed in terms of spherical harmonics about an equilibrium shape as,

$$R(\theta, \phi) = R_0 \left[ 1 + \sum_{\lambda, \mu} \alpha_{\lambda\mu} Y_{\lambda\mu}(\theta, \phi) \right] \quad (2.11)$$

where  $R_0$  is the equilibrium radius,  $\lambda$  is the multipolarity of the deformation and  $R(\theta, \phi)$  is the distance of the nuclear surface from the origin. The co-ordinates  $\alpha_{\lambda\mu}$  are the spherical tensor components (which transforms as spherical har-

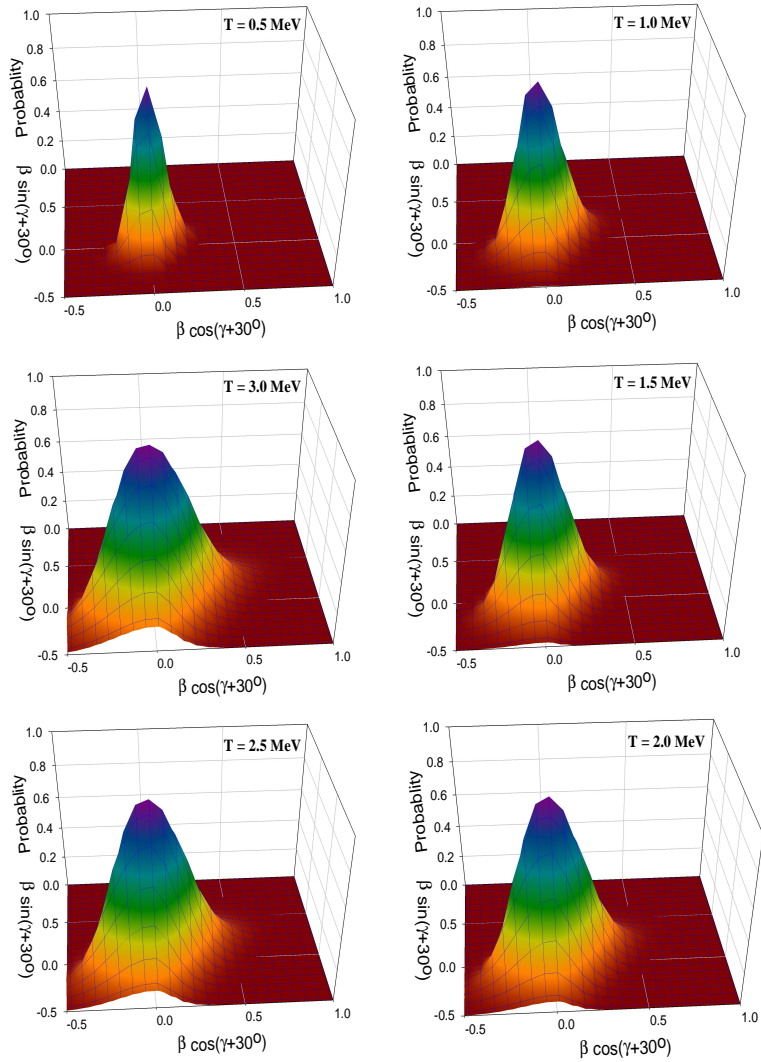


Figure 2.2: The deformation probability distributions of the free energy surface in the  $(\beta, \gamma)$  plane for  $^{97}\text{Tc}$  nucleus at different temperatures.

monics under rotation of the co-ordinate system) and gives the extent of the deformation. In case of nuclear shape transition, the quadrupole deformation parameter  $\alpha_{2\mu}$  are believed to play an important role. The parameters  $\alpha_{2\mu}$  describe the ellipsoidal shapes for the nuclear mean field. One can transform  $\alpha_{2\mu}$  from the laboratory frame into  $a_{2\mu}$  in the intrinsic principal frame, which is defined as  $a_{21} = a_{2-1} = 0$ ,  $a_{22} = a_{2-2}$  and  $a_{20}$  is real. The quantities  $a_{20}$  and  $a_{22}$  are then parametrized in terms of the deformation parameters  $\beta, \gamma$  [Hil53]

and are defined as

$$a_{20} = \beta \cos \gamma \quad (2.12)$$

$$a_{22} = \frac{1}{\sqrt{2}} \beta \sin \gamma \quad (2.13)$$

The parameters  $\beta$  gives the magnitude of deformation and  $\gamma$  denotes the types of deformation (e.g.  $\gamma = 0^\circ$  &  $60^\circ$  for axial prolate and oblate shapes, respectively).

These parameters ( $\beta, \gamma$ ) determine the intrinsic shape of the nucleus to be an ellipsoid with semi-axis length ( $k = 1, 2, 3$  for three principle axes)

$$R_k = R_0 \exp \left[ -\sqrt{\frac{5}{4\pi}} \beta \cos \left( \gamma - \frac{2\pi k}{3} \right) \right] \quad (2.14)$$

The corresponding GDR centroid energy is given by

$$E_k = E_0 \exp \left[ -\sqrt{\frac{5}{4\pi}} \beta \cos \left( \gamma - \frac{2\pi k}{3} \right) \right] \quad (2.15)$$

The widths for the different components of resonance energy are generally taken as [Aru04]

$$\frac{\Gamma_k}{\Gamma_0} = \left( \frac{E_k}{E_0} \right)^{1.9} \quad (2.16)$$

The equilibrium shape  $\beta_{eq}$  of a hot rotating nucleus can be obtained by minimizing the free energy  $F$  with respect to the quadrupole deformation parameters  $\beta$  and  $\gamma$ . In the liquid drop picture, the free energy for a hot rotating nucleus can be essentially related to the energy not locked up in the deformation degrees of freedom and can be written as [Alh93, Dee10b]

$$F(T, J, \beta, \gamma) = E_{LDM}(\beta, \gamma) - TS + \frac{J(J+1)\hbar^2}{2\hat{\omega} \cdot \mathcal{I} \cdot \hat{\omega}} \quad (2.17)$$

Where

$$\hat{\omega} \cdot \mathcal{I} \cdot \hat{\omega} = \mathcal{I}_{xx} \sin^2 \theta \cos^2 \phi + \mathcal{I}_{yy} \sin^2 \theta \sin^2 \phi + \mathcal{I}_{zz} \cos^2 \theta \quad (2.18)$$

is the moment of inertia about the rotation axis  $\omega$ .  $\mathcal{I}_{xx}$ ,  $\mathcal{I}_{yy}$  and  $\mathcal{I}_{zz}$  are the principal rigid body moments of inertia and  $S$  is the entropy of the system.  $E_{LDM}(\beta, \gamma)$  is the deformed liquid drop energy, calculated in terms of  $\beta$  and  $\gamma$  [Dee12b].

The nucleus at finite  $T$  and  $J$ , does not possess a single well-defined shape but rather starts to fluctuate around the equilibrium shape. Therefore, the nucleus loses its single well-defined shape, and explores a broad ensemble of mostly quadrupole shapes (defined by the deformation parameters  $\beta$  and  $\gamma$ ) and orientations with respect to a fixed frame (defined by Euler angles  $\theta, \phi, \psi$ ) due to thermal fluctuation. The observed GDR width in these conditions is the weighted average of all the frequencies associated with all possible shapes and orientations at a particular temperature and angular momentum and thus producing a large width. The probability of finding the excited nucleus in any certain shape (defined by the parameters  $\beta, \gamma, \theta, \phi, \psi$ ) at a certain temperature ( $T$ ) and angular momentum ( $J$ ) is given by the Boltzmann factor  $e^{-F/T}$ . In this approach, the equilibrium configuration of the nucleus can be obtained by minimizing the total free energy. Therefore, the GDR line shape is the weighted average of all possible shapes and orientations. The probability distributions of the free energy surface in the  $(\beta, \gamma)$  plane for the  $^{97}\text{Tc}$  nucleus at different temperatures are shown in Fig 2.2. The GDR strength function can be written as

$$\langle f_{GDR}(E_\gamma, T) \rangle = \frac{\int f_{GDR}(E_\gamma, T, \beta, \gamma) \exp[-F(T, \beta, \gamma)/T] d\tau}{\int \exp[-F(T, \beta, \gamma)/T] d\tau} \quad (2.19)$$

Here  $f_{GDR}$  denotes the GDR strength function. The term  $d\tau$  is the volume element associated with the parameter  $\beta, \gamma$ .

$$d\tau = \beta^4 d\beta \sin 3\gamma d\gamma \sin\theta d\theta d\phi d\psi \quad (2.20)$$

As the temperature increases, the fluctuation increases and so the ensemble average looks wider. As a result, the GDR width has been found to increase monotonically up to temperature  $T = 2.5$  MeV. At higher temperature ( $T > 2.5$  MeV), the nucleon-nucleon collision starts to dominate. This two body collision leads to an extra contribution in the GDR width showing  $T^2$  dependence. Finally, at much higher temperature, the particle decay from the compound nucleus becomes faster and gives rise to another contribution, known as particle evaporation width ( $\Gamma_{ev}$ ). However,  $\Gamma_{ev}$  is very small up to a temperature of  $\sim 2.5$  MeV, typically  $\ll 1$  MeV. The TSFM prediction of GDR width as a function of temperature has been shown by dashed line (without shell effect) and dotted line (with shell effect) in Fig 2.5,

The effect of angular momentum on the GDR width has been successfully explained by TSFM. At lower angular momentum, the angular momentum driven shape change and the associated width change is lower than that from thermal fluctuation itself. As the angular momentum becomes larger, the nucleus undergoes an oblate flattening due to centrifugal effects whose magnitude is determined by the interplay between the surface and rotational energies. The equilibrium deformation  $\beta_{eq}$  increases rapidly with  $J$ . As a consequence, the total GDR strength function undergoes further splitting, which increases the  $\Gamma_{GDR}$ . However, even though the equilibrium deformation increases with  $J$ , an increase in  $\Gamma_{GDR}$  does not occur until the  $\beta_{eq}$  increases sufficiently so as to affect the thermal average value of  $\langle\beta\rangle$ . In addition to the mean value  $\langle\beta\rangle$ , the nucleus also experience a spread in deformation, which can be measured by the variance  $\Delta\beta = \sqrt{\langle\beta^2\rangle - \langle\beta\rangle^2}$ . As long as  $\beta_{eq} < \Delta\beta$  (shown in Fig.2.3 in case of  $^{106}\text{Sn}$  nucleus), neither the mean deformation  $\langle\beta\rangle$  nor the GDR width  $\Gamma_{GDR}$  increases significantly.

Subsequently, Kusnezov et al., [Kus98] proposed a parametrized formula

for GDR width as a function of  $T$  and  $J$  based on TSFM, commonly known as Kusnezov parametrization. This parametrization explains the experimental data reasonably well and shows a universal behavior for the evolution of GDR width as a function of  $T$  and  $J$  for almost all nuclei. In this parametrization, the term  $J^2/2\mathcal{I}$  ( $\mathcal{I}$  is moment of inertia) is a dominant factor in describing the spin dependence of GDR width  $\Gamma_{T,J,A}$ . Since,  $\mathcal{I} \propto A^{5/3}$ , it must be expected that a scaling factor  $\xi = A^{5/6}$  would remove the mass dependence of GDR width. Therefore, the  $J$ -dependence of GDR width can be expressed in terms of that

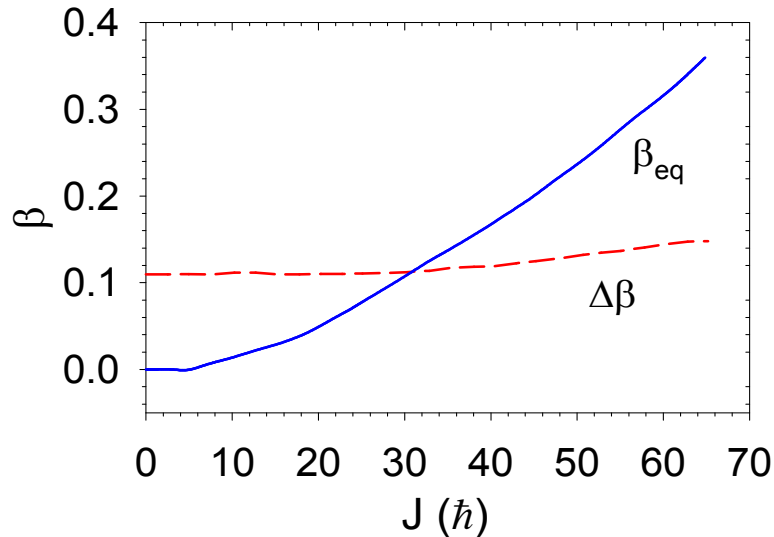


Figure 2.3: Evolution of the equilibrium deformation,  $\beta_{eq}$  for  $^{106}\text{Sn}$  at  $T = 1.8$  MeV as a function of angular momentum  $J$ . The dashed line shows the value of  $\Delta\beta$  [Bor98].

scaling factor  $\xi$ . The calculation shows a smooth dependence of this scaled width ( $\Gamma_{T,J,A}/\Gamma_{T,J=0,A}$ ) as a function of  $\xi$ , for the entire range of nuclear mass. This dependence, however changes with  $T$ . This can be solved if the scaled width is raised to a power depending on  $T$ . Thus, the smooth dependence of this final reduced width ( $\Gamma_{T,J,A}/\Gamma_{T,J=0,A}$ ) can be described with an analytical function of  $\xi$ . The Kusnezov parametrization, expressing the width as a function of  $T$ ,  $J$

and  $A$ , is given by :

$$\begin{aligned}
 \Gamma(T, J, A) &= \Gamma(T, J = 0, A)[L(\xi)]^{4/[T/T_0+3]} \\
 \Gamma(T, J = 0, A) &= \Gamma_0(A) + c(A)\ln(1 + T/T_0) \\
 c(A) &= 6.45 - A/100 \\
 L(\xi) &= 1 + \frac{1.8}{1 + e^{(1.3-\xi)/0.2}}
 \end{aligned} \tag{2.21}$$

Here,  $\Gamma_0(A)$  is the ground state GDR width and it has been taken as 3.8 MeV for almost all nuclei without any explanation,  $T_0$  is a reference temperature. The function  $c(A) \approx (6.45 - A/100)$  describes the weak  $A$ -dependence of the increase in width with  $T$ . It should be remembered that the Kusnezov parametrization provides an approximate description of the systematic behavior where the nuclear liquid drop picture is valid, i.e. in nuclei where shell effects are small or at temperatures where shell effects have already been melted.

### 2.3.2 Critical Temperature included Fluctuation Model (CTFM) : A new parametrization of TSFM

Deepak Pandit et al., [Dee12a] has proposed this new model. Mathematically, this is a modified form of the phenomenological parametrization of TSFM, but conceptually an essential point (which has been overlooked in TSFM) has been included in CTFM. It has been argued that the GDR vibration itself induces a quadrupole moment causing the nuclear shape to fluctuate even at  $T = 0$  MeV. Therefore, when the giant dipole vibration having its own intrinsic fluctuation is used as a probe to view the thermal shape fluctuations, it is unlikely to feel the thermal fluctuations that are smaller than its own intrinsic fluctuation. If this assumption is true, the experimental GDR widths should remain constant at the ground state values up to a critical temperature ( $T_c$ ) at which thermal shape fluctuation ( $\Delta\beta$ ) and intrinsic GDR fluctuation ( $\beta_{GDR}$ ) are same. The effect of

thermal shape fluctuation on GDR width will only be evident when the thermal shape fluctuations become larger than the GDR intrinsic fluctuation. So, there is a competition between  $\Delta\beta$  and  $\beta_{GDR}$  which leads to the critical behaviour and that's why the model has been named as Critical Temperature included Fluctuation Model. This novel idea has been applied to explain the experimental data for  $^{63}\text{Cu}$ ,  $^{119}\text{Sb}$  and  $^{201}\text{Tl}$ . It has been concluded that this model explains the data much better than the pTFSM or TFSM and the critical temperature shows a linear behavior with  $1/A$ . The deformation ( $\beta_{GDR}$ ) due to intrinsic

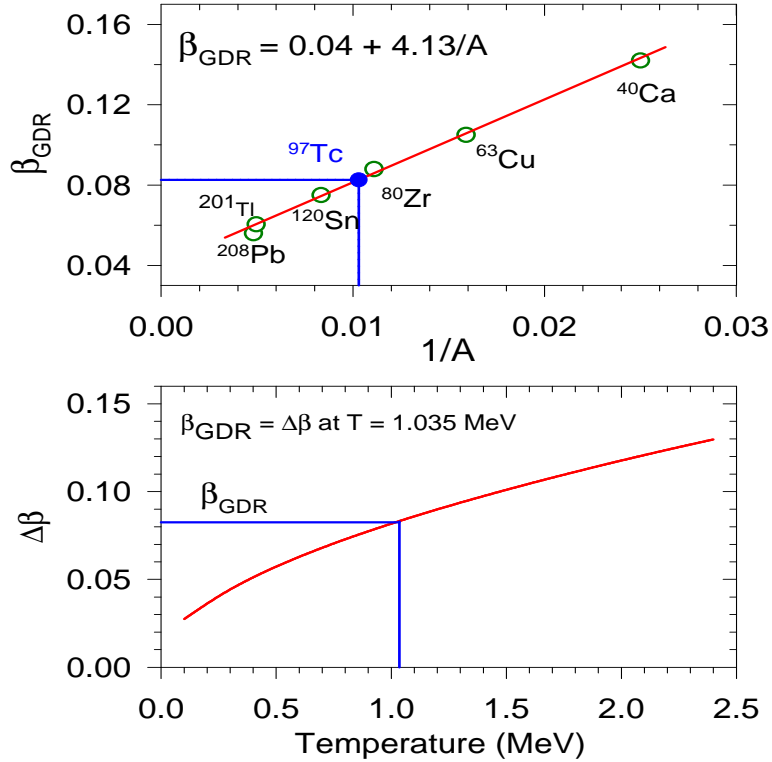


Figure 2.4: [Top Panel] The deformation due to GDR induced intrinsic fluctuation for different nuclei. [Bottom Panel] The temperature dependence of  $\Delta\beta$  for  $^{97}\text{Tc}$ , where  $\Delta\beta$  is the variance of the deformation due to thermal fluctuation of nuclear shape.

GDR fluctuation has been calculated by considering the formula  $\beta \propto Q_Q / \langle r^2 \rangle$  where  $Q_Q$  is the quadrupole moment induced by the intrinsic GDR fluctuation and  $r^L = 3R^L / (L+3)$ . The value of  $Q_Q$  has already been calculated under the

framework of time dependent Hartree-Fock theory in References [Sim09, Sto89] and the corresponding values have been reported for  $^{208}\text{Pb}$ ,  $^{120}\text{Sn}$ ,  $^{90}\text{Zr}$  and  $^{40}\text{Ca}$  as 99.0, 56.0, 46.5 and 21.4 fm<sup>2</sup>, respectively. The reported values are shown in the top panel of Fig 2.4, and shows a linear behavior with  $1/A$ . The variance of the deformation ( $\Delta\beta$ ) is generally calculated using the Boltzmann probability  $e^{-F(\beta,\gamma)/T}$  with the volume element  $\beta^4 \sin(3\gamma) d\beta d\gamma$ , according to the formalism described in Reference [Dee10b]. The temperature dependence of  $\Delta\beta$  is shown in the bottom panel of Fig 2.4. The critical temperatures are calculated by comparing  $\beta_{GDR}$  and  $\Delta\beta$ .

The temperature dependence of GDR widths in CTFM by including GDR induced fluctuations is given as [Dee12a]:

$$\begin{aligned} \Gamma(T, J = 0, A) &= \Gamma_0(A) & T \leq T_c \\ \Gamma(T, J = 0, A) &= c(A) \ln\left(\frac{T}{T_c}\right) + \Gamma_0(A) & T > T_c \end{aligned} \quad (2.22)$$

where,

$$T_c = 0.7 + 37.5/A$$

$$c(A) = 8.45 - A/50.$$

Here, instead of taking the  $\Gamma_0(A)$  as 3.8 MeV for all nuclei,  $\Gamma_0(A)$  has been taken as the actual ground state value which has been calculated using the ground state deformation and spreading width parametrization  $\Gamma_s = 0.05 E_{GDR}^{1.6}$  [Jun08]. The estimated ground state values are in good agreement with the actual measured values. The temperature dependence of GDR width as predicted by the CTFM is shown in Fig 2.5. The angular momentum dependence was parametrized through the reduced width at different temperature by a power law  $[\Gamma_{exp}(T, J, A)/\Gamma(T, J = 0, A)]^{(T+3T_0)/4T_0}$ . Using the available experimental

systematics in high J region for the masses  $A \sim 60$  to 200, the J-dependence of GDR width in CTFM has been proposed as:

$$\Gamma_{red} = \left[ \frac{\Gamma_{exp}(T, J, A)}{\Gamma(T, J=0, A)} \right]^{\frac{(T+3.3T_c)}{7T_c}} = L(\xi) \quad (2.23)$$

where,  $L(\xi) = 1 + 1.8/[1 + e^{(1.3-\xi)/0.2}]$  and  $\xi = J/A^{5/6}$ . The CTFM prediction of GDR width as a function of temperature has been shown in Fig 2.5.

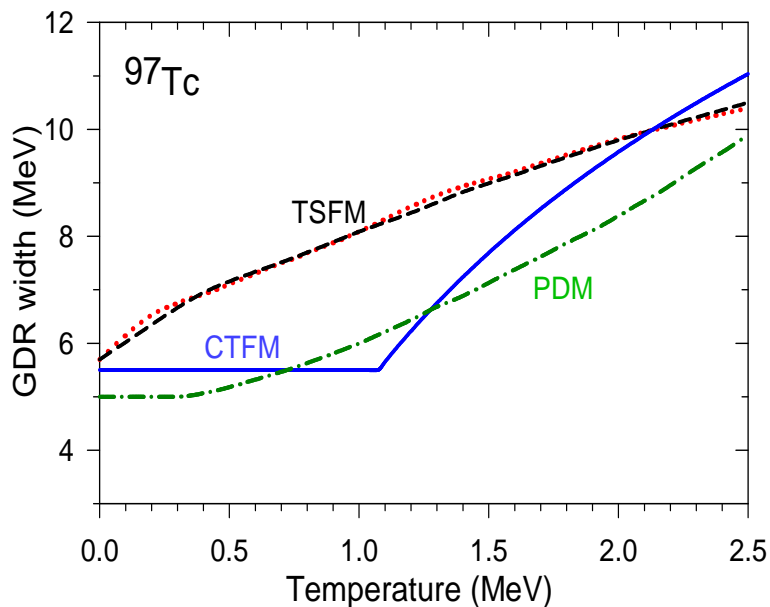


Figure 2.5: The GDR width as a function of temperature according to TSFM (Black dashed line), CTFM (Blue continuous line) and PDM (Green dot-dashed line) calculation. The red dotted line represent the TSFM calculation with shell effect.

### 2.3.3 Phonon Damping Model (PDM) : A microscopic calculation

From the microscopic point of view, the GDR built on ground states can be considered as a single or a group of several collective phonons of energy  $w_q$  close to the energy of the resonance ( $E_{GDR}$ ) [Wil56]. The collective phonon is a coherent superposition of particle-hole excitations. The width of the resonance mainly consists of Landau damping width ( $\Gamma_L$ ), escape width ( $\Gamma^\dagger$ ) and

spreading width ( $\Gamma_{\downarrow}$ ) [Har01]. The Landau width is due to the coupling of collective 1p-1h to non-collective 1p-1h excitations. The escape width is due to direct particle or  $\gamma$ -emission. The spreading width arises due to the coupling of collective 1p-1h to non-collective 2p-2h and more complicated np-nh configurations. The main contribution to the total GDR width comes from the spreading width. Ngyuen Dinh Dang and Akito Arima [Dan98] has done a sim-

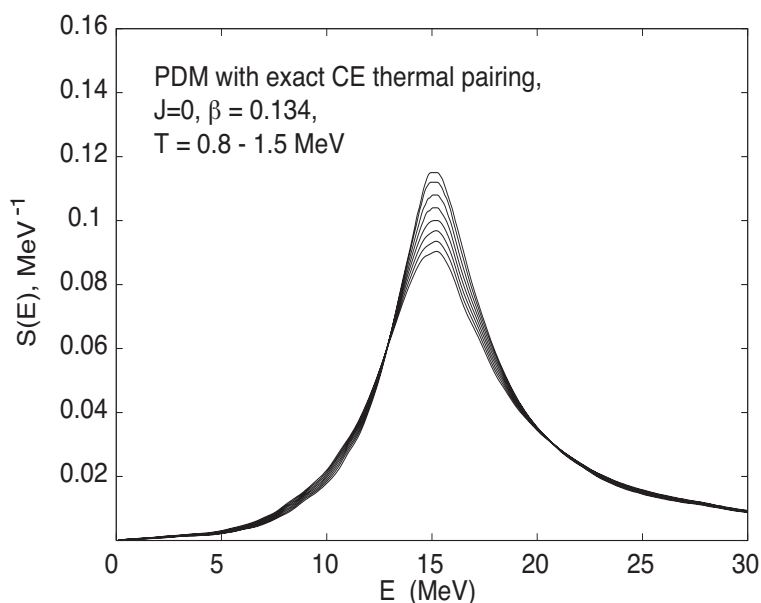


Figure 2.6: *The GDR line shapes at different temperatures calculated from Phonon Damping Model.*

ple extension of the above microscopic description of ground state GDR width to non-zero temperature ( $T \neq 0$  MeV) and this extension is known as Phonon Damping Model (PDM). Within the PDM, the GDR vibration is damped by the coupling of GDR phonon to non-collective particle-hole (ph), particle-particle (pp) and hole-hole (hh) configurations. The coupling to the various ph configurations leads to the quantal width which exists even at  $T = 0$  MeV, whereas the thermal width arises owing to the coupling to pp and hh configurations, which appear at  $T > 0$  because of the distortion of the Fermi surface. The

quantal width decreases, whereas the thermal width increases with increase in temperature. The details of the PDM calculation is discussed in Ref [Dan98]. The effect of super fluid thermal pairing is also included at low temperatures ( $T < 1$  MeV), since, in finite systems such as atomic nuclei, thermal pairing does not collapse at the critical temperature  $T_{cp} = 0.57\Delta$  ( $T = 0$  MeV) of the superfluidnormal phase transition in infinite systems, but decreases monotonically as  $T$  increases. The role of superfluid pairing effect on the GDR within the finite-temperature random phase approximation has been discussed in detail in Refs [Dan12a, Dan12b]. The PDM calculation of GDR line shape at the temperature region of  $T = 0.8-1.5$  MeV for  $^{97}\text{Tc}$  is shown in Fig 2.6. The evolution of GDR width as a function of  $T$  for  $^{97}\text{Tc}$  nuclei according to TSFM, CTFM and PDM has been shown in Fig 2.5.

## 2.4 Bremsstrahlung corrections

In the first chapter, it has already been discussed that the high energy  $\gamma$ -ray spectrum contain mainly three regions. The region of  $E\gamma \geq 25$  MeV has a large amount of non-statistical contribution due to nucleon-nucleon, nucleon-nucleus bremsstrahlung processes. The study of bremsstrahlung radiation is itself an interesting topic, but due to the poor statistics it was not possible to perform the detail analysis in this work. The presence of the bremsstrahlung component in the measured high energy  $\gamma$ -ray spectrum, poses a problem in matching the experimental data with the CASCADE prediction. The bremsstrahlung calculation is not included in the CASCADE calculation. However, it is important to include the bremsstrahlung contributions in the analysis to make it more precise.

The non statistical contributions to the experimental  $\gamma$  spectra arising due to bremsstrahlung emission is generally parametrized using the relation  $\sigma_{brem} =$

$k1/[k2 + \exp(E_\gamma/E_0)]$ , where  $k1$  &  $k2$  are constant and  $E_0$  is the slope parameter [Kel99]. The slope parameter  $E_0$  can be obtained by measuring the angular distribution of  $\gamma$ -rays. The  $\gamma$ -ray angular distribution is assumed to have the form  $\sigma(\theta) = A_0(E_\gamma)[1 + a_1(E_\gamma)P_1(\cos(\theta)) + a_2(E_\gamma)P_2(\cos(\theta))]$  as the emission of  $\gamma$ -rays is dominated by electric dipole radiation [Kel99]. The separation of the statistical GDR contribution and of the non-statistical bremsstrahlung background is possible due to the fact that the two components differ in the  $a_1(E_\gamma)$  coefficient. The  $a_1(E_\gamma)$  coefficient should be zero for statistical emission, however, it is non zero for higher gamma energies due to bremsstrahlung emission. In our earlier work [Sup12a], the values of  $a_1(E_\gamma)$  coefficients were obtained from the high energy  $\gamma$ -ray spectra measured at  $55^\circ$ ,  $90^\circ$  and  $125^\circ$ . The slope parameter ( $E_0$ ) of the bremsstrahlung shape was extracted by simultaneously fitting both the high energy  $\gamma$ -ray spectra measured at  $90^\circ$  and the extracted  $a_1(E_\gamma)$  coefficient using the method described in Refs [Trz01, Hab97]. It was shown that the extracted values of the slope parameters were consistent with the systematics  $E_0 = 1.1[(E_{Lab} - V_c)/A_p]^{0.72}$  [Nif90], where  $E_{Lab}$ ,  $V_c$  and  $A_p$  are the beam energy, Coulomb barrier and the projectile mass, respectively.

In the present work, the slope parameter was taken from the systematics. Next, the bremsstrahlung contribution was normalized to the experimentally measured spectra at  $E_\gamma \geq 25$  MeV and finally added with the calculated  $\gamma$ -ray spectra after folding with the detector response function.



# Chapter 3

## Detectors and simulation studies

The high energy  $\gamma$ -ray from the decay of giant dipole resonance (GDR) is an important tool to study the nuclear properties. A detector system is an integral part of the high energy  $\gamma$ -ray measurement and hence, the key to unfold nuclear properties. On the other hand, the detector simulation is another important part which provides the detector response function needed to fold the theoretical spectrum before comparing with the experimental data. Along with that, the simulation also helps in extracting the efficiency of the neutron detector and the conversion of experimental fold distribution to angular momentum distribution. In this chapter, the detail of the detector systems ( $\text{BaF}_2$  scintillator and liquid organic scintillator) used in this thesis work as well as their simulation studies (for the detector response function) are discussed.

### 3.1 $\gamma$ -ray detectors

The high energy  $\gamma$ -rays ( $> 8$  MeV) mainly interact via pair production and produce an electromagnetic shower in the entire volume of the detector. In order to confine this shower, a large interaction volume with high  $\gamma$ -detection efficiency is required. Apart from that, during in-beam experiments, neutrons are the major source of background in the high energy  $\gamma$ -ray spectra. Thus, it is important to have a detector with a very good n- $\gamma$  discrimination capability. Mostly, this discrimination is done by time-of-flight technique, where a detector

with a very good time resolution is essential. The detectors having better time resolution can also be placed very close to the target, and thereby subtending a large solid angle which is important for low cross-section measurements. Good gain stability is also a major requirement for a good detector. Thus, to measure the high energy  $\gamma$ -rays, one should choose those detectors which have large interaction volume, high  $\gamma$ -detection efficiency, very good time resolution and high gain stability.

At present, there are different types of  $\gamma$ -ray detectors such as High Purity Germanium (HpGe) detector, inorganic scintillators [NaI(Tl), BaF<sub>2</sub>, LaBr<sub>3</sub>] etc. The HpGe detector has very good energy resolution (0.3% at 662 keV). However, the high resolution Ge crystals have very small  $\gamma$ -detection efficiency due to small size and low effective atomic number, and very poor timing response. Therefore, the HpGe detectors are not suitable for measuring the high energy  $\gamma$ -rays. Moreover, the GDR itself has small decay probability in the decay of compound nuclei and thus, the efficiency factor rather than the energy resolution has been the main concern to measure the GDR  $\gamma$ -rays.

Inorganic scintillators [NaI(Tl), BaF<sub>2</sub>, LaBr<sub>3</sub>] are commonly used in the detection of the high energy photons because of their high atomic number and high density. BaF<sub>2</sub> has been one of the most popular scintillator used in high energy  $\gamma$ -ray spectroscopy due to its transparency and ability of being one of the fastest scintillators to detect the high energy  $\gamma$ -rays and other high energy particles. It has large  $\gamma$ -detection efficiency due to its high effective atomic number. Besides, it is highly dense (4.89 gm/cm<sup>3</sup>) that makes the detector highly efficient for  $\gamma$ -detection. The other two important properties, that help BaF<sub>2</sub> to become one of the most suitable high energy  $\gamma$ -ray detector, are the smaller radiation length (2.05 cm) and the Moliere radius (3.39 cm) for effective confinement of the longitudinal and transverse spread of the electromagnetic

shower generated due to  $\gamma$ -ray interaction with the detector material. The scintillation light output of BaF<sub>2</sub> crystal mainly consists of two components: a fast component (decay time  $\tau_1 = 0.6$  ns) peaking at shorter wavelength  $\lambda_1 = 220$  nm and a slow component (decay time  $\tau_2 = 630$  ns) peaking at longer wavelength  $\lambda_2 = 320$  nm with intensities 20% and 80%, respectively. The fast and slow components give the time and energy informations of the absorbed photons, respectively. In addition to that, the ratio of their relative intensities depends on the ionizing power of the absorbed particle which allows identification of the incident radiations by pulse shape discrimination technique. The total number of scintillation photons emitted from a BaF<sub>2</sub> crystal is about 9000 per MeV of absorbed photon energy ( $\sim 2000$  for fast and 6500 for slow component). As the slow component of the BaF<sub>2</sub> light output is dependent on temperature, the gain variation of BaF<sub>2</sub> is a significant factor, which can be controlled by continuous monitoring and controlling the room temperature of the experimental hall. The scintillation properties of BaF<sub>2</sub> are displayed in Table 3.1.

NaI(Tl) scintillators are also used to detect the high energy  $\gamma$ -rays. The total number of scintillation photons emitted from NaI(Tl) is around 40000, greater than that of BaF<sub>2</sub> crystal. Though the energy resolution of NaI(Tl) is better than the BaF<sub>2</sub> scintillators, they are comparable in  $\gamma$ -detection efficiency. But, the BaF<sub>2</sub> scintillators have good timing response than the NaI(Tl) due to the presence of very fast scintillation decay component (600 ps). Therefore, BaF<sub>2</sub> scintillator is superior to the NaI(Tl) in all applications where a fast timing is required. Other advantages of using BaF<sub>2</sub> scintillator are that it is non-hygroscopic, has lower thermal neutron capture probability and lower radiation damage. The merits and de-merits of BaF<sub>2</sub> scintillator compared to NaI(Tl) scintillator are displayed in Table 3.2.

On the other hand, LaBr<sub>3</sub> is a relatively new inorganic crystal that has been

gaining popularity for the study of  $\gamma$ -ray spectroscopy due to its excellent timing resolution ( $\sim 200$  ps, depending on the detector size) and energy resolution ( $\sim 2.8\%$  at 662 keV for 1 inch scintillator). It has large  $\gamma$ -detection efficiency due to the high atomic number and high density ( $5.1 \text{ gm/cm}^3$ ). The total number of scintillation photons produced for 1 MeV incident photon is  $\sim 60000$ , which is greater than that of NaI(Tl) and BaF<sub>2</sub> scintillator. The disadvantage of LaBr<sub>3</sub> scintillator is its high light output which affects the linearity and gain stability of the detector. Moreover, the LaBr<sub>3</sub> crystal is very hygroscopic in nature.

Table 3.1: *BaF<sub>2</sub> scintillator properties*

Scintillation outputs	A fast component $\lambda_1=220$ nm and a slow component at $\lambda_2=320$ nm
decay time constants	$\tau_1 = 0.6$ ns & $\tau_2 = 630$ ns
Relative intensities	20% for $\lambda_1$ & 80% for $\lambda_2$
Number of photons emitted per MeV of absorbed radiation	Approximately 2000 for $\lambda_1$ and 6500 for $\lambda_2$ (factor of 4-5 smaller than NaI(Tl))
Transmission range	150 nm to $11.5\mu\text{m}$
Refractive index	1.5 at 300 nm
Density	$4.89 \text{ gm/cm}^2$
Radiation Length	2.05 cm
Molliere radius	3.39 cm

At the Variable Energy Cyclotron Centre, Kolkata, India, two major detector systems, a Large Area Modular BaF<sub>2</sub> Detector Array (LAMBDA) spectrometer [Sup07] and a  $\gamma$ -multiplicity filter [Dee10a] have been developed using BaF<sub>2</sub> scintillators. The former detects the high energy  $\gamma$ -rays from the decay of GDR built on highly excited states while the latter detects the low energy discrete  $\gamma$ -rays for measuring the angular momentum populated in the compound nucleus.

Table 3.2: Merits and de-merits of BaF<sub>2</sub> scintillators (adopted from [Sup12b])

Merits	<ul style="list-style-type: none"> <li>• Sub-nano second order timing.</li> <li>• Non-hygroscopic.</li> <li>• Atomic weight of Barium = 56, high efficiency for gamma detection.</li> <li>• Low thermal neutron capture probability.</li> <li>• Good chemical and mechanical stability.</li> <li>• Low radiation damage.</li> </ul>
De-merits	<ul style="list-style-type: none"> <li>• Light outputs are in ultra violet region (requires expensive quartz window PMT).</li> <li>• Poorer energy resolution (factor of 2 worse than NaI(Tl)).</li> <li>• Intensity of slow component (<math>\lambda_2</math>) is temperature dependent.</li> <li>• Presence of intrinsic alpha activity due to radium impurities, which are always present in the BaF<sub>2</sub> crystals.</li> </ul>

### 3.1.1 The LAMBDA spectrometer

The LAMBDA spectrometer [Sup07] consists of 162 large BaF<sub>2</sub> crystals each of them having a length of 35 cm and cross-sectional area of 3.5×3.5cm<sup>2</sup>. The detectors have been developed indigenously from bare crystals. First, each crystal was cleaned thoroughly using dehydrated ethyl alcohol. Each crystal was then wrapped with 8 - 10 layers of 10 μm thick white Teflon cloth since it is a very good UV reflector. Another advantage of using Teflon is that it acts as a diffused reflector, producing detector outputs nearly independent of scintillation center position inside the crystal volume, minimizing the non-uniformity in case

of detectors having larger lengths. The crystal with Teflon layer was further wrapped by aluminium foil of thickness  $10\ \mu\text{m}$  (3 - 4 layers) to enhance the light collection and to block the surrounding lights from outside entering into the detector. As the scintillation light output is produced in the UV region, the optical coupling between crystal and Photo Multiplier Tube (PMT) must have a good transparency for UV light. Hence, a fast UV sensitive photo multiplier tubes (PMT) (29 mm dia, Philips XP 2978) with a fused silica window was coupled with the crystal using a highly viscous UV transmitting optical grease (Basyllone,  $\eta$  - 300000 stokes). The optical coupling was done very carefully to avoid any formation of air bubble in the grease over the crystal surface, because the air bubble present unwanted reflecting surface amounting to a loss of scintillation light. After coupling, the complete system was covered with black tape for light tightness. Finally, the total assembly (crystal + PMT) was covered with a heat shrinkable PVC tube for mechanical stability. The LAMBDA spectrometer arranged in the form of three  $7 \times 7$  matrix form has been displayed in Fig 3.1. One  $7 \times 7$  array of the spectrometer placed at a distance of 50 cm from the target at an angle of  $90^\circ$  with the beam axes covered a solid angle 1.8% of  $4\pi$ . It needs to be mentioned that the spectrometer is highly granular which greatly reduces the possibility of  $\gamma$ - $\gamma$  and  $\gamma$ -n pile up events. It has large  $\gamma$ -ray detection efficiency with a very good time resolution (960 ps for each  $\text{BaF}_2$  detector in the LAMBDA array). The modularity of this spectrometer is such that it can be arranged in two  $9 \times 9$ , three  $7 \times 7$  or six  $5 \times 5$  matrix configurations and placed at different angles with respect to the beam axis which is important for GDR angular distribution studies. The pulse shape and the uniformity of the detectors were studied using a  $^{137}\text{Cs}$   $\gamma$ -ray source and an oscilloscope (Tektronix model TDS724D, 500 MHz). The fast to slow component ratio, defined as the maximum pulse amplitude divided



Figure 3.1: *The LAMBDA spectrometer arranged in three  $7 \times 7$  matrix configurations.*

by the amplitude of the signal measured at 20 ns from the peak position, was found to lie between 10 and 12 for all the crystals. The uniformity of the detectors were checked by moving a  $^{137}\text{Cs}$  source along the length of the crystals and the corresponding peak positions were monitored. The non-uniformity was less than 5%. The  $\alpha$ -activities present inside the crystals due to the Radium impurities were checked using pulse shape discrimination technique and the measured values were less than 0.3 counts/sec/cm<sup>3</sup> which lie below 4 MeV and does not affect the high energy  $\gamma$ -ray measurement. The details of high energy  $\gamma$ -ray measurements have been discussed in Chapter-4.

### 3.1.2 Multiplicity filter

In the fusion evaporation reaction, the compound nucleus is populated at a well-defined excitation energy but with a broad angular momentum distribution. The populated compound nucleus loses most of the excitation energy through particle and GDR  $\gamma$ -ray emissions above the particle threshold. The remainder of the excitation energy and most of the angular momentum are removed by

the statistical E1  $\gamma$ -ray and low energy yrast stretched E2  $\gamma$ -ray emissions, respectively. The angular momentum loss due to particle emission and GDR  $\gamma$ -rays emission is negligibly small. Therefore, the angular momentum information is generally extracted by measuring the low energy yrast  $\gamma$ -rays. Since, the main purpose of this thesis is to study the GDR property which depends on both the excitation energy and angular momentum populated, it is very important to separate two effects in order to understand their individual contributions. One of the ways to decouple this two effects is by making measurements of the high energy  $\gamma$ -rays in coincidence with the multiplicity of the low energy yrast  $\gamma$ -rays. Therefore, a 50 element  $\gamma$ -multiplicity filter has been developed at the Variable Energy Cyclotron Centre, Kolkata, India to detect that low energy yrast  $\gamma$ -rays for the study of angular momentum gated GDR phenomena [Dee10a].

The  $\gamma$ -multiplicity filter [Dee10a] consists of 50 BaF<sub>2</sub> crystals each having length of 5 cm and cross-sectional area of  $3.5 \times 3.5$  cm<sup>2</sup> as shown in Fig 3.2. This detector system acts as an ancillary system to the LAMBDA array and also serves as a time start trigger for the time of flight measurement. The energy resolution of each detector element is  $\sim 7.2\%$  at 1.17 MeV and time resolution is  $\sim 450$  ps [Dee10a]. The filter is split into two blocks of 25 detectors each, in a staggered castle type geometry. The staggered geometry equalizes the solid angle subtended by each multiplicity detector element at the centre of the target. The geometric efficiency of the filter is  $\sim 56\%$  if placed at 5 cm from the target position in staggered castle type geometry.

The  $\gamma$ -multiplicity filter records the total number of detectors fired (designated as fold, F) in each event in coincidence with the high energy  $\gamma$ -rays. The fold distributions have been converted into the angular momentum distribution using a realistic technique [Dee10a] based on the Monte Carlo GEANT4 simulation which has been discussed in section 3.3.2.



Figure 3.2: The  $\gamma$ -multiplicity filter, split into two blocks of each 25 detectors arranged in  $5 \times 5$  matrix configurations.

### 3.2 Neutron detector: Liquid organic scintillator (BC501A)

The nuclear level density parameter (NLD) is an important ingredient in the statistical model calculation as well as in extracting the temperature of the compound nucleus. In general, the temperature and NLD parameter can be estimated by measuring the evaporated neutron energy spectrum. The liquid organic scintillator is widely used for neutron measurement in a mixed field of neutrons and  $\gamma$ -rays due to its good timing property, high light output and high neutron detection efficiency. A liquid organic scintillator (BC501A) based neutron time-of-flight (TOF) detector array [Ban07] has been developed at the Variable Energy Cyclotron Centre, Kolkata, India for the spectroscopic study of energetic neutrons emitted in the accelerator induced nuclear reactions. A part of the neutron TOF detector array is shown in Fig 3.3. A single neutron detector (5 inch in diameter and 5 inch in length) has been used in this work to detect the evaporated neutrons for estimating the nuclear level density parameter and

hence the compound nuclear temperature.

The detector cells are cylindrical in shape and made up of 3 mm thick stainless steel. The internal walls of the cells are white painted for efficient light collection and filled with xylene based liquid scintillator (BC501A) after passing dry nitrogen gas to remove any Oxygen present in the liquid. Scintillator cells sealed with 6 mm thick Pyrex glass are coupled with 12.7 cm PMT (Model : 9832B, Electron tube Ltd). The detectors have very good intrinsic time resolution and pulse shape discrimination. The intrinsic time resolution of the detectors are  $\sim 1.2$  ns, which can easily discriminate the low energy neutrons from  $\gamma$ -rays by TOF technique. High energy neutrons are generally separated by n- $\gamma$  pulse shape discrimination. Finally, the neutron can be well distinguished by using both the techniques, TOF and pulse shape discrimination. The efficiency of the detectors are also reasonable ( $\sim 50\%$  at 5 MeV for 5 inch  $\times$  5 inch detector placed at 150 cm from the target position). The detail information about the design, fabrication and development of the detectors are discussed in References [Ban07, Ban09].



Figure 3.3: *Liquid organic scintillator (BC501A) based neutron time-of-flight detector array.*

### 3.3 GEANT4 simulation of the detector systems

GEANT4 [Ago03] is a toolkit developed by engineers and scientists at CERN and other institutions worldwide, to simulate the response of various types of particles and radiation (having huge energy range from the eV to TeV) through different medium. The toolkit is based on different software and object oriented programme in C++. The toolkit has a hierarchical structure of domains or classes that are linked together when the program is compiled with a GNU makefile. Several domains or classes that are necessary to construct a physics case are given by:

- The geometry and material of the detector used – G4DetectorConstruction class.
- Particle interaction within the detector medium or other material – G4PhysicsList class.
- Particle generation, throwing the particles, particles direction and momentum, the hit pattern etc – G4PrimaryGeneratorAction class.
- Tracking of the particle i.e how many steps the particle are moving – G4SteppingAction or G4TrackingAction class
- Event and track management i.e event by event information – G4EventAction class
- Visualization and user interface framework.
- Histogram plotting – DataRecordTree class.

Individual particles are randomly generated by a particle generator and tracked through the detector volume. The energy depositions are recorded step-by-

step and finally added for each event. The event-by-event information are then plotted by histogramming in ROOT software. It should be remembered that in PhysicsList class, all the required physics processes (ionization, scattering, multiple scattering etc for charged particle, all the electromagnetic processes for  $\gamma$ -rays and elastic, inelastic, fusion model, capture model etc for neutron) have to be included. The details of the GEANT4 toolkit is discussed in Reference [Ago03]. In this thesis work, GEANT4 simulation has been performed to study the response function of the detectors used in the present work.

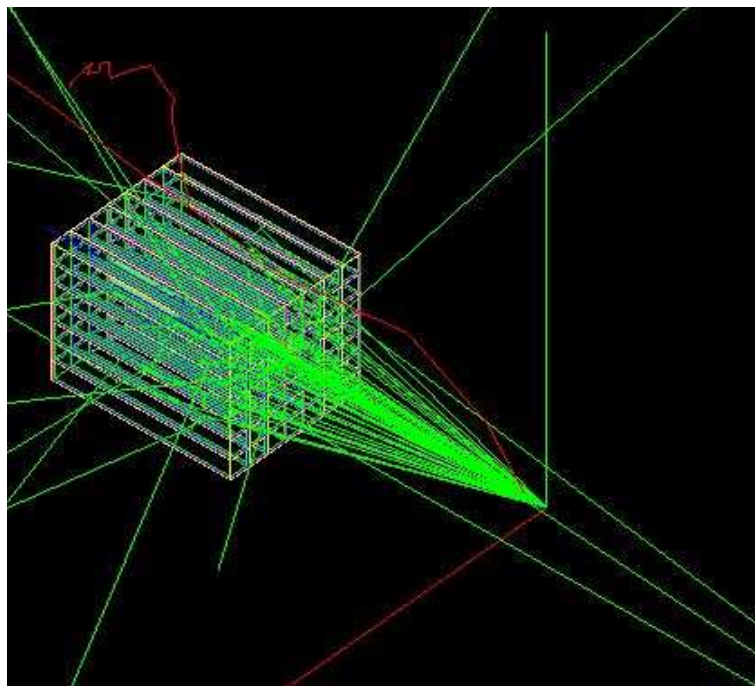


Figure 3.4: *Detector geometry of the LAMBDA spectrometer arranged in  $7 \times 7$  matrix configuration using GEANT4 simulation code. The  $\gamma$ -rays are thrown isotropically to the front face of the spectrometer.*

### 3.3.1 Simulation of the LAMBDA array and its response function

Simulation of the LAMBDA array is very important to extract the information (GDR parameters) properly from the measured high energy  $\gamma$ -ray spectra.

The GDR parameters are generally extracted by comparing the experimental data with the statistical model calculations. When comparing the experimental data and theoretical calculation, it is necessary to either unfold the experimental data or fold the theoretical calculation. Unfolding the data is suitable for a single high energy  $\gamma$ -ray with high statistics [Suk95]. In the present work, the  $\gamma$ -ray yield considers a range variation of  $10^6 - 1$  from the energy range 4–30 MeV. Hence, it is very difficult to unfold the continuous  $\gamma$ -ray yield from the GDR decay because of poor statistics at higher energy ( $>20$  MeV). Therefore, the theoretical calculations were directly folded with the detector response function for a realistic comparison with the experimental data. The detector response function of the LAMBDA array was obtained using the Monte Carlo code GEANT4 [Ago03]. The code allows us to specify the exact geometry of the

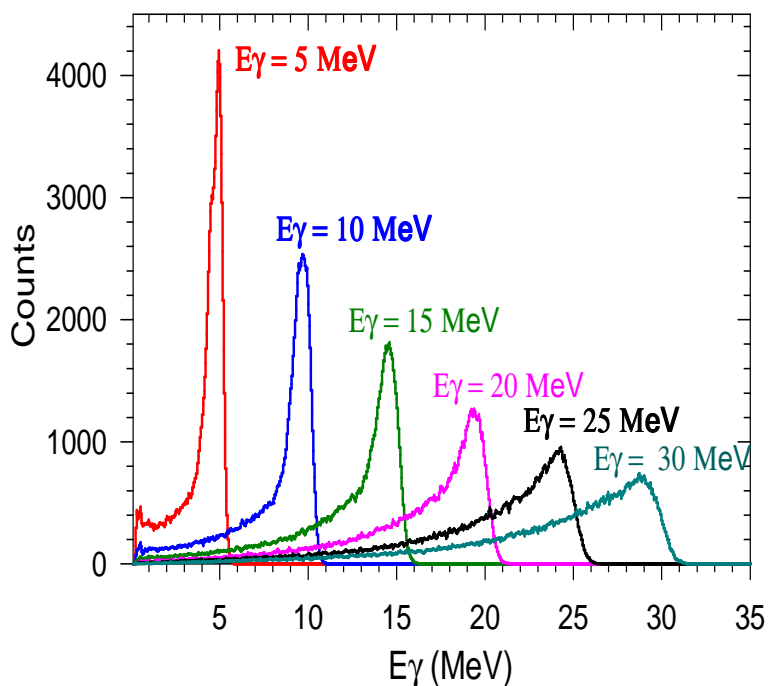


Figure 3.5: The GEANT4 simulated line shapes at  $E_\gamma = 5, 10, 15, 20, 25$  and  $30$  MeV for the LAMBDA array arranged in  $7 \times 7$  matrix configuration.

experimental set-up. The  $\text{BaF}_2$  wrapping material (Teflon, Aluminium, PVC),

target chamber, air gap were all included in the simulation to make the calculation more realistic. The response of the PMT is not included in the simulation code. In the geometrical set-up, the array was arranged in  $7 \times 7$  matrix configuration and placed at 50 cm from the centre of the target chamber as per the experimental set-up. A lead sheet of 3 mm (which was used to cut down the x-rays during experiment) has been placed in front of the LAMBDA array to keep the same experimental configuration. The geometrical set-up using GEANT4 simulation is shown in Fig 3.4. The energy resolution of each detector and electronic threshold were also considered properly. The  $\gamma$ -rays were randomly generated by a particle generator (G4ParticleGun) and thrown isotropically on the front face of the array and then tracked through the array. As the high energy  $\gamma$ -ray incident on a single  $\text{BaF}_2$  in the LAMBDA array, has the probability to escape to the neighbouring detector, the event must be reconstructed to get the full energy information of that particular event. For event reconstruction, different methods have been tested and event-by-event nearest neighbour summing or cluster summing technique has been found to be most suitable in this configuration. The details of the cluster summing technique has been discussed later in the next Chapter (Section-4.5). The incident  $\gamma$  rays have the energies ranging from 0.1 to 40 MeV with 0.1 MeV steps. The hit pattern of the incident particles were also recorded. One million events were triggered for each energy steps and the corresponding line shapes (with energy bin 0.1 MeV) were recorded. The corresponding line shapes for  $E_\gamma = 5, 10, 15, 20, 25$  and 30 MeV have been shown in Fig 3.5. Thus, the line shape of LAMBDA array has been calculated for the  $\gamma$ -rays from 0.1 to 40 MeV. So there are a total of 400 line shapes and each line shape forms subsequent rows of the response matrix. Finally, we get detector response function in a  $400 \times 400$  matrix form. The calculated  $\gamma$ -spectra are required to be multiplied each time by this response

matrix to compare with the experimental  $\gamma$ -ray spectra.

### 3.3.2 Simulation of Multiplicity filter and conversion of experimental fold distribution to angular momentum distribution

The angular momentum distribution of populated compound nucleus is required for the proper estimation of nuclear temperature and also used as an input in the statistical model calculations. The knowledge of populated angular momentum in the compound nucleus is also important to perform the theoretical Thermal Shape Fluctuation Model, Critical Temperature Fluctuation Model, Phonon Damping Model calculations properly. Different approaches can be applied to extract the angular momentum distribution from the experimental fold distribution. In this work, an approach (which has been used in our earlier work [Dee10a]) based on GEANT4 simulation has been taken. In the experiment, the multiplicity folds (the number of detectors fired) were obtained by measuring the low energy discrete  $\gamma$ -rays in an event by event mode using the  $\gamma$ -multiplicity filter. The final experimental fold spectrum was generated during off-line analysis by gating with the high energy  $\gamma$ -rays to remove the non-fusion events which generally appear for the lowest folds and then compared with the simulated fold distribution. In the simulation, the exact experimental conditions (detector geometry, detector threshold, trigger condition, etc) were taken into account. In the geometrical set-up, two blocks of 25 detectors arranged in  $5 \times 5$  matrix (in staggered castle type geometry) were kept on the top and bottom of the target chamber, similar to the experiment, at distance of 5 cm from the target position. The geometrical set-up using GEANT4 simulation is shown in Fig 3.6. The low energy  $\gamma$ -rays were generated using a random number generator according to the incident multiplicity distribution  $P(M_\gamma)$  of

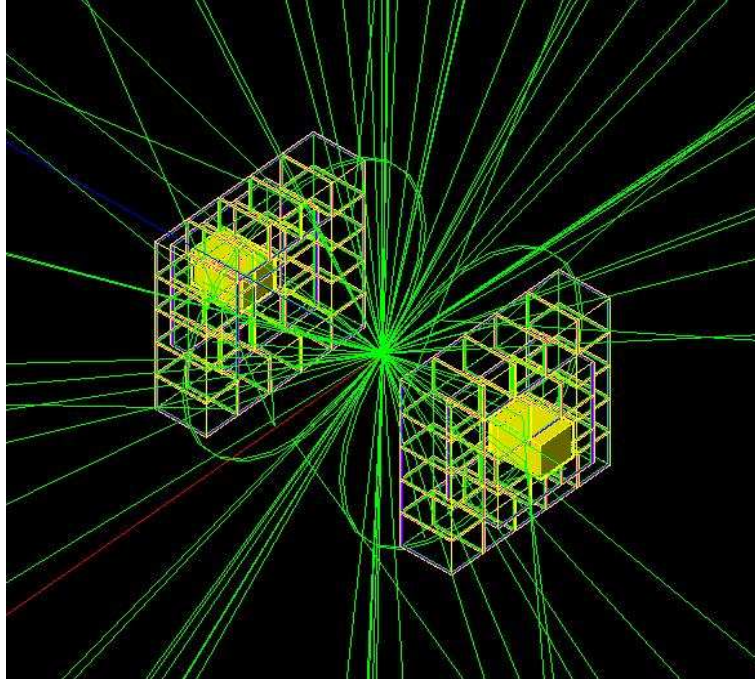


Figure 3.6: *Detector geometry of the  $\gamma$ -multiplicity filter using GEANT4 simulation code. The  $\gamma$ -rays are thrown using the Landau distribution.*

triangular shape and is given by:

$$P(M_\gamma) = \frac{2M_\gamma + 1}{1 + \exp[(M_\gamma - M_0)/\delta M]} \quad (3.1)$$

where,  $M_0$  is the maximum of this distribution and  $\delta M$  is the diffuseness. The energy distribution of the incident multiplicity was considered as a Gaussian with a peak at 0.35 MeV and width 0.65 MeV. The randomly generated low energy  $\gamma$ -rays were thrown isotropically from the target position. The fold corresponding to randomly generated multiplicity was recorded for each event. One million such events were triggered to record the final simulated fold spectrum. The angular momentum distribution for the reaction  ${}^4\text{He} + {}^{93}\text{Nb}$  was obtained from the statistical model code CASCADE. This CASCADE calculated angular momentum distribution was converted to multiplicity distribution using the formula  $J = 2M + C$ , where  $C$  is a free parameter which takes into account the angular momentum loss due to particle evaporation and emission of statistical

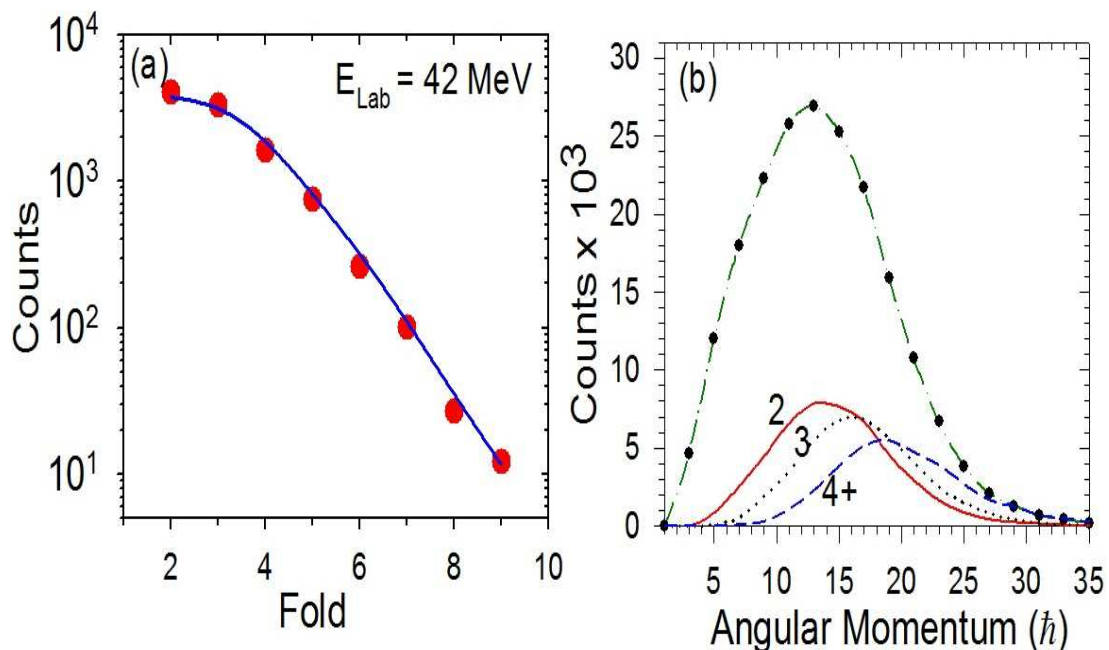


Figure 3.7: (a) Experimental fold distributions (filled circles) along with GEANT4 simulation (continuous line). (b) Angular momentum distribution for different folds ( $F$ ). The continuous, dotted and dashed lines represent the angular distributions for  $F=2$ , 3 and 4+, respectively. The symbols with dash-dotted line represent the total incident distribution ( $F \geq 2$ ).

$\gamma$ -rays. The parameters  $M_0$  and  $\delta M$  of the incident multiplicity distribution was obtained from the J-distribution by varying the free parameter  $C$  until the best fit between experimental fold distribution and simulated fold distribution was achieved. The best fitted simulated fold distribution (continuous line) along with the experimental fold distribution (filled circles) is shown in Fig 3.7 at  $E_{lab} = 42$  MeV. Next, the different fold gated multiplicity distributions were generated. Finally, these fold gated multiplicity distributions were converted to the angular momentum distributions (using the relation  $J = 2M + C$ ) which were used as inputs in the statistical model code CASCADE. The incident total angular momentum distribution (dot-dashed) and the angular momentum distributions corresponding to different folds (continuous line) are shown in Fig 3.7.

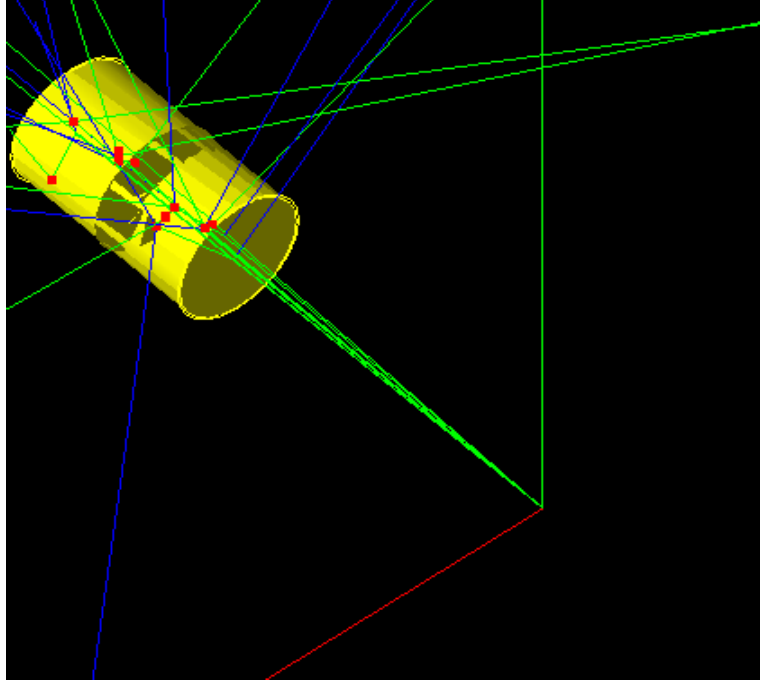


Figure 3.8: *Detector geometry of the liquid organic scintillator (BC501A) based neutron detector using GEANT4 simulation code.*

### 3.3.3 Simulation of BC501A neutron detector and its efficiency

For proper understanding of the neutron measurement, it is important to know the response function of the detector. The experimental neutron energy spectra must be normalized by the detector response (efficiency) before comparing with the theoretical calculation to determine the nuclear level density parameter. In this work, the intrinsic efficiency of the neutron detector has been measured using a spontaneous fission source  $^{252}\text{Cf}$  and compared with the GEANT4 simulation [Dey13]. In the simulation, the exact geometry of the experimental set-up (as shown in Fig 3.8) was taken into account. A liquid organic scintillator cylindrical in shape (5 inch in diameter and 5 inch in length) was placed at 150 cm from the centre of the target chamber. The detector threshold, TOF energy resolution, time resolution etc were properly considered. The TOF energy res-

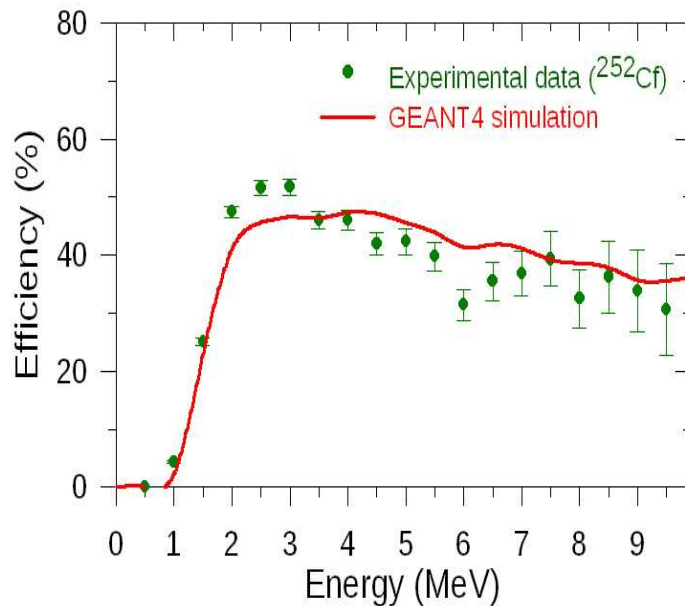


Figure 3.9: Energy dependent intrinsic neutron detection efficiency for neutron detector. The symbols represent the experimental data using  $^{252}\text{Cf}$  source and the continuous line represent GEANT4 simulation.

olution of the neutrons has been incorporated in the simulation by considering a Gaussian energy distribution ( $\Delta E$ ) which is given as [Goh12]

$$\left(\frac{\Delta E}{E}\right)^2 = \left(2\frac{\Delta T}{T}\right)^2 + \left(2\frac{\Delta L}{L}\right)^2 \quad (3.2)$$

where  $\Delta T$  is the time resolution of the detector,  $T$  is neutron flight time,  $L$  is neutron flight path,  $\Delta L$  is the flight path spread due to the detector size. The photo multiplier tube was not included in the simulation. Individual neutrons were generated by particle generator (G4ParticleGun) and tracked through the volume. Neutron interacts with the detector volume and produces charged particles and the scattered neutrons are tracked until they deposit all their energy in the defined detector volume or go out of the “World” volume. In the physics process the neutron induced interactions, such as radiative capture, elastic scattering, fission and inelastic scattering have been included. The G4NDL3.14, neutron cross-section library, has been used in GEANT4 simulation study for

neutron interaction. For  $\gamma$ -ray interaction, all the electromagnetic processes were included.

A conical beam of one million particles (neutron) in the energy range of 0.5 to 10 MeV are thrown into the front face of the detector keeping the same experimental configurations. The other essential aspects such as physics process, detector threshold, TOF energy resolution, time resolution, length uncertainty etc have been properly included. The intrinsic detection efficiency has been calculated by taking the ratio of the number of neutrons detected to the incident neutrons, properly normalized by solid angle. The simulated energy dependent detection efficiency along with the experimental data of  $^{252}\text{Cf}$  are shown in Fig 3.9. As can be seen from the Fig 3.9, the efficiency increases first up to 2 MeV and then decreases monotonically after 4 MeV. Hence, the neutron detection efficiency is very important before comparing the experimental data with theoretical calculation in order to estimate properly the nuclear level density parameter.

# Chapter 4

## Experimental Details and data analysis

The experiment was performed at the Variable Energy Cyclotron Centre, Kolkata, India using alpha beam from the K-130 cyclotron. A self-supporting foil of  $^{93}\text{Nb}$  (99.9% pure) with thickness of  $\sim 1 \text{ mg/cm}^2$  was used as the target. Four different beam energies of 28, 35, 42 and 50 MeV were used to form the compound nucleus (CN)  $^{97}\text{Tc}$  at initial excitation energies of 29.3, 36, 43 and 50.4 MeV, respectively. In this chapter, the details of the experiment, detector set-up and electronic set-up, data analysis and extraction of GDR parameters are discussed.

### 4.1 Detector set-up

The experimental set-up consists of three major detection systems which are given below :

- The LAMBDA spectrometer for measuring the high energy ( $>4 \text{ MeV}$ )  $\gamma$ -rays coming from the decay of the GDR built on highly excited states [Sup07].
- The  $\gamma$ -multiplicity filter for measuring the low energy discrete yrast  $\gamma$ -rays to extract the angular momentum populated in the compound nucleus [Dee10a].

- A liquid organic scintillator (BC501A) based neutron detector for measuring the evaporated neutrons from the compound nucleus to determine the nuclear level density parameter as well as the temperature of the compound nucleus [Ban07].

A part of the LAMBDA spectrometer consisting of 49 BaF<sub>2</sub> detectors, was arranged in a 7 × 7 matrix configuration for high energy  $\gamma$ -ray measurement. The spectrometer was placed at a distance of 50 cm from the target (covering 1.8% of  $4\pi$ ) at an angle of  $90^\circ$  with respect to the beam direction. Lead sheets of 3 mm thickness were kept in front and at the sides of the array to reject low energy  $\gamma$ -rays and X-rays. The  $\gamma$ -multiplicity filter was split into two blocks of 25 detectors each, in a staggered castle type geometry to equalize the solid angles for each multiplicity detector element, and placed at a distance of 5 cm above and below the centre of the scattering chamber. The solid angle covered by the multiplicity filter was  $\sim 55\%$  of  $4\pi$ . The geometric efficiency of the multiplicity set-up was 56% as calculated using GEANT4 simulation. All the detectors of the LAMBDA array and of the multiplicity filter array were gain matched so that a common threshold can be applied to all the detector modules. The liquid organic scintillator (BC501A) based neutron detector was placed at an angle of  $125^\circ$  with respect to the beam axis to avoid the pre-equilibrium neutrons and at a distance of 150 cm from the target. To keep the background ( $\gamma$  and neutrons originating from the beam dump) of the detectors at a minimum level, the beam dump was kept at a 3 m away from the target and well shielded with layers of lead bricks and borated paraffin blocks. Necessary arrangement was also taken to maintain the constant temperature of the total detector systems as the slow component of BaF<sub>2</sub> is highly temperature sensitive. The temperature inside the experimental hall was kept at  $18 \pm 1^\circ\text{C}$ . The typical experimental set-up has been shown in Fig 4.1.

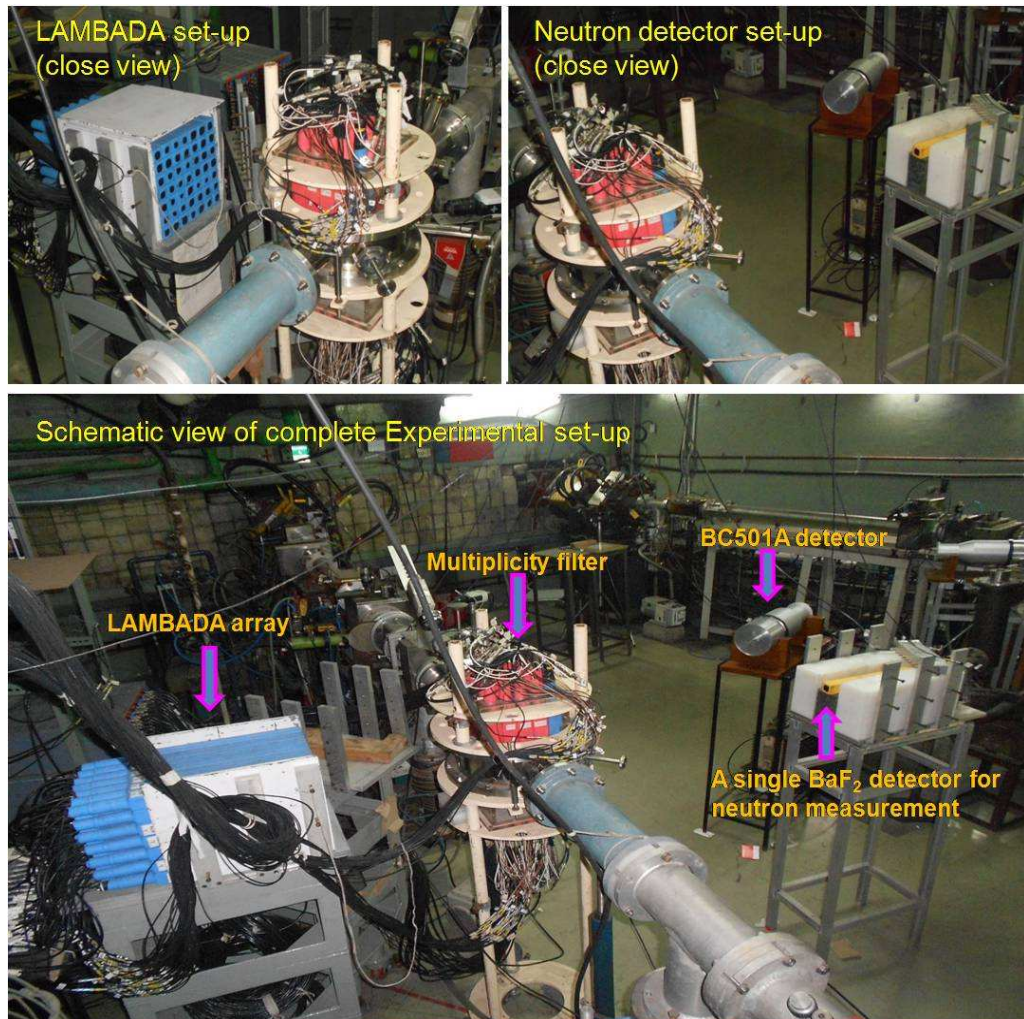


Figure 4.1: Schematic diagram of experimental set-up for GDR studies.

## 4.2 Electronic set-up

A dedicated CAMAC based front-end electronic setup was used to register the energy and time information from each detector element in an event by event mode. A dedicated VME based data acquisition (DAQ) system running under LINUX environment developed at VECC, was used to collect the data. All the electronic modules, detectors, bias supplies and the data acquisition (DAQ) system were kept inside the experimental hall and were controlled from outside through Ethernet. Fast, 32 channels VME charge to digital converter (QDC,

Model: CAEN V792) and time to digital converter (TDC, Model: CAEN V775) were used for collecting energy and time informations. These modules have a conversion time of  $5.6 \mu\text{s}$  for all its 32 channels and have a 12 bit resolution. The QDC can handle a maximum input charge of 400 pC while the TDC has a dynamic range of 140 ns to 1200 ns. The TDC and QDCs were operated in zero suppression mode. The data acquisition system can handle data up to 4 k/s. The diagram of the complete electronic set-up for the LAMBDA spectrometer along with the  $\gamma$ -multiplicity filter array has been shown in Fig 4.2. It should be mentioned that each of the 49 BaF<sub>2</sub> detectors in the LAMBDA spectrometer and 50 BaF<sub>2</sub> detectors in the  $\gamma$ -multiplicity filter were individually handled electronic wise. The details about the electronics of the LAMBDA spectrometer, multiplicity filter and liquid scintillator are discussed below.

### 4.2.1 Electronics for measuring the angular momentum gated high energy $\gamma$ -ray spectra

The individual detector outputs (total 49 outputs) from the LAMBDA spectrometer were first amplified using a fixed gain ( $\times 10$ ) fast wide band amplifier (CAEN N412). The amplified signals were split into two parts for the subsequent linear and logic paths

Each of the amplified signals (total 49 signals) in the linear path was delayed (by 100 ns) and divided into two parts with an amplitude ratio of 1:10, namely the attenuated and the unattenuated signal. This was done using a delay-splitter-cum-attenuation box designed in-house with analog IC chips. The attenuated and unattenuated signals were fed into four QDCs which integrate the charge contained in the signals and digitized it to give energy information. The integration on attenuated signal is called long integration whereas that on unattenuated signal it is termed as short integration. The duration of the long

and short integration gates were kept at  $2 \mu\text{s}$  and  $50 \text{ ns}$ , respectively. The amplitude ratio was chosen in such a way so that approximately equal amounts of charge were integrated under both long and short gates forming a  $\gamma$ -band making  $45^\circ$  slope in 2-dimensional long vs short gate spectrum (Pulse Shape Discrimination spectrum). It should be mentioned that the impedance adapter (CAEN A992) was connected in the input of QDCs box to match the input and output impedance and to block any DC offset present in the signal.

Each of the amplified signals (total 49 signals) in the logic path were further divided into two parts: one part was sent to Constant Fraction Discriminator (CFD) unit for timing measurement and other part was sent to Leading Edge Discriminator (LED) for generating a gate to integrate the charge contained in the linear signal. A high threshold ( $> 4 \text{ MeV}$ ) was applied in LED to select only the high energy  $\gamma$ -events. The LED output in coincidence with the multiplicity event (discussed in next paragraph) was used to generate an integration gate for energy measurement. The individual CFD outputs (with uniformly low threshold of  $300 \text{ keV}$ ) were delayed and used as individual STOP signals in the TDC for generation of the individual time spectrum for each elements of the LAMBDA array. The TDC unit was run in common START mode. The individual detector outputs (total 50 outputs) from the multiplicity filter (TOP MULT and BOTT MULT as shown in Fig 4.2) were fed into four CAMAC based CFD unit (CAEN 808). Each of the CFDs has two parallel outputs, an OR and a SUM output. The SUM outputs from the CFDs were summed in a Linear-Fan-in module. The output of the Linear-Fan-in module was fed into a QDC and integrated for a gate duration of  $50 \text{ ns}$  to generate the experimental fold distribution on event-by-event basis. The logic OR signals from each of four CFDs were sent to two logic FAN-IN FAN-OUT units, one for TOP multiplicity filter and another for BOTTOM multiplicity filter. These two logic

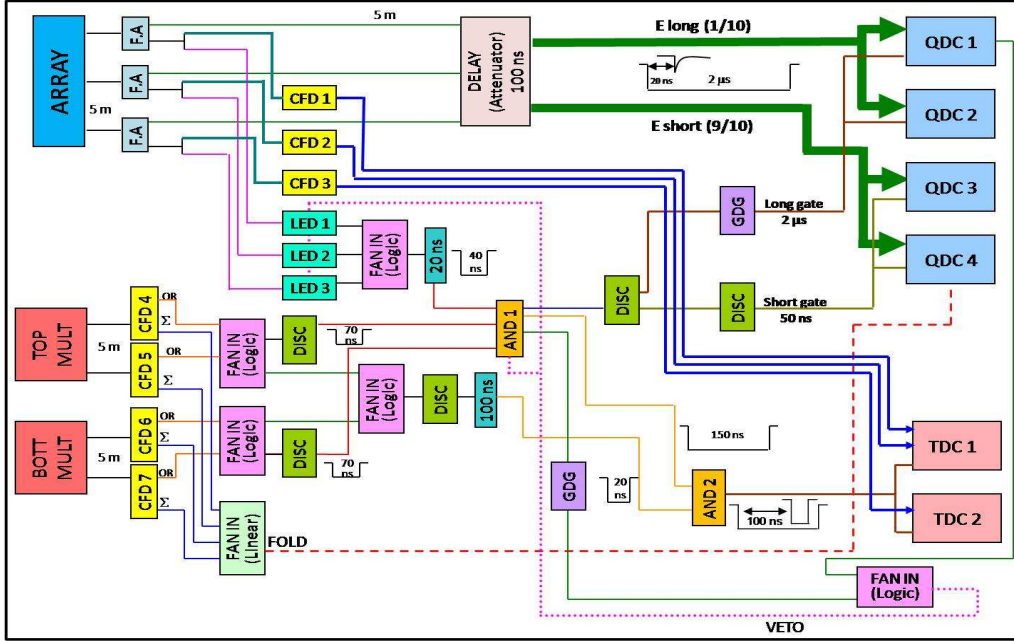


Figure 4.2: Schematic diagram of electronics set-up for LAMBDA array and multiplicity filter.

FAN-IN FAN-OUT units serve as a logical SUM to the OR-ed outputs from the discriminator. The fanned out signals from both the TOP and BOTTOM multiplicity filter and the signals from LEDs were sent to a coincidence unit (AND1) to generate the master trigger which was used to generate the QDC gate. It should be mentioned that all the detector elements in the LAMBDA array and the  $\gamma$ -multiplicity filter array were properly matched in time individually using delays and cables of equal lengths.

A level-1 trigger(A) was generated from the multiplicity filter array when at least one detector each from the top and bottom blocks fired in coincidence above a threshold of 250 keV. Another trigger (B) was generated when the signal in any of the detector elements of the LAMBDA spectrometer crossed a high threshold of 4 MeV. A coincidence of these two triggers (A and B) generated the master trigger ensuring the selection of high energy  $\gamma$ -events and

rejection of backgrounds. This master trigger was used to generate the QDC integration gate for energy information. For timing measurement, the START trigger was taken from the master trigger and the STOP trigger was taken from the individual CFD delayed outputs of the LAMBDA array. For each of the detector elements of the LAMBDA array, the long gate and short gate integrated energies and time were recorded for each triggered event.

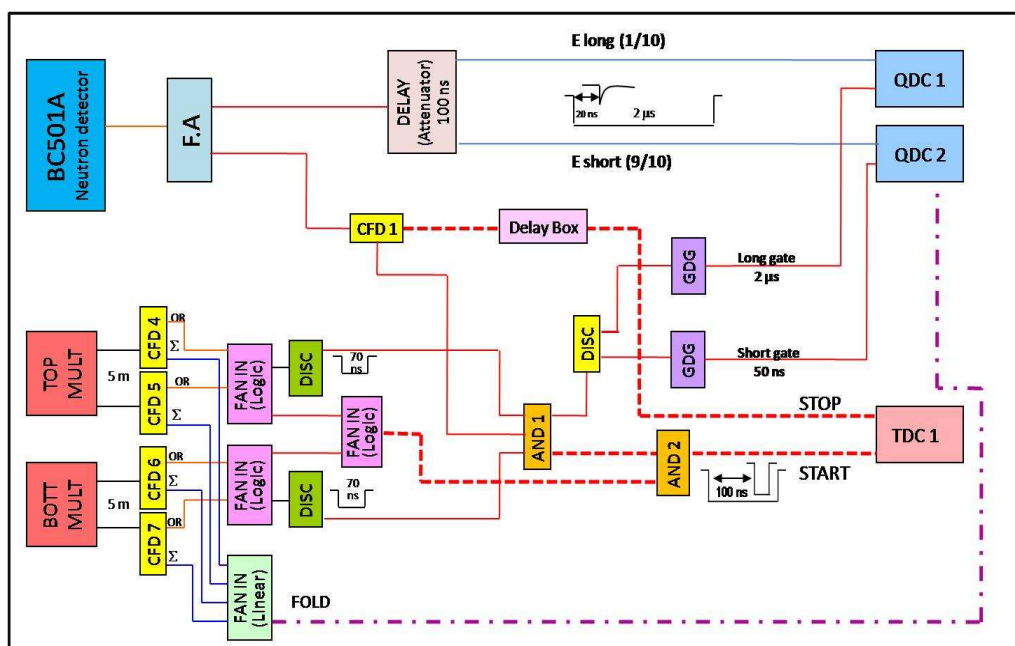


Figure 4.3: Schematic diagram of electronics set-up for BC501A neutron detector.

## 4.2.2 Electronics for neutron energy measurement

The liquid organic scintillator (BC501A) based neutron detector was used to measure the evaporated neutron energy spectrum by time-of-flight (TOF) technique. The PMT (Photo Multiplier Tube) output of the liquid organic scintillator was first amplified using a fixed gain fast amplifier and then sent to a CFD unit. The trigger generated from the multiplicity filter in coincidence with CFD output from BC501A was used as the common START trigger whereas

the STOP trigger was taken from the delayed CFD output for the neutron TOF measurement. The time difference between START and STOP trigger separates the neutrons from  $\gamma$ -rays, and ultimately gives the energy information of the neutrons. In the TOF technique, the low energy neutron can easily be separated

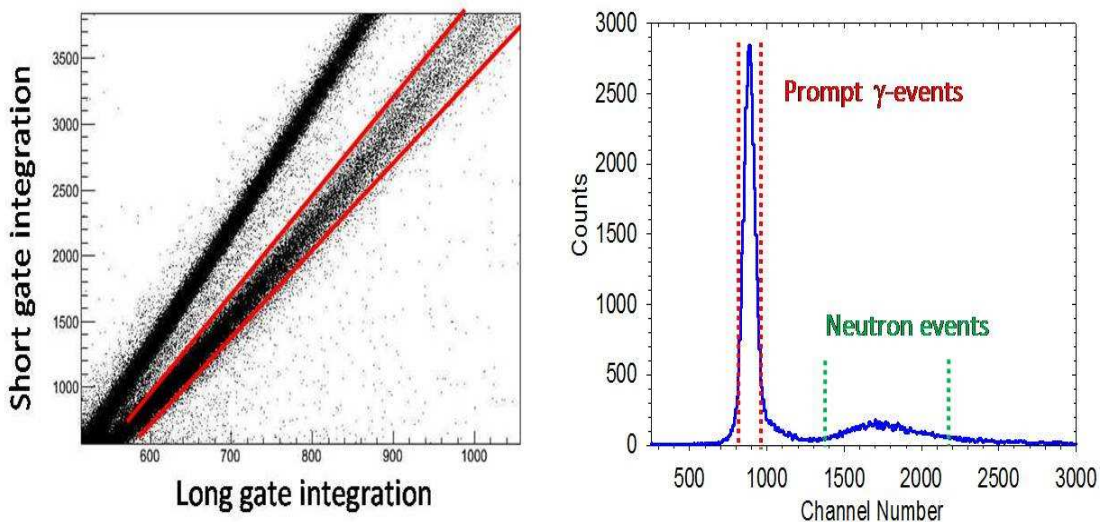


Figure 4.4: *The pulse shape discrimination and time-of-flight spectrum of liquid scintillator.*

from the  $\gamma$ -rays, but there is a high possibility of high energy neutrons mixing with the  $\gamma$ -rays. High energy neutrons can then only be separated by pulse shape discrimination (PSD) technique using 2-dimensional long vs short gate spectrum. The long and short integration were performed same as explained in the section of LAMBDA electronics. Finally, the neutron events were well separated from the  $\gamma$ -events using both the TOF and PSD techniques. The TOF and PSD spectrum has been shown in Fig 4.4. A clean neutron TOF spectrum can be obtained using a proper gate on the neutron events. Along with the TOF and PSD spectrum, the pulse height spectrum has also been measured to apply energy thresholds in off-line analysis. The data have been collected in event by event mode including the experimental fold (F) distribution with conditions ( $F \geq 2$ ). The electronic set-up for liquid scintillator for neutron measurement is

shown in Fig 4.3.

### 4.3 Detectors calibration

All the BaF<sub>2</sub> detectors in the LAMBDA array were calibrated for energy information using the laboratory standard  $\gamma$ -ray sources and minimum ionizing cosmic muons. The low energy calibration points were obtained from the sources  $^{22}\text{Na}$ (0.511 MeV, 1.274 MeV),  $^{241}\text{Am-}^9\text{Be}$ (4.43 MeV) whereas the high energy calibration point was obtained from the minimum ionizing cosmic muons (23.1 MeV). The typical  $\gamma$ -ray energy spectra for  $^{22}\text{Na}$  and  $^{241}\text{Am-}^9\text{Be}$  are shown in Fig 4.5. Due to the high granularity of the array, the  $\gamma$ -ray (4.43 MeV) from  $^{241}\text{Am-}^9\text{Be}$  source do not deposit its full energy in the detector and is mostly dominated by the first escape peak. During off-line analysis, the prominent full energy peak is obtained by putting a condition (no-leak condition) that only one detector has fired in that event. The spectrum for both leak and no-leak condition are shown in Fig 4.5. Minimum ionizing cosmic muons deposit 6.6

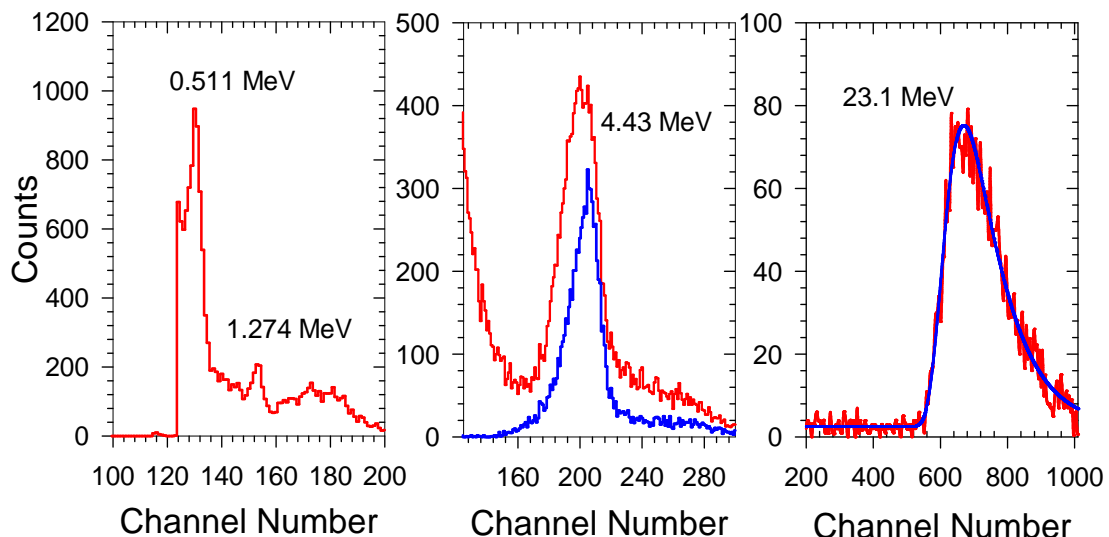


Figure 4.5: LAMBDA detector calibration using laboratory standard sources  $^{22}\text{Na}$  and  $^{241}\text{Am-}^9\text{Be}$ . The cosmic muons are used for high energy (23.1 MeV) calibration point.

MeV/cm in BaF<sub>2</sub> crystal. While passing through a single detector (3.5 cm) vertically in the array, they deposit a minimum of 23.1 MeV energy in the detector element. In order to get the high energy calibration point (23.1 MeV), the cosmic muons spectrum is generated in off-line analysis by selecting those events in which all the seven detectors in a vertical column have fired. Utilizing this fact, the whole array (arranged in  $7 \times 7$  matrix form) can be calibrated within a very short time. The cosmic muons spectrum is fitted by a Landau function (as shown in Fig 4.5) to get the corresponding channel number for 23.1 MeV. It is observed that (as shown in Fig 4.6) that the energy response of each BaF<sub>2</sub> detector in the LAMBDA array is linear at least up to 23.1 MeV. The array was calibrated frequently to keep the same gain of all the detector elements in the LAMBDA spectrometer.

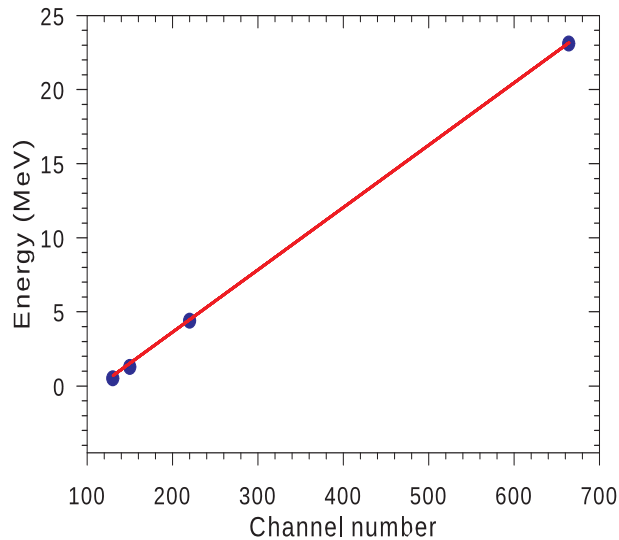


Figure 4.6: A typical energy calibration curve obtained from a single BaF<sub>2</sub> detector using low energy lab standard sources <sup>22</sup>Na (0.511 MeV, 1.274 MeV) and <sup>241</sup>Am-<sup>9</sup>Be (4.43 MeV). The high energy (23.1 MeV) calibration point was taken by measuring the cosmic muons.

## 4.4 Data reduction technique

Several backgrounds are present in the high energy  $\gamma$ -ray spectra. Those are neutron events, pile-up events, cosmic events, etc. It is therefore essential to reject those backgrounds from the high energy  $\gamma$ -ray spectra. A detailed off-line analysis has been performed under the framework of CERN ROOT [Bru86] to extract the meaningful spectra from the list mode data employing different cuts and rejections. The rejection of these backgrounds are discussed as follows.

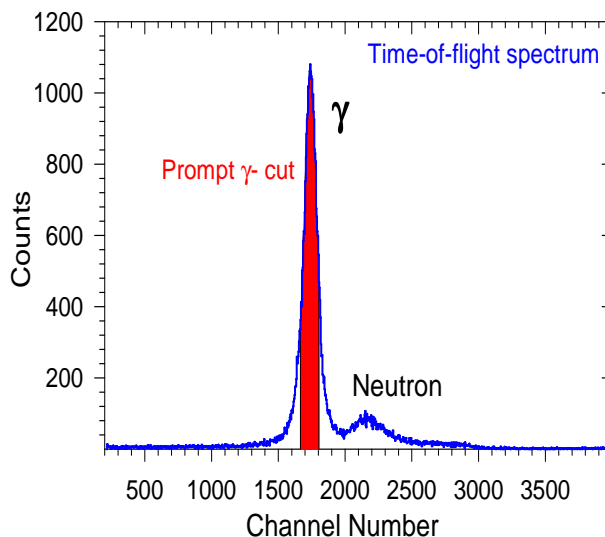


Figure 4.7: The experimental time-of-flight spectrum obtained from a single  $\text{BaF}_2$  detector of the LAMBDA array. The selection of prompt  $\gamma$ -band is shown with the filled region.

### 4.4.1 Rejection of neutron backgrounds

The evaporated neutrons from the compound nucleus are the major source of contamination in the high energy  $\gamma$ -spectra. Slower neutrons ( $E < 10$  MeV) mainly interact in the  $\text{BaF}_2$  material through  $(n,\gamma)$  or  $(n,n'\gamma)$  reactions and deposit their energy in the detector as photons, whereas fast neutrons ( $> 10$  MeV) interact in the  $\text{BaF}_2$  material through  $(n,p)$  or  $(n,n'p)$  reactions and deposit their energy by proton ionization in the detector volume. Therefore,

due to different interaction mechanisms of slow and fast neutrons, it is very difficult to separate the slow neutron by PSD technique only. These slower neutrons were effectively discriminated using TOF technique by the selection of prompt  $\gamma$ -window in the TOF spectrum (as shown in Fig 4.7).

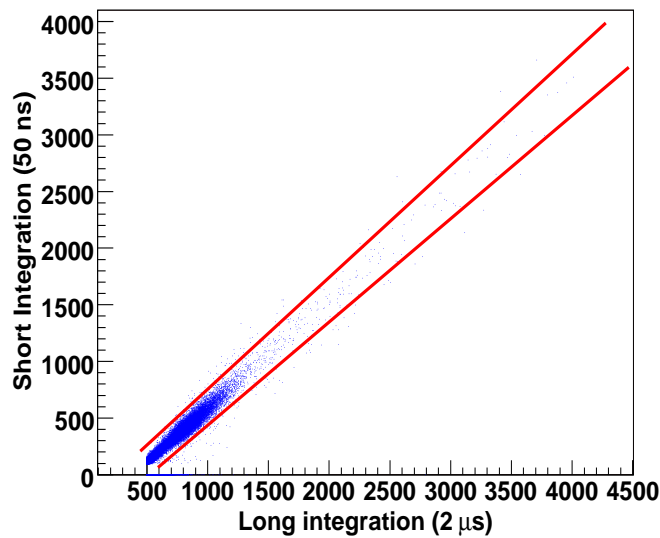


Figure 4.8: A two dimensional pulse shape discrimination spectrum. The selection of the  $\gamma$ -band is shown with continuous line.

#### 4.4.2 Rejection of pile-up events

Pile-up events mainly occur when along with a valid high energy  $\gamma$ -event in a single detector element, another photon or neutron enters the same detector element while the integration gates are open. These pile-up events are purely random in nature. The pile-up events were rejected by PSD method. In PSD method, a 2-dimensional long vs short gate spectrum was taken. The  $\gamma - \gamma$  or  $\gamma$ -n hits in the same element in the same event during the integration will result in different ratio of long vs short integrated charge and appear away from the

true  $\gamma$ -band as shown in Fig 4.8. Therefore, a suitable selection of true  $\gamma$ -band, which rejects the pile-up events, is very important. Due to the large granularity of the spectrometer, the probability of pile-up events are very small, but it is required to select a proper gate on the  $\gamma$ -band in 2-dimensional long vs short gate spectrum to extract a clean data.

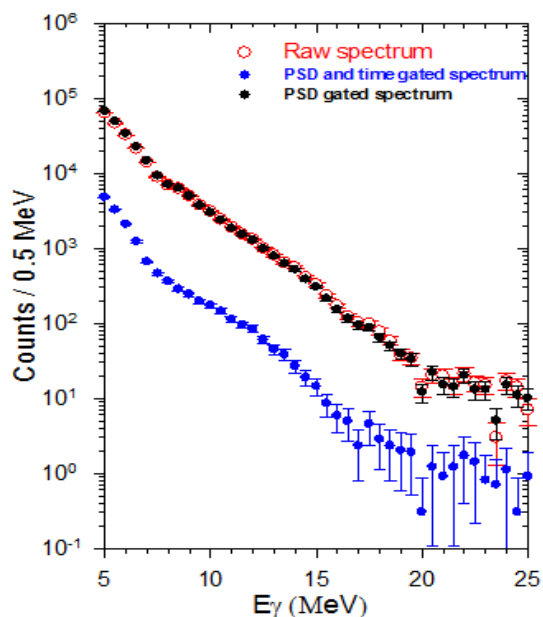


Figure 4.9: *The effect of different cuts and rejections on the raw high energy  $\gamma$ -ray spectrum. The red opened circles are the raw high energy  $\gamma$ -ray spectrum, black filled circles are PSD gated high energy  $\gamma$ -ray spectrum and blue filled circles are PSD and time gated high energy  $\gamma$ -ray spectrum.*

#### 4.4.3 Cosmic event rejection

The deposited energy by the cosmic muons in the detector volume can easily be rejected by looking at the hit pattern in the array. The cosmic muons, being minimum ionizing radiation, produce a linear track in the LAMBDA array whereas the high energy  $\gamma$ -ray produce a cluster. The hit pattern of cosmic muons coming from the top and sides of the spectrometer is completely different from that of the high energy  $\gamma$ -ray. Typical cosmic muon tracks in

the spectrometer are shown in Fig 4.10 whereas the hit patterns for high energy  $\gamma$ -rays are shown in Fig 4.11. When a cosmic muon is passing vertically through the array, it deposits a large amount of energy (23.1 MeV) in a single detector of the array. For diagonal and oblique incidence, the energy deposit may be still larger. While reconstructing the pure events using cluster summing technique, these cosmic events contribute to a very high energy ( $> 40$  MeV) much above the region of interest and therefore rejected. During off-line analysis, these muons are effectively rejected due to their unique hit patterns in the array. Moreover, the triggered data acquisition system was kept in such a way that the probability of detection of the cosmic events in coincidence with a high energy  $\gamma$ -events is very small.

## 4.5 Measurement of high energy $\gamma$ -rays using cluster summing technique

The high energy  $\gamma$ -spectra were generated in an event-by-event mode during off-line analysis. When a high energy  $\gamma$ -ray is incident on a single detector element in the array, it may deposit its complete energy to the detector or may scatter to its neighbouring detector element. Therefore, to collect the full information of a single event, it is important to confine the scattered events within the array. Two methods can be applied to reconstruct a single event: one is the total summing of the array and another one is nearest neighbour summing (cluster summing). In the first case, all the unwanted events i.e pile-up ( $\gamma$ - $\gamma$ , n- $\gamma$ ), cosmic events etc can not be separated from the actual event. Therefore, instead of taking the total summing, the cluster summing technique has been used to reconstruct the events for collecting clean  $\gamma$ -spectra. In the cluster summing technique, first, the detector with highest energy deposit above a high energy threshold ( $> 4$  MeV) within the array was checked and identified

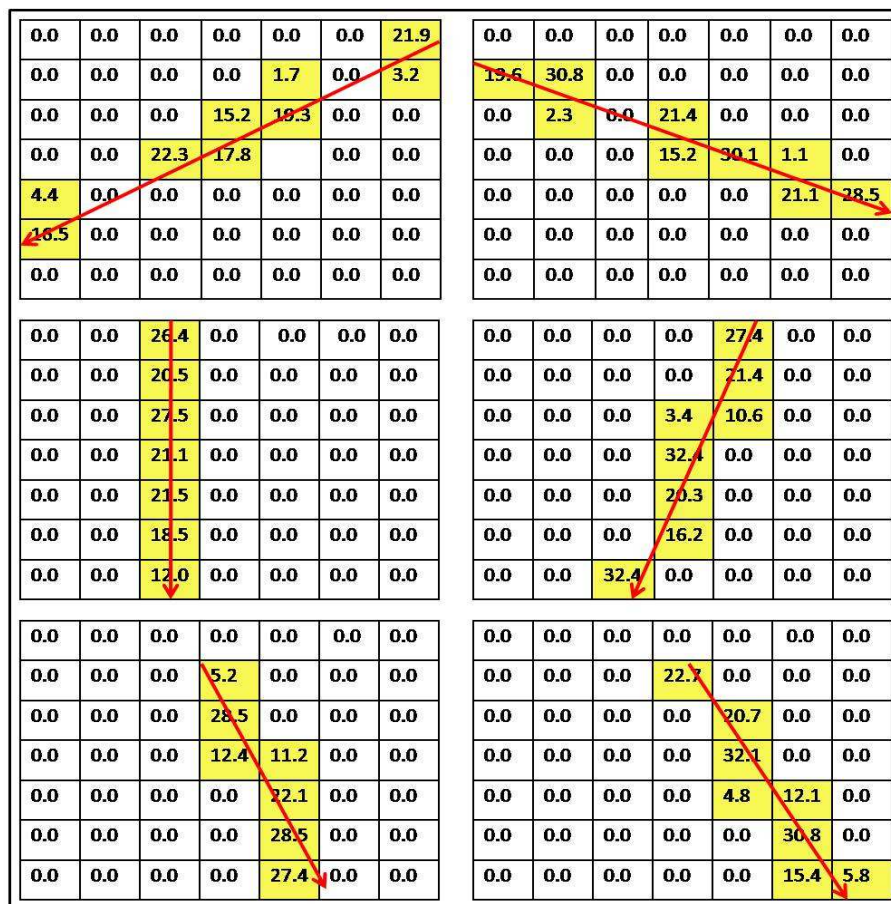


Figure 4.10: The typical cosmic muon tracks in LAMBDA spectrometer arranged in  $7 \times 7$  matrix. The direction of the muon tracks are shown by the arrows along with the actual energy deposits in the detector elements. .

as primary detector. The high energy  $\gamma$ -ray can hit the outer most detector in the array and it may go outside the detector without depositing full energy. Therefore, the primary detector was checked that whether it was surrounded by all of its nearest neighbours (8 detectors) or not. The events corresponding to primary detector surrounded by all its nearest neighbour detectors, were only selected as valid events, whereas the events for outer most primary detector were rejected. In this way, the valid cluster ( $3 \times 3$ ) was selected in a single event. All the nearest neighbour 8 detectors were kept at a minimum threshold (150 – 200 keV) as much as possible. Before summing all the nine detector



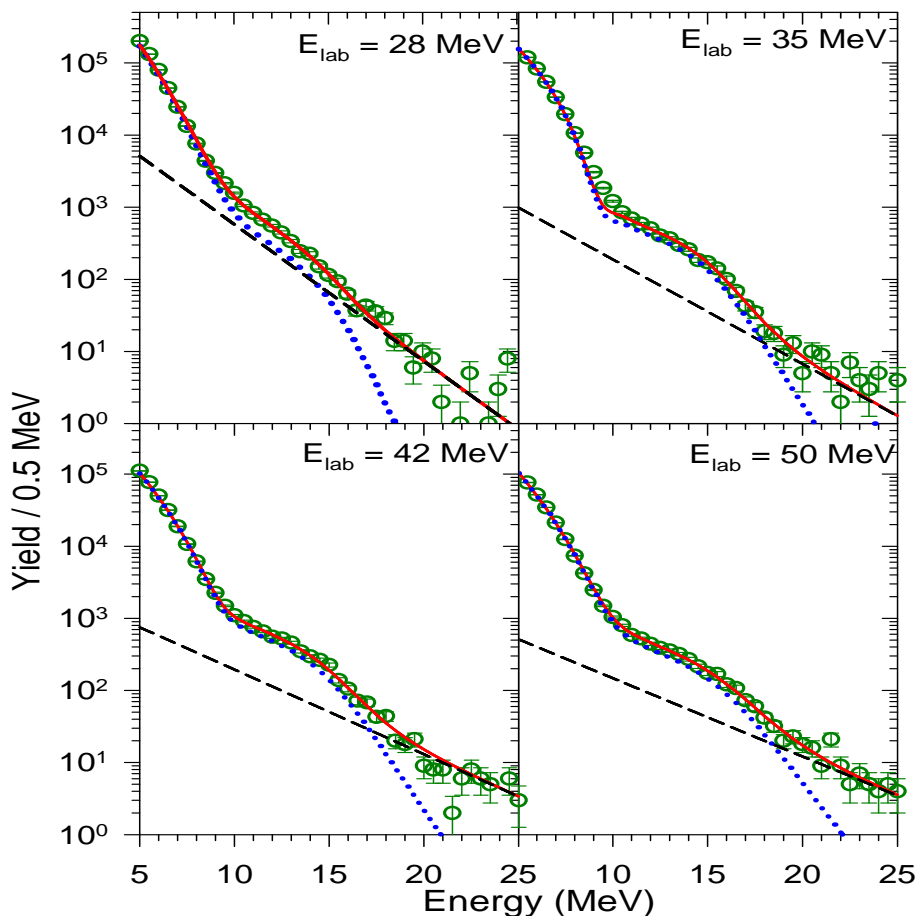


Figure 4.12: The high energy  $\gamma$ -ray spectra (filled circles) along with the statistical model CASCADE calculation (continuous line) for the system  ${}^4\text{He} + {}^{93}\text{Nb}$  at four incident energies  $E_{\text{lab}} = 28, 35, 42$  and  $50$  MeV. Dashed line represents the bremsstrahlung contribution whereas dotted line represents the CASCADE calculation without bremsstrahlung component.

The maximum value of  $\beta$  in this experiment was  $\sim 0.0067$  and the angular position of the outer most cluster in the array was  $78.8^\circ$ . At  $E_{\text{clus}} = 15$  MeV, the maximum Doppler correction was  $\sim 20$  keV which is negligibly small. The contributions from the target holder due to the presence of beam halo, if any, were subtracted using a blank frame run. Any contributions from the chance coincidence events within the prompt  $\gamma$ -window in the TOF spectrum were also subtracted. Finally, the Doppler corrected high energy  $\gamma$ -ray spectra were generated for each beam energy by gating on different coincidence folds (F)

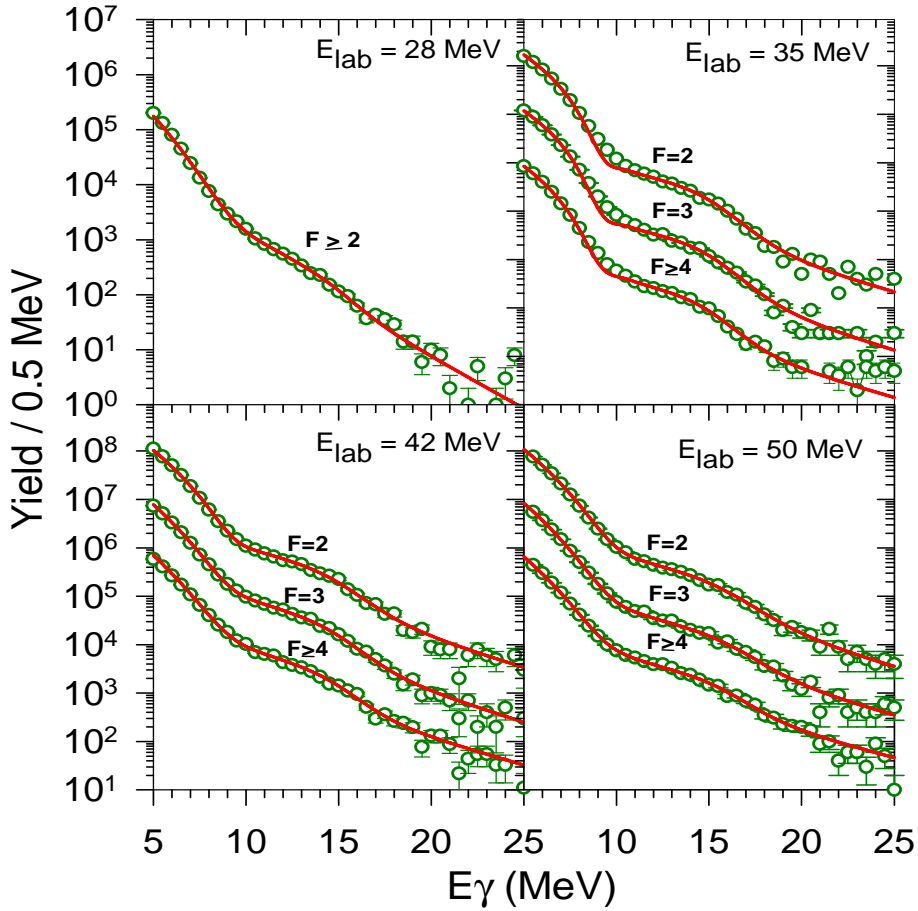


Figure 4.13: The high energy  $\gamma$ -ray spectra (filled circles) along with the statistical model CASCADE calculation (continuous line) for the system  ${}^4\text{He} + {}^{93}\text{Nb}$  at four incident energies  $E_{\text{lab}} = 28, 35, 42$  and  $50$  MeV.

of low energy  $\gamma$ -multiplicities in the  $\gamma$ -multiplicity filter. The high energy  $\gamma$ -ray spectra along with the different theoretical components are shown in Fig 4.12. All the angular momentum gated high energy  $\gamma$ -spectra for four incident energies are shown in Fig 4.13.

## 4.6 Extraction of angular momentum

The knowledge of angular momentum distribution of the compound nucleus is essential to extract the GDR parameters. The angular momentum distribution is required as an input in the CASCADE code for calculating the rotational

energy to properly estimate the compound nucleus temperature. The angular momentum distributions were measured from the multiplicity distribution of the low energy discrete  $\gamma$ -rays. The detailed procedure to measure the angular momentum distribution has been discussed in the previous Chapter (Section 3.3.2). The angular momentum distributions for different projectile energy along with the multiplicity fold distributions are shown in Fig 4.14. The value of angular momentum for different fold at different projectile energies are displayed in Table 4.1.

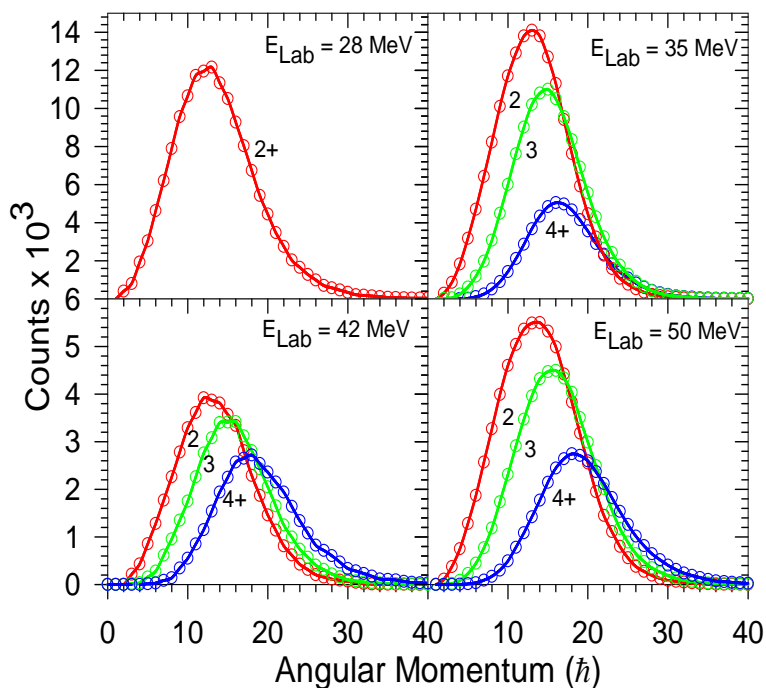


Figure 4.14: Simulated angular momentum distributions for the system  ${}^4\text{He} + {}^{93}\text{Nb}$  at four incident energies  $E_{lab} = 28, 35, 42$  and  $50$  MeV.

## 4.7 Measurement of evaporated neutron energy spectrum

The evaporated neutron energy spectra were measured using a liquid organic scintillator (BC501A) by TOF technique. The experimental set-up for neutron

measurement is shown in Fig 4.1. For the TOF measurement, the START signal was taken from the multiplicity filter, whereas the STOP signal was from the liquid organic scintillator. The TOF spectrum along with the PSD spectrum of liquid organic scintillator are shown in Fig 4.4. The PSD gated TOF spectrum was converted to energy spectrum using the prompt  $\gamma$ -peak as a time reference. The neutron energy spectra were then corrected by incorporating the energy dependent neutron detection efficiency. The procedure of extraction the energy dependent neutron detection efficiency have been discussed in details in References [Ban07, Dey13]. The efficiency corrected neutron energy spectra

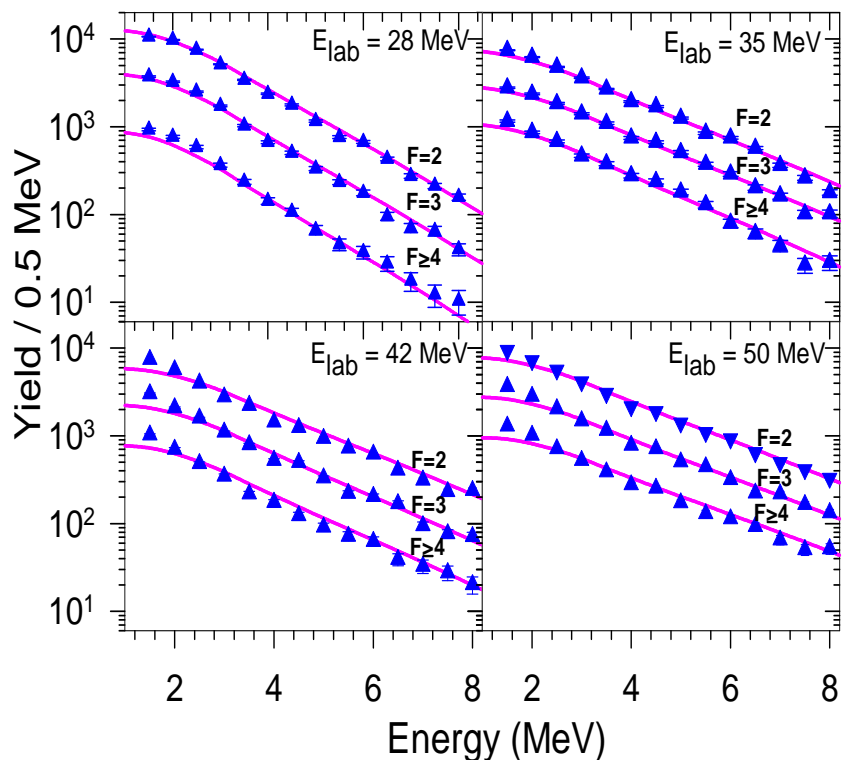


Figure 4.15: The neutron energy spectra (filled triangles) measured using liquid organic scintillator (BC501A) based neutron detector along with the statistical model CASCADE calculation (continuous line) for the system  ${}^4\text{He} + {}^{93}\text{Nb}$  at four incident energies  $E_{\text{lab}} = 28, 35, 42$  and  $50$  MeV for different fold values.

were further transformed to centre of mass frame from laboratory frame. The theoretical neutron energy spectra were calculated using the statistical model

code CASCADE [Puh77]. In the CASCADE code, the Ignatyuk level density prescription [Ign75] was used. The theoretical neutron energy spectra were then fitted with the experimental neutron energy spectra using  $\chi^2$ -minimization technique in the energy range of 3–7 MeV to determine the nuclear level density parameter. The final neutron energy spectra along with the corresponding CASCADE calculations (continuous line) for different folds are shown in Fig 4.15. The extracted level density parameters for different folds and excitation energies are displayed in the Table 4.1.

### 4.7.1 Calculation of compound nucleus temperature

The proper estimation of compound nucleus temperature is required for a realistic comparison between the theoretical predictions and the experimental results. The nuclear temperature is related to the excitation energy ( $E$ ) via the definition of nuclear level density  $\rho(E)$ . The entropy can be defined as  $S(E) = \ln[\rho(E)]$ . The relation between nuclear temperature  $T$  and entropy  $S$  is

$$\frac{1}{T} = \frac{dS}{dE} = \frac{d}{dE} \ln[\rho(E)] \quad (4.1)$$

The nuclear level density is related to the available excitation energy  $U$  as

$$\rho(U) \propto \exp[2\sqrt{aU}] \quad (4.2)$$

Now using the form of NLD from Eqn.(4.2), the nuclear temperature can expressed as

$$T = \sqrt{\frac{U}{a}} \quad (4.3)$$

where  $a$  is the NLD parameter and  $U = E^* - E_{GDR} - E_{rot} - \Delta$  is the available excitation energy in the compound nucleus. The GDR energy ( $E_{GDR}$ ), rotational energy ( $E_{rot}$ ) and pairing energy ( $\Delta$ ) are not thermal in nature and hence, they

are subtracted from the initial excitation energy ( $E^*$ ) to properly estimate the nuclear temperature for GDR experiments. At high excitation energy, the compound nucleus decays through a large number of intermediate steps, and hence the mass ( $A$ ), charge ( $Z$ ), excitation energy ( $E^*$ ), angular momentum ( $J$ ) and temperature ( $T$ ) of the compound nucleus should be averaged over all the decay steps. While estimating the average temperature, a lower limit in the excitation energy ( $E^*$ ) during the CN decay process was employed in the statistical model calculation in accordance with the prescription described in References [Wie06, Sri08a]. This lower limit in  $E^*$  is selected when the cut off in the excitation energy only affects the low energy part of the high energy  $\gamma$ -ray spectra, without affecting the region of our interest  $E_\gamma = 10-25$  MeV. The average values of mass, atomic number, excitation energy and angular momentum were calculated within the above mentioned  $E^*$  limit. The average temperature was calculated using the relation

$$\bar{T} = \sqrt{\frac{E^* - \Delta - \bar{E}_{rot} - E_{GDR}}{a(\bar{E}^*)}} \quad (4.4)$$

where  $\bar{E}_{rot} = \hbar^2 \bar{J}(\bar{J}+1)/\mathcal{I}$  is the energy bound in the rotation at the  $\bar{J}$  and  $E_{GDR}$  is the GDR centroid energy.  $a(\bar{E}^*)$  is the energy dependent NLD parameter computed at  $\bar{E}^*$ .  $\bar{E}^*$  is the average excitation energy, weighted over the decay chain of the compound nucleus for GDR  $\gamma$ -ray emission in the region  $E_\gamma = 10-25$  MeV, can be represented as  $\bar{E}^* = \sum E_i^* w_i / \sum w_i$ , where  $E_i^*$  is the excitation energy of  $i^{th}$  nuclei in the decay steps and  $w_i$  is the yield in the region  $E_\gamma = 10-20$  MeV.

It should be pointed out that the exact knowledge of NLD parameter  $a(E^*)$  is not only the crucial for statistical model calculation but also vital for the precise estimation of nuclear temperature. In the present work, this parameter has been experimentally extracted from the simultaneous measurement of evaporated

neutron energy spectra.

### 4.7.2 The effect of nuclear level density formalism on the high energy $\gamma$ -ray spectra

To understand the properties of the GDR parameters in order to infer the nuclear structure, the characterization of the high energy  $\gamma$ -rays and its comparison with the predictions of theoretical statistical model related to CN decay is absolutely necessary. However, the success of any statistical model depends on the knowledge of the nuclear level density. This is the central source of error in extracting the GDR parameters. An ideal nuclear level density formalism should describe the level density correctly starting from lower to higher  $E^*$  and at different  $J$  values. It should also incorporate shell effects at lower  $E^*$  smoothly connecting to the liquid drop behavior of the nucleus at higher  $E^*$  and it must describe the high-energy  $\gamma$ -ray spectra faithfully. The Puhlhofer's statistical model code CASCADE [Puh77], that incorporates Dilg formalism for nuclear level densities [Dil73], induces large uncertainty in the explanation of high energy  $\gamma$ -rays due to non-inclusion of the proper treatment of the shell corrections and its washing out at higher excitation energies along with the effect of nuclear deformation. At present, only a few level density formalisms exist which incorporate the proper inclusion of shell effects and its extrapolation at higher excitation energies. The formalism predicted by Ignatyuk, Smirenkin and Tishin [Ign75] is highly popular due to its easy to use lucid mathematical formulae and inclusion of shell effects. Besides, two other nuclear level density formalisms given by Kataria, Rammurthy and Kapoor [kat78] and Budtz-Jorgensen and Knitter (BJK) [Bud88] exist that are easy to use and also include shell effects in different ways. While in the BJK level density formalism, mass-dependent level density parameters were extracted from the neutron evaporation measurements in the spontaneous fission of  $^{252}\text{Cf}$ , the Kataria formalism proposes the

ground state shell correction as a perturbation term along with the shell independent level density. To understand the role of nuclear level density on

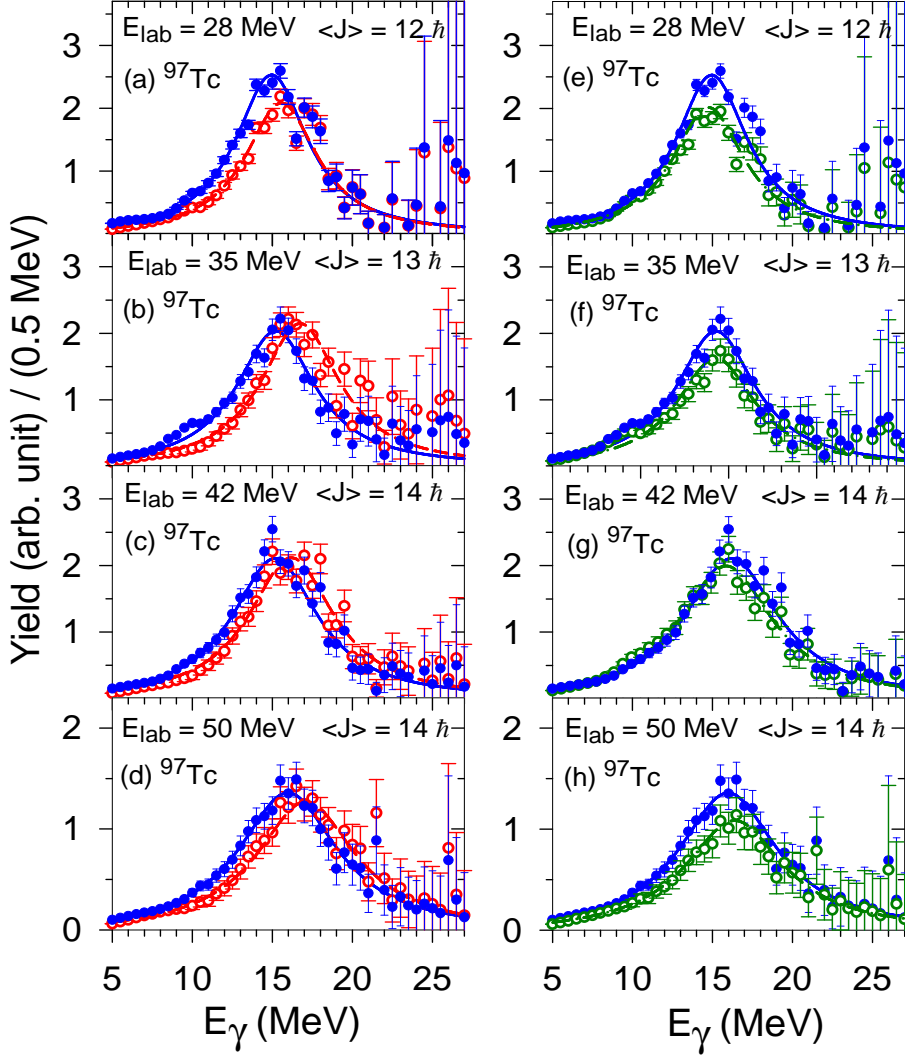


Figure 4.16: Panels (a) to (d): The experimental linearized plots for the reaction  $^4\text{He} + ^{93}\text{Nb}$  at projectile energies 28, 35, 42 and 50 MeV along with CASCADE predictions utilizing KRK (open circles with red dashed line) and IST (filled circles blue continuous line) level density formalisms. Panels (e) to (h): Same as above but utilizing BJK (open circles with green dotted-dashed line) and IST (filled circles with blue continuous line) level density formalisms.

the high energy  $\gamma$ -ray spectra, the experimental high-energy  $\gamma$ -ray spectra for  $^{97}\text{Tc}$  at excitation energies  $E^* = 29.3, 36.0, 43.0,$  and  $50.4$  MeV were compared with CASCADE predictions utilizing Ignatyuk [Ign75], Kataria [kat78] and BJK

[Bud88] formalisms in this work (as shown in Fig 4.16). Though Ignatyuk prescription successfully predicted the data keeping the extracted best fit  $E_{GDR}$  at 15.6 MeV as per existing GDR systematics, Kataria prescription could only predict all the data for  $E_{GDR} = 17.0\text{--}17.5$  MeV, much higher than the established GDR energy systematics. On the contrary, BJK also successfully predicted the data for  $E_{GDR} = 15.0\text{--}16.8$  MeV.

For some definite conclusion, all the three prescriptions were tested not only on the GDR data of  $^{97}\text{Tc}$  but also on that of  $^{113}\text{Sb}$ ,  $^{201}\text{Tl}$  and  $^{63}\text{Cu}$  nuclei [Sri14]. After a thorough investigation starting from the regime of lower to higher masses, lower to higher excitation energies and with different average angular momenta along with lower to higher values of shell corrections, it was found that Ignatyuk prescription represent the data best in all possible conditions. The problem with the Kataria prescription is that, it can only predict correctly the high energy  $\gamma$ -ray spectra if  $E_{GDR}$  is taken much larger than the systematics. BJK can only predict a data if the level density parameter for the corresponding nucleus exists in its compilation [Bud88]. Again, the level density parameter under BJK is excitation energy independent which introduces errors in it. More over, BJK can successfully predict the data if and only if  $E_{GDR}$  is taken lower than the value from systematics. In this investigation, for all the three prescriptions in a particular nucleus at a certain value of  $E^*$  and  $J$ , the GDR width remains constant but  $E_{GDR}$  changes. The details of this work has been discussed in Reference [Sri14].

The extracted value of  $E_{GDR}$ , in all the cases, is closer to the existing systematics of GDR under Ignatyuk prescriptions in comparison to the other two prescriptions. The extraction of correct values of  $E_{GDR}$  is highly important in case of GDR studies as it introduces systematic error in the estimation of CN temperature. Hence, Ignatyuk prescription [Ign75] of nuclear level density has

been used in this thesis work.

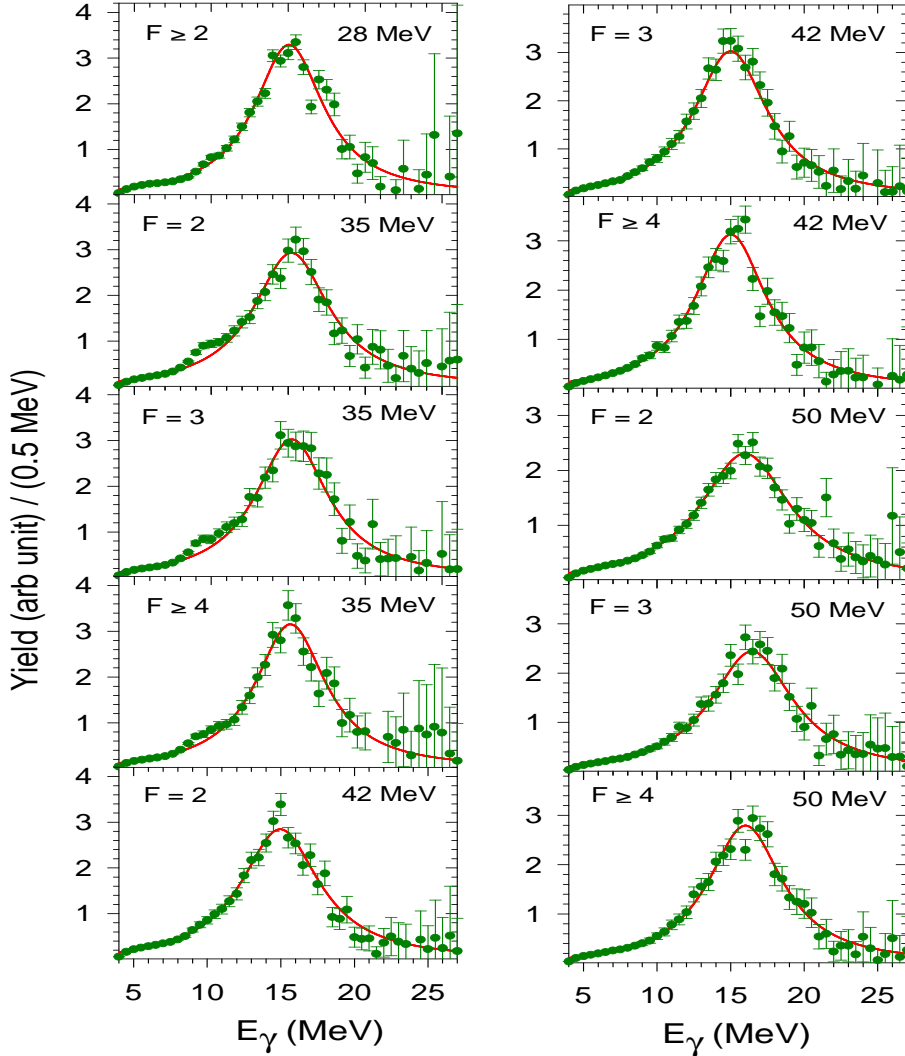


Figure 4.17: Linearized plots of the measured  $\gamma$ -spectra (filled circles) and the best fitted CASCADE calculations (continuous lines) for different folds ( $F$ ) at incident energies of 28, 35, 42 and 50 MeV.

## 4.8 Extraction of GDR parameters

In order to extract the GDR parameters ( $E_{GDR}$ ,  $\Gamma_{GDR}$ ,  $S_{GDR}$ ), the high energy  $\gamma$ -ray spectra were finally compared with the modified version of the statistical model code CASCADE along with the non-statistical bremsstrahlung compo-

ment. The high energy  $\gamma$ -ray spectra along with the CASCADE calculation is shown in Fig 4.13. The bremsstrahlung emission was parametrized by the exponential function ( $e^{-E_\gamma/E_0}$ ).  $E_0$  parameter was adopted from the systematics  $E_0 = 1.1[(E_{Lab} - V_c)/A_p]^{0.72}$  [Nif90], where  $E_{Lab}$ ,  $V_c$  and  $A_p$  are the beam energy, Coulomb barrier and the projectile mass, respectively. The systematic was verified earlier for alpha beams at similar energies by measuring the angular distribution of  $\gamma$ -rays arising from the non-statistical component [Sup12a]. The CASCADE calculation as well as the bremsstrahlung component were folded with the detector response function. The response function of the LAMBDA spectrometer was generated using GEANT4 simulation. The CASCADE calculation as well as the bremsstrahlung component are shown in Fig. 4.12 along with the experimental data at 28, 35, 42 and 50 MeV incident energies.

In the statistical model calculation, as  $^{97}\text{Tc}$  is nearly spherical nucleus, a single Lorentzian GDR strength function was assumed, having centroid energy ( $E_{GDR}$ ) and width ( $\Gamma_{GDR}$ ) as parameters. The other parameters (radius  $r_0$ , inverse level density parameter  $k$ , deformation parameters  $\delta_1$ ,  $\delta_2$  etc) were kept fixed as used for describing the neutron evaporation spectra. The moment of inertia of the CN was taken as  $\mathcal{I} = \mathcal{I}_0(1 + \delta_1 J^2 + \delta_2 J^4)$ , where  $\mathcal{I}_0$  is the moment of inertia of the spherical nucleus. The parameters  $r_0$ ,  $\delta_1$  and  $\delta_2$  were kept at their default values of 1.2 fm,  $0.9 \times 10^{-5}$  and  $2.0 \times 10^{-8}$ , respectively. The level density prescription of Ignatyuk [Ign75] was taken with the asymptotic level density parameters as extracted from the corresponding neutron evaporation spectra. The extracted spin distributions deduced from the experimental fold distributions were used as an inputs for different folds for both neutron and high energy  $\gamma$ -ray analyses. The GDR widths were obtained from the best fit statistical model calculations using a  $\chi^2$  minimization technique (in the energy range of 10–20 MeV of the high energy  $\gamma$ -ray spectra). In order to

Table 4.1: Average temperatures and average angular momenta along with level density parameters, GDR widths, centroid energies and bremsstrahlung parameters at different beam energies.

$E_{lab}$ MeV	$E^*$ MeV	$\bar{J}$ $\hbar$	$\bar{T}$ MeV	$\bar{a}$ MeV $^{-1}$	GDR Width MeV	$E_{GDR}$ MeV	$E_0$ MeV
28	29.3	13±6	0.80 $^{+0.07}_{-0.10}$	A/(8.0±0.4)	5.5±0.5	15.2±0.1	2.4
35	36.0	13±4	1.12 $^{+0.07}_{-0.09}$	A/(9.7±0.5)	6.0±0.5	15.5±0.1	3.4
		15±5	1.03 $^{+0.08}_{-0.10}$	A/(9.5±0.3)	5.7±0.6	15.5±0.1	3.4
		18±5	0.97 $^{+0.10}_{-0.15}$	A/(8.2±0.4)	5.6±0.6	15.4±0.1	3.4
42	43.0	14±5	1.32 $^{+0.07}_{-0.10}$	A/(9.0±0.4)	6.5±0.5	15.3±0.1	4.2
		16±5	1.23 $^{+0.07}_{-0.10}$	A/(8.1±0.4)	6.1±0.4	15.3±0.1	4.2
		19±6	1.16 $^{+0.11}_{-0.15}$	A/(7.8±0.5)	5.9±0.5	15.3±0.1	4.2
50	50.4	14±5	1.51 $^{+0.09}_{-0.09}$	A/(9.2±0.5)	7.5±0.6	16.4±0.1	4.8
		16±5	1.41 $^{+0.07}_{-0.10}$	A/(8.5±0.4)	6.9±0.5	16.6±0.1	4.8
		20±5	1.29 $^{+0.09}_{-0.12}$	A/(8.2±0.4)	6.2±0.5	16.3±0.1	4.8

highlight the GDR region, the linearized GDR plots were obtained using the quantity  $F(E_\gamma)Y^{exp}(E_\gamma)/Y^{cal}(E_\gamma)$ , where  $Y^{exp}(E_\gamma)$  and  $Y^{cal}(E_\gamma)$  are the experimental and best fitted CASCADE spectra, respectively, corresponding to the single Lorentzian function  $F(E_\gamma)$ . The linearized GDR plots for different energy and different folds are shown in Fig 4.17. The extracted GDR parameters,  $\bar{T}$  and  $\bar{J}$  are given in Table 4.1. The error estimation of temperature includes the uncertainty in the level density parameter, the effect of varying GDR centroid energy and the width of the selected angular momentum distribution. It needs to be mentioned that nuclear deformation was not included in the statistical calculation. Hence, the extraction of the apparent GDR widths have been reported and compared them with the different theoretical models, which also provide the apparent width of the GDR.

In the present work, ten new data points have been obtained in the low temperature range 0.8 – 1.5 MeV for  $^{97}\text{Tc}$ . This is the first systematic experimental measurement of angular momentum gated GDR width in the unexplored

temperature region ( $T < 1.5$  MeV) for  $^{97}\text{Tc}$ . To understand the exact nature of damping mechanism of the collective oscillation inside the nuclear matter, the new experimental data points have been compared with different theoretical calculations (macroscopic TSFM, CTFM and microscopic PDM calculation) and are discussed in the next Chapter.



# Chapter 5

## Results and discussion

The interpretation of the experimental results for the system  ${}^4\text{He} + {}^{93}\text{Nb}$  at  $E_{lab} = 28, 35, 42$  and  $50$  MeV has been discussed in this chapter. In this thesis work, ten new data points of GDR width have been obtained at very low temperatures ( $0.8 - 1.5$  MeV) for  ${}^{97}\text{Tc}$  [Dey14]. This is the first systematic experimental measurement of angular momentum gated GDR width in the unexplored temperature region ( $T < 1.5$  MeV) for  ${}^{97}\text{Tc}$ .

### 5.1 Evolution of GDR width at low temperature

A number of theoretical approaches have been proposed to demonstrate the behavior of GDR width as a function of temperature and angular momentum. Those are the macroscopic Thermal Shape Fluctuation Model (TSFM) [Alh88], microscopic Phonon Damping Model (PDM) [Dan98], Kusnezov parametrization on TSFM (pTSFM) [Kus98] etc. Very recently, a new parametrization on TSFM by including GDR induced intrinsic shape fluctuation has also been proposed and named as Critical Temperature Fluctuation Model (CTFM) [Dee12a]. The experimentally measured GDR widths in this work have been compared with all of the above theoretical models to investigate the damping mechanism of the giant dipole collective oscillations inside the nucleus. It should be mentioned that, in the present study, the angular momentum of the compound

nucleus was kept below the critical angular momentum ( $J_c=0.6A^{5/6}$ ) to see only the effect of temperature on the GDR width.

### 5.1.1 GDR width as a function of temperature with macroscopic TSFM calculation

According to TSFM calculation [Alh88], the GDR strength function is calculated by averaging the line shapes corresponding to the different possible nuclear shapes as discussed in section 2.3.1. The averaging over the distribution of nuclear shapes is weighted with a Boltzmann factor  $e^{-F(\beta,\gamma)/T}$ , where  $F(\beta,\gamma)$  is the free energy and  $T$  is the nuclear temperature. The calculations were performed

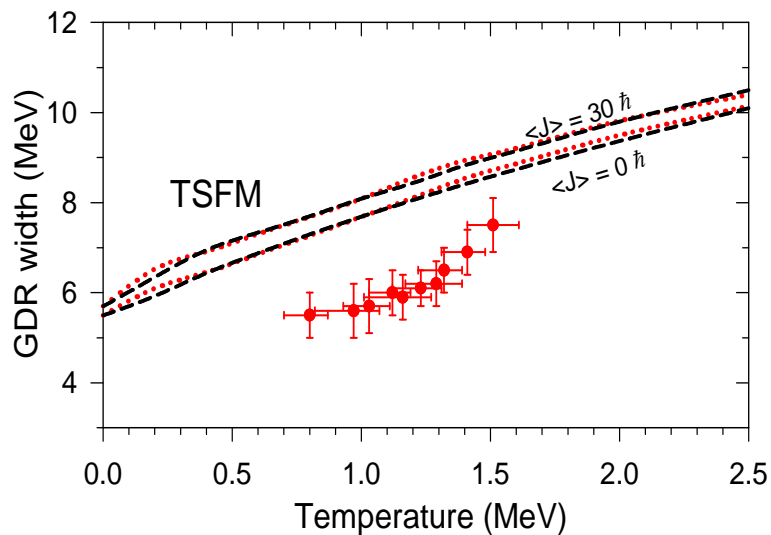


Figure 5.1: *Experimental GDR width (symbols) as a function of temperature along with the TSFM calculation. Dashed line without shell effect and dotted line with shell effect.*

with (dotted) and without (dashed) considering the shell effect (Fig 5.1). The details of this calculation has been discussed in the Chapter 2 (section 2.3.1). The TSFM calculations also showed that the effect of angular momentum on the GDR width below  $30 \hbar$  is small and essentially remains unchanged below  $20 \hbar$ . The compound nuclear particle evaporation widths ( $\Gamma_{ev}$ ) have been in-

incorporated in the TSFM calculation to take into consideration the effect of evaporation of particles and the corresponding energy loss before the GDR  $\gamma$ -emission in the CN decay chain. In this low temperature region, the particle decay width is rather small ( $\sim 0.2$  MeV at  $T = 2$  MeV) and its inclusion within the TSFM hardly improves the prediction. The predictions of TSFM at  $J = 0$  and  $J = 30 \hbar$  are shown in Fig 5.1 and compared with the experimental data.

### 5.1.2 GDR width as a function of temperature with new CTFM calculation

The CTFM [Dee12a] emphasize on an essential point that the intrinsic GDR vibration itself produces a quadrupole moment causing the nuclear shape to fluctuate even at  $T = 0$  MeV. Therefore, when the giant dipole vibration with its own intrinsic fluctuations in shape is used as a probe to view the thermal shape fluctuations, it is unlikely to probe the thermal fluctuations that are smaller than its own intrinsic fluctuation. Thus, the competition of  $\beta_{GDR}$  (the average

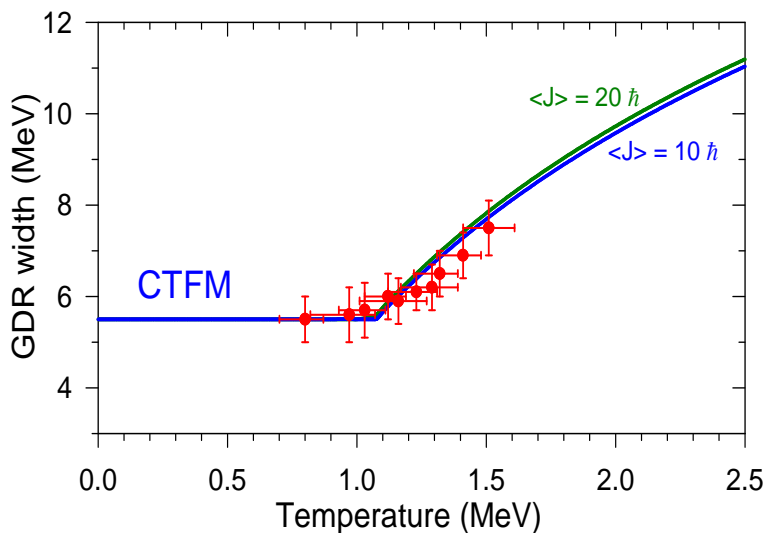


Figure 5.2: Experimental GDR width (symbols) as a function of temperature along with the CTFM calculation (continuous line).

deformation due to intrinsic fluctuation) and  $\Delta\beta$  (variance in deformation due

to thermal shape fluctuation) should give rise to a critical temperature ( $T_c$ ) and the experimental GDR width should remain constant at the ground state value below  $T_c$ . The detailed calculation of this new model has been discussed in Chapter 2 (section 2.3.2).

In order to compare the experimental data with CTFM, the ground state GDR width for  $^{97}\text{Tc}$  was calculated using the ground state deformation ( $\beta = 0.134$ ) and spreading width parametrization  $\Gamma_s = 0.05E_{GDR}^{1.6}$  [Jun08] for each Lorentzian. The ground state value was estimated to be 5.5 MeV which is consistent with the experimentally measured value in this mass region. The behavior of the GDR width within the CTFM was calculated as a function of  $T$  for  $J = 10$  and  $20 \hbar$  corresponding the extreme angular momenta involved in the measurement. The  $\Gamma_{ev}$  was not included in the CTFM calculations as the model was put forward by fitting the experimental data. The prediction of CTFM at  $J=10 \hbar$  and  $J=20 \hbar$  along with the experimental data are shown in the Fig 5.2.

### 5.1.3 GDR width as a function of temperature with microscopic PDM calculation

The experimental data were also compared with the results of microscopic PDM calculations [Dan98, Dan12a, Dan12b]. The PDM calculates the GDR width and the strength function directly in the laboratory frame without any need for an explicit inclusion of thermal fluctuation of nuclear shapes. Within the PDM, the GDR damping mechanism is caused by coupling of the GDR to non collective particle-hole (ph) and particle-particle (pp) [hole-hole (hh)] configurations. The coupling to various ph configurations leads to the quantal width (exists even at  $T = 0$ ), whereas the thermal width arises owing to the coupling to pp and hh configurations which appear at  $T > 0$  because of the distortion of the

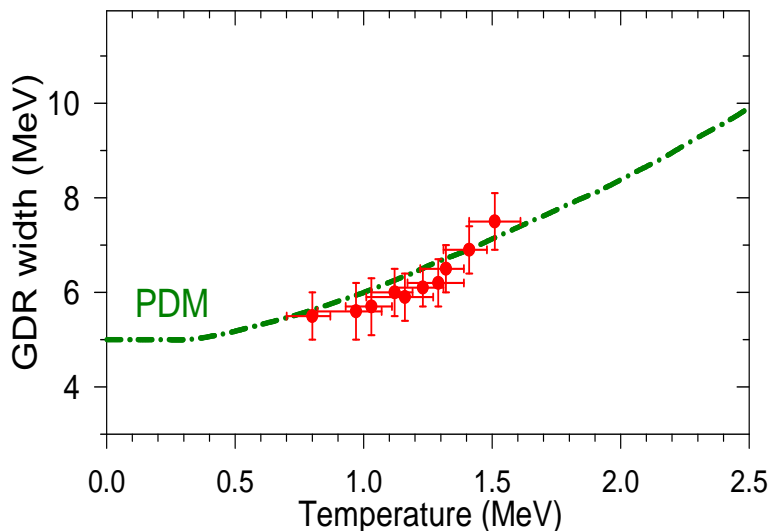


Figure 5.3: *Experimental GDR width (symbols) as a function of temperature along with the microscopic PDM calculation (dot-dashed line).*

Fermi surface. The model emphasizes the inclusion of thermal pairing, since, in finite systems such as in atomic nuclei, thermal pairing does not collapse at the critical temperature  $T_{cp} = 0.57\Delta(T = 0)$  of the superfluid-normal phase transition in infinite systems, but decreases monotonically as  $T$  increases. The prediction of the PDM at  $J = 0 \hbar$  along with the experimental data is shown in Fig. 5.3. The calculations were performed at  $J = 0 \hbar$  by using the single-particle energies obtained within the deformed Woods-Saxon potential with the deformation parameter  $\beta = 0.134$ , and including exact canonical-ensemble thermal pairing gaps for neutrons and protons [Dan12b].

## 5.2 Determination of nuclear deformation via GDR width at finite temperature for $^{97}\text{Tc}$

The average deformation ( $\langle\beta\rangle$ ) for this case was also extracted using the universal correlation between the experimental GDR width and the average deformation of the nucleus at finite  $T$ , and was compared with the TSFM [Dey14].

The correlation has been proposed recently by including the deformation induced by the GDR motion [Dee13]. As can be observed from Fig 5.4, the empirical deformations extracted from the experimental data match very well

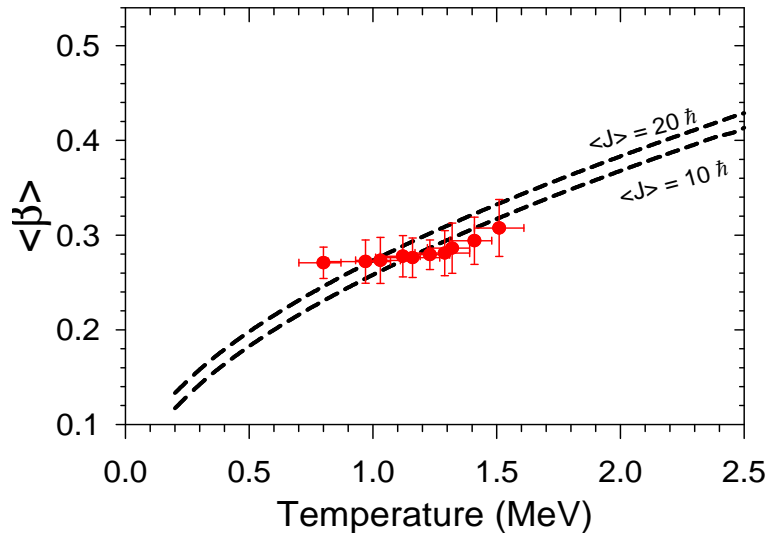


Figure 5.4: The average deformation measured from GDR width for  $^{97}\text{Tc}$  nucleus as a function of temperature with TSFM calculation (dashed line).

with the TSFM calculation above  $T_c$ . The good description of the CTFM as well as the validity of the universal correlation indicate that GDR induced deformations could play a decisive role in suppressing the GDR width at low  $T$ .

### 5.3 Discussion on the experimental results

The experimentally measured GDR widths in the present study for  $^{97}\text{Tc}$  along with the different theoretical calculations are shown in Fig 5.5. The filled circles represent the experimental data measured in this work, the dotted line represents the TSFM calculation with shell effect whereas the dashed line without shell effect, the continuous line represents the CTFM calculation and dashed-dotted line represents the microscopic PDM calculation. The experimental data show that the GDR width remains constant up to a certain temperature and

increases thereafter. As can be seen, the adiabatic TSFM differs significantly from the experimental data in the entire region ( $T < 1.5$  MeV). It was earlier conjectured that the microscopic shell effect may be the responsible for this suppression at low temperature. But, even after incorporating the shell correction, the situation does not improve (as shown in Fig 5.5) [Dee12a]. As expected for  $^{97}\text{Tc}$ , the effect of shell correction on the GDR width is quite small and leads to similar results as obtained considering the liquid drop model (as shown in Fig 5.1). This interesting result clearly suggests that the suppression of the GDR width at these low  $T$  is a general feature for all nuclei and cannot be explained including only the shell effects.

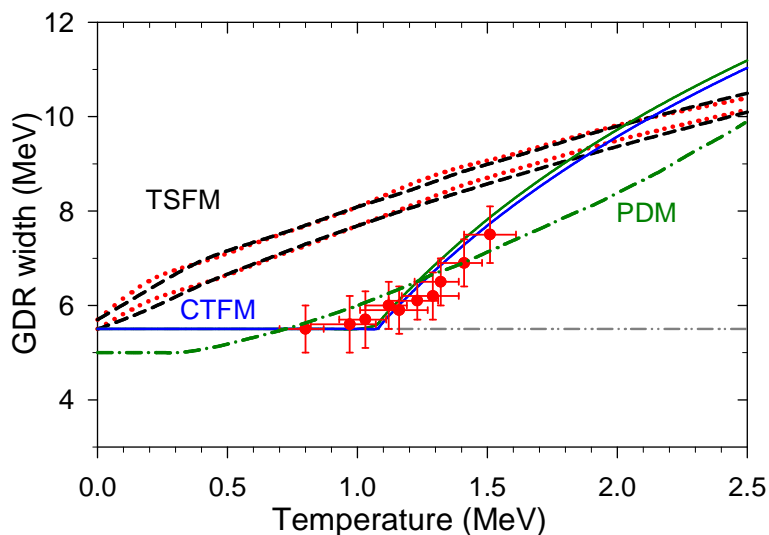


Figure 5.5: Experimentally measured GDR width (symbols) as a function of temperature with different theoretical predictions. The dotted line represents the TSFM calculation with shell effect whereas dashed line without shell effect, the continuous line represents CTFM calculation and dashed-dotted line represents the microscopic PDM calculation for  $^{97}\text{Tc}$ .

On the other hand, the microscopic PDM model better explains the trend of the experimental data at the low temperature region ( $T < 1.5$  MeV). It has been shown that the thermal pairing effect plays an important role in the evolution of GDR width at this low temperature. However, in the PDM calculation, the

deformed ground state GDR width was taken as 5.0 MeV which is close to the ground state value (5.5 MeV). Moreover, the PDM calculation does not have any angular momentum dependence explicitly.

Interestingly, the CTFM represents the data remarkably well. This excellent match between experimental data and CTFM clearly suggests that the experimental GDR widths are not suppressed, rather TSFM over predicts the GDR width at low temperature as it does not take into account the intrinsic GDR fluctuation induced by GDR vibrations. Moreover, the systematic trend of the data also shows that the critical temperature for the increase of GDR width lies between 1 and 1.2 MeV as predicted by the CTFM ( $T_c = 0.7 + 37.5/A$ ). The average deformation of this nucleus was also calculated by considering the GDR induced intrinsic fluctuation and it is well explained by the TSFM calculation.

It is intriguing to find that the microscopic PDM and macroscopic phenomenological CTFM gives the nearly same results though the origin of these two models are different, where as, the TSFM completely fails to explain the experimental data at low temperatures. These interesting results indicate that the effect of GDR induced deformation could be one of the ways in explaining macroscopically the behavior of GDR width at low T. However, this effect is not explicitly needed in microscopic PDM, rather thermal pairing should be included to have adequate description of the damping of GDR width in open shell nuclei at low T. It would also be interesting to compare the data with TSFM by including the effect of thermal pairing, but is beyond the scope of this present work. Nevertheless, the present experimental study does provide a stringent testing ground of the theoretical models as a function of T. It provides a completely new set of data for the variation of GDR widths for  $^{97}\text{Tc}$  nuclei at low temperatures (0.8 – 1.5 MeV).

# Chapter 6

## Neutron response of LAMBDA spectrometer

### 6.1 Introduction

The LAMBDA spectrometer (consisting of 162 large BaF<sub>2</sub> crystals) has been developed for the measurement of high-energy  $\gamma$ -rays [Sup07], and is discussed in details in Chapter 3. Neutrons are the major source of backgrounds in the high energy  $\gamma$ -ray experiments. Until now, the LAMBDA spectrometer has been employed efficiently to reject the neutron backgrounds from the high-energy  $\gamma$ -ray spectrum by the time-of-flight (TOF) technique [Sup07, Dee12a, Sup12a, Dee10b]. However, instead of rejecting the neutrons, the neutron TOF spectra as recorded by the LAMBDA spectrometer can be utilized to extract the nuclear level density (NLD) parameter which is an important ingredient for the statistical model calculation as well as for a proper estimation of nuclear temperature. The most widely used detectors for neutron measurement are liquid hydrocarbon based scintillators such as NE213 [Nak01], BC501A [Ban07], BC521, BC525 [Ban09], etc. because of their good timing, pulse shape discrimination (PSD) properties and efficient energy transfer in the hydrogenous material. However, a BaF<sub>2</sub> scintillator can also be efficiently employed for neutron detection because of its excellent timing property (a fast decay component of 0.6 ns) and high density (4.88 g/cc). In this chapter, the LAMBDA spectrometer has been tested

for neutron spectroscopy and discussed whether it can be used as a neutron detector or not.

Neutrons having energies  $E < 10$  MeV predominantly interact via  $(n, \gamma)$  and  $(n, n'\gamma)$  reactions with the  $\text{BaF}_2$  material, whereas for  $E > 10$  MeV, the interaction occurs via different complicated reactions producing charged hadrons [Lan97]. The use of a neutron detector usually requires the knowledge of its intrinsic neutron detection efficiency which depends upon many factors, such as, neutron energy, electronic threshold, dimensions of the crystal, interaction mechanism, etc. [Ban09]. Earlier, many authors have investigated the neutron response of the  $\text{BaF}_2$  scintillators of various dimensions and over several energy ranges. The efficiency for neutron energies up to 22 MeV was measured by Matulewicz et al. [Mat89], while Kubota et al. [Kub89] measured the efficiency between 15 MeV and 45 MeV by introducing a PSD cut on the neutron events. The response to fast neutrons in the energy ranges 15–150 MeV and 45–198 MeV was studied by R. A. Kryger et al. [Kry94] and Gunzert-Marx et al. [Gun05], respectively. The investigation was extended to relativistic neutrons with energies up to 1300 MeV by V. Wagner et al. [Wag97]. For neutrons in the energy range of 0.5 to 10 MeV, C. Bourgeois et al. [Bou85] and Lanzano et al. [Lan97] measured the efficiency of 14 cm and 5 cm thick  $\text{BaF}_2$  crystals, respectively.

In this work, the neutron response of the existing LAMBDA spectrometer has been presented and compared with that of a standard liquid scintillator based neutron detector (BC501A). It has been shown that the neutron energy spectrum measured by the LAMBDA spectrometer in an in-beam experiment can be efficiently used to extract the NLD parameter. The average interaction length of neutrons in the  $\text{BaF}_2$  scintillator have also been measured, for the first time, to precisely determine the neutron TOF energy resolution which

was uncertain in other measurements. Finally, a detailed GEANT4 simulation has been carried out to understand and to explain the neutron response of the LAMBDA spectrometer.

## 6.2 Experimental Details

### 6.2.1 Efficiency measurement

The intrinsic neutron detection efficiency of the LAMBDA spectrometer has been measured using a  $^{252}\text{Cf}$  spontaneous fission source (62  $\mu\text{Ci}$ ).  $^{252}\text{Cf}$  decays via  $\alpha$  particle emission (96.91%) and spontaneous fission (3.09%) with a half-life of 2.65 years and the energy spectrum of the emitted neutrons is well documented [Knol]. Generally, the fission events are measured using fragment detectors such as surface-barrier detectors [Tho87], PPAC and MWPC [Bre02]. Since a large number of  $\gamma$ -rays are also emitted from the excited fission fragments, a fast-timing  $\gamma$ -ray detector (e.g.  $\text{BaF}_2$ ) can also be effectively used to select the fission events [Dee10c] as well as to obtain the start trigger for neutron TOF measurement.

Four large  $\text{BaF}_2$  detectors (each having dimension of  $3.5 \times 3.5 \times 35$   $\text{cm}^3$ , a small part of the LAMBDA spectrometer), arranged in  $2 \times 2$  matrix, were kept at a distance of 80 cm from the  $^{252}\text{Cf}$  source to study the neutron response. The detectors were gain matched and equal thresholds were applied to all of them. A BC501A-based neutron detector (5 inch in diameter and 5 inch in length) [Ban07] of known efficiency was also employed to measure the neutron energies, in order to compare its efficiency with that of the  $\text{BaF}_2$  detectors. The neutron detector was kept on the other side of the source at a distance of 150 cm to equalize the solid angle of the two detector systems. Along with these detectors, a 50 element  $\text{BaF}_2$   $\gamma$ -multiplicity filter [Dee10a] was also used to detect the low energy discrete  $\gamma$ -rays emitted from the decay of excited fission fragments

to establish a correlation between the neutrons and the fission process. The multiplicity filter was split into two blocks of 25 detectors each, in staggered castle type geometry, and placed at a distance of 3 cm above and below the sealed  $^{252}\text{Cf}$  source. A level-1 trigger (A) was generated from the multiplicity filter array when at least one detector from both top and bottom blocks fired in coincidence above a threshold of 250 keV. Another trigger (B) was generated when the signal in any of the detector elements of the LAMBDA spectrometer or BC501A neutron detector crossed a threshold of 350 keV. A coincidence of these two triggers (A and B) generated the master trigger ensuring the selection of fission events and rejection of backgrounds. The schematic view of the experimental set-up is shown in Fig. 6.1. The TOF technique was employed

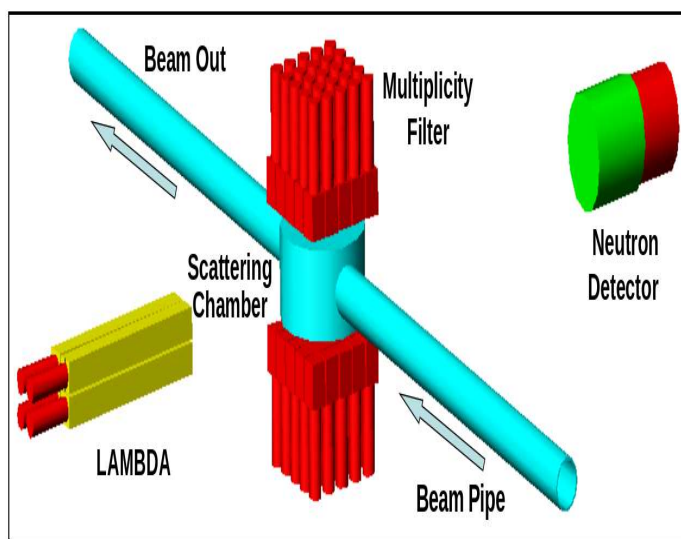


Figure 6.1: Schematic view of the experimental set-up for neutron studies using LAMBDA array.

for neutron energy measurement in both the detector systems using the start signal from the multiplicity filter. Along with the time spectrum, the pulse height spectrum of each detector was also measured to apply energy thresholds in off-line analysis. A typical TOF spectrum for one of the  $\text{BaF}_2$  detectors (in the array) at a threshold of 350 keV is shown in Fig. 6.2a. The TOF spectrum

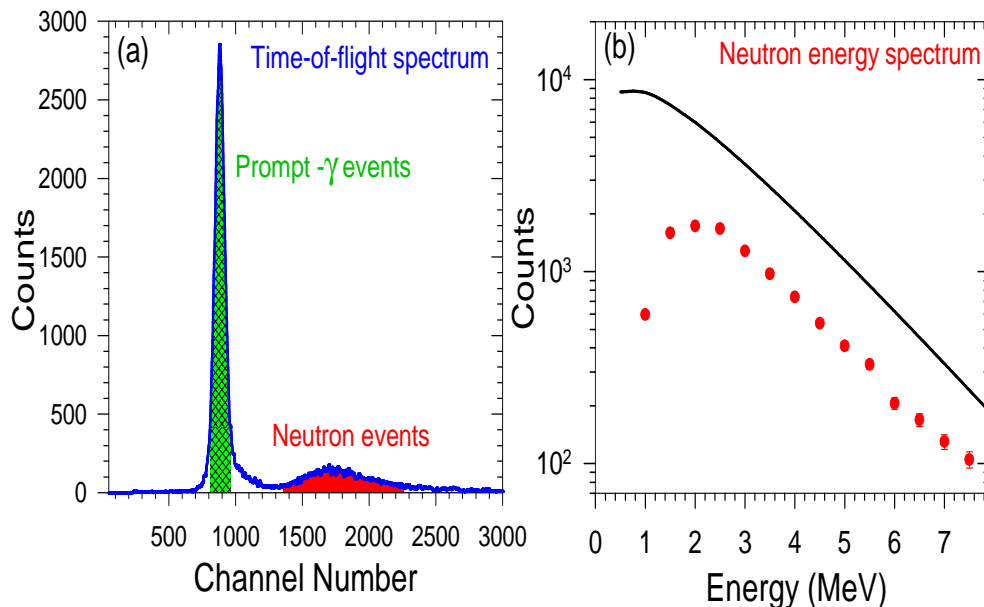


Figure 6.2: [a] TOF spectrum for one of the  $\text{BaF}_2$  detectors in the array. [b] Neutron energy spectrum of the  $\text{BaF}_2$  array (filled circle) compared with the expected neutron energy spectrum from  $^{252}\text{Cf}$  (continuous line) [Knol].

was converted to energy spectrum using the prompt  $\gamma$  peak as a time reference. The neutron energy spectrum measured with the  $\text{BaF}_2$  array (summing all four detectors) is shown in Fig. 6.2b (filled circles). The efficiencies of both the detector systems were determined by dividing the neutron yield per fission by the expected neutron energy distribution (continuous line in Fig. 6.2b) of  $^{252}\text{Cf}$  [Ban07, Ban09, Knol] (with temperature  $T = 1.42$  MeV), properly normalized with the detector solid angle and the total number of fission events detected. The total number of fission events per second was also measured experimentally using the approach [Lan97] discussed below.

A  $^{252}\text{Cf}$  source was placed very close in front of one of the multiplicity filter (M1) block (arranged in  $5 \times 5$  matrix, discussed later). The other multiplicity filter (M2) block was placed at a distance ( $d$ ) on the other side of the source. The number of coincidence between M1 and M2 was measured for different

distances of M2 from the source. For larger distances, a  $1/d^2$  variation of the coincidence rate was observed. For smaller distances, the rate saturated to a value which was consistent with the number of fission events expected from the source activity. The experiment was repeated without the source to reject the background events (e.g. cosmic rays,  $\alpha$  impurity in the  $\text{BaF}_2$  crystal, etc). The number of fission per second measured experimentally was used for the efficiency calculation. It needs to be mentioned that the measurement contains a very small systematic error ( $< 1\%$ ) due to the presence of isotopic impurity in the source.

The efficiencies of individual detectors in the array were also determined. It was found that the intrinsic efficiencies of individual detector elements were identical and very similar to that observed for the array. The energy dependent efficiencies of the  $\text{BaF}_2$  array and BC501A detector are shown in Fig. 6.3. It is interesting to note that, starting at 4 MeV, the neutron detection efficiency of the BC501A detector decreases monotonically as a function of neutron energy, whereas, the efficiency of the  $\text{BaF}_2$  array increases sharply up to 2–3 MeV and reaches a plateau at efficiency  $\sim 34\%$  which is comparable with that of the neutron detector at these energies. However, the BC501A has an extra advantage in discriminating the neutrons from the  $\gamma$ -rays using PSD technique.

The experimentally measured efficiencies were also compared with the corresponding GEANT4 [Ago03] simulation. The GEANT4 simulation for the neutron detector (BC501A) has already been discussed in detail in Ref [Ban07, Ban09]. In the case of the  $\text{BaF}_2$  detector, a simulation was performed using a series of GEANT4 classes like detector construction and material building, particle and physics process definition, particle tracking, event action, etc. Individual neutrons were randomly generated by a particle generator (G4ParticleGun) according to neutron energy spectrum in  $^{252}\text{Cf}$  source and tracked through the

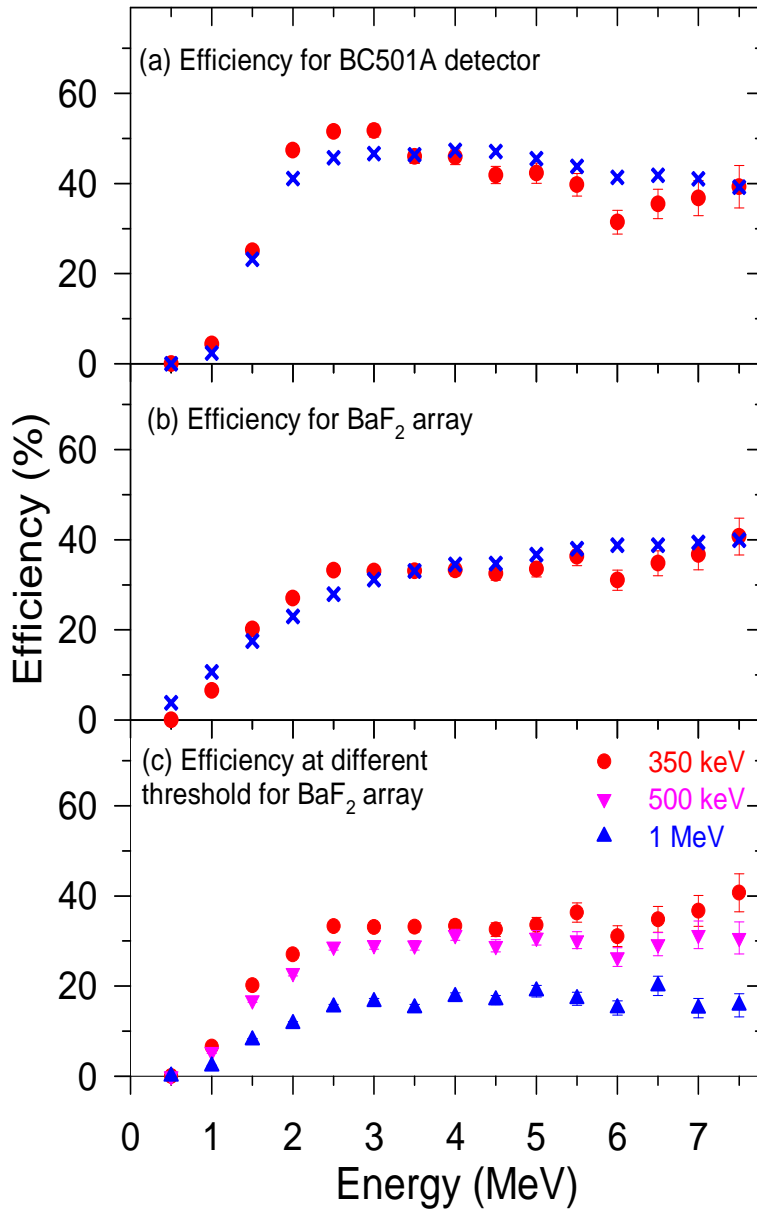


Figure 6.3: [a] Energy dependent neutron detection efficiency of BC501A detector. [b] Energy dependent neutron detection efficiency of BaF<sub>2</sub> array. Filled circles are the experimental data points and cross symbols represent GEANT4 simulation. [c] Neutron detection efficiency at different energy thresholds.

detector volume. The energy deposition was recorded step-by-step and finally added for each event. Since neutrons of energies  $E < 10$  MeV interact with the BaF<sub>2</sub> material predominantly by  $(n, \gamma)$  or  $(n, n'\gamma)$  [Lan97] and deposit their energy in the detector as photons, we considered only the processes of neutron

inelastic scattering and capture using G4LENeutronInelastic and G4LCCapture models, respectively, in the physics list class (G4PhysicsList). We did not include the more complicated nuclear reaction mechanisms and the response of the photo multiplier tube. In the simulation, all the electromagnetic processes were considered for  $\gamma$ -ray interaction. It was found that the experimentally measured efficiencies of the BaF<sub>2</sub> array and BC501A detector were in good agreement with the corresponding GEANT4 simulations. The energy dependent efficiencies of the BaF<sub>2</sub> array at various energy thresholds are displayed in Fig. 6.3c. As can be seen from Fig 6.3, the overall efficiency for BaF<sub>2</sub> detectors decreases with increasing energy threshold, while the nature of the spectrum remains the same. The cross-talk probability of neutrons in the BaF<sub>2</sub> array was also estimated in off-line analysis and found to be  $\sim 12\%$  at a threshold of 350 keV. It should be mentioned that only statistical errors are shown in Fig 6.3. The systematic errors are  $< 1\%$  and arise predominantly due to isotopic impurity present in the source.

### 6.2.2 Time-of-flight energy resolution

The TOF energy resolution of neutrons is given by the relation,

$$\left(\frac{\delta E}{E}\right)^2 = \left(2\frac{\delta T}{T}\right)^2 + \left(2\frac{\delta L}{L}\right)^2 \quad (6.1)$$

where  $\delta E$  is the energy resolution,  $\delta T$  is the time resolution of the detector,  $L$  represents the flight length of the neutron and  $\delta L$  is the flight path spread due to the detector size. As the density of the BaF<sub>2</sub> material is high, it is expected that, the neutrons will interact mostly in the initial part of the detector volume. Hence, the total size of the detector should not be taken as the uncertainty in length, rather the average interaction length should be estimated and used for energy resolution calculations. The average interaction length of neutrons in the BaF<sub>2</sub> detector was measured using the detector elements of  $\gamma$ -multiplicity filter.

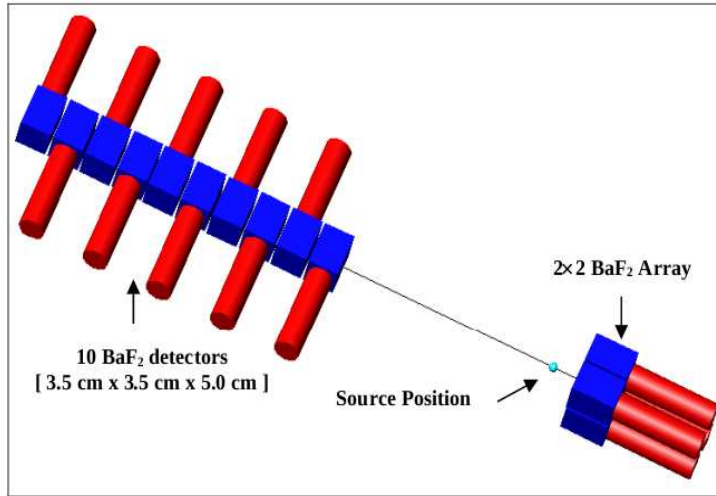


Figure 6.4: *Experimental set-up for the measurement of average interaction length of neutrons in BaF<sub>2</sub> crystal.*

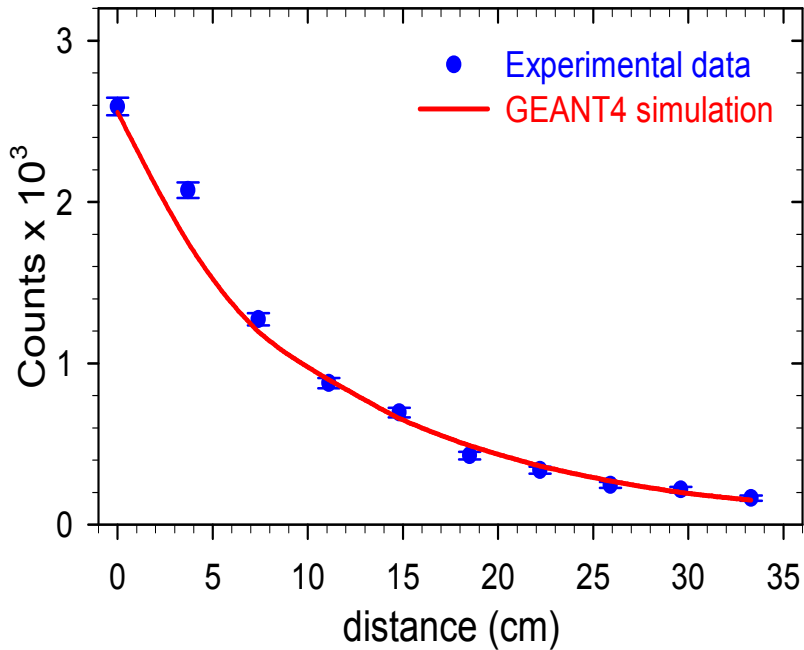


Figure 6.5: *Variation of the number of events as a function of distance corresponding to the number of detectors. Filled circles are the experimental data points and continuous line represents GEANT4 simulation*

The length of each detector was 5 cm and its cross-sectional area was same as that of the LAMBDA array elements ( $3.5 \times 3.5 \text{ cm}^2$ ). Ten such detectors were arranged linearly (as shown in Fig. 6.4) one after another so that the

effective length that may be traversed by the neutrons is identical to that of the bigger (35 cm) elements of the LAMBDA array. Next, the detectors were gain matched and equal thresholds were applied to all (300 keV). The TOF spectrum for each detector was measured using a  $^{241}\text{Am}-^9\text{Be}$  source which was kept at a distance of 50 cm from the first of the ten detectors kept in line. The start trigger for TOF measurement was taken from another set of identical  $\text{BaF}_2$  detectors which were arranged in a  $2 \times 2$  matrix and kept at a distance of 5 cm on the other side of the source. A schematic view of the experimental set-up to measure the average interaction length is shown in Fig. 6.4. In order

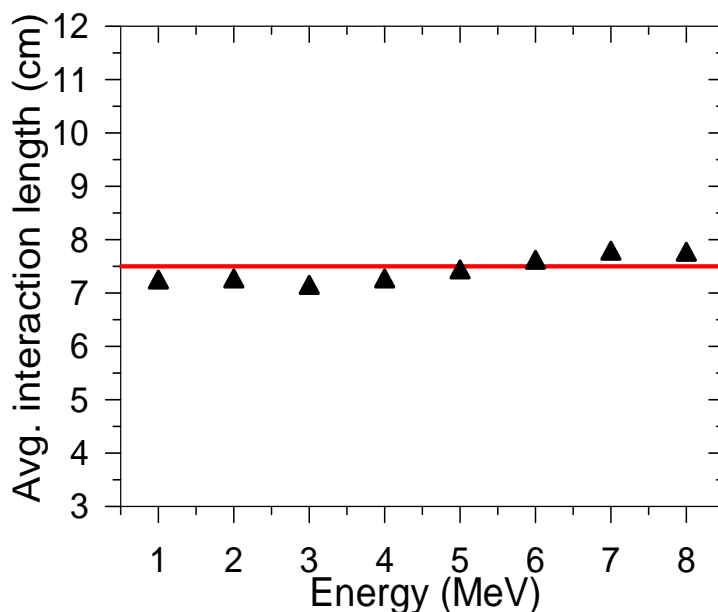


Figure 6.6: *Simulated average interaction length (symbols) of neutron in a 35 cm  $\text{BaF}_2$  crystal at different incident energies*

to estimate the average interaction length, the total number of counts in the neutron TOF spectrum was calculated corresponding to an energy range of 3 – 6 MeV in each of the 10 detectors. Since, a flat overall background was obtained in the TOF spectrum, the background counts were subtracted by selecting the

same channels (as for energy bins) from the left of the prompt  $\gamma$  peak. The total number of neutron events obtained in this energy range (3 – 6 MeV) is shown in Fig. 6.5 as a function of distance corresponding to the number of detectors. It is very interesting to note that the total number of counts is highest for the first detector and decreases for subsequent detectors, pointing towards the fact that the interaction of neutrons in the BaF<sub>2</sub> detector decreases exponentially with increase in distance. A complete GEANT4 simulation was also carried out for this experimental set-up to calculate the average interaction length. As could be seen from Fig. 6.5, the experimental data and the simulation results (continuous line in Fig. 6.5) match remarkably well with each other. This excellent match between the experimental data and the simulation provided us with the required confidence in GEANT4 simulation. The cross-talk probability was also measured for this set-up and was found to be less than 1%.

Next, a GEANT4 simulation has been performed to estimate the average interaction length for the LAMBDA detector set-up. The interaction point of neutrons in the BaF<sub>2</sub> material were found to decrease according to the relation  $\exp(-\mu x)$  where  $\mu = 0.13 \text{ cm}^{-1}$ . Using this distribution, the average interaction length of neutrons in the LAMBDA detector element was estimated using the relation

$$\langle x \rangle = \frac{\sum x \exp(-\mu x)}{\sum \exp(-\mu x)} \quad (6.2)$$

and found to be 7.6 cm when kept at a distance of 80 cm from the source. As a result, the energy resolution at 4 MeV using equation (1) was found to be +0.4 MeV, corresponding to  $\delta T = 0.96 \text{ ns}$  (intrinsic time resolution of the detector). It has also been shown that the average interaction length remains almost constant for different neutron energies (1 – 10 MeV) as shown in Fig 6.6.

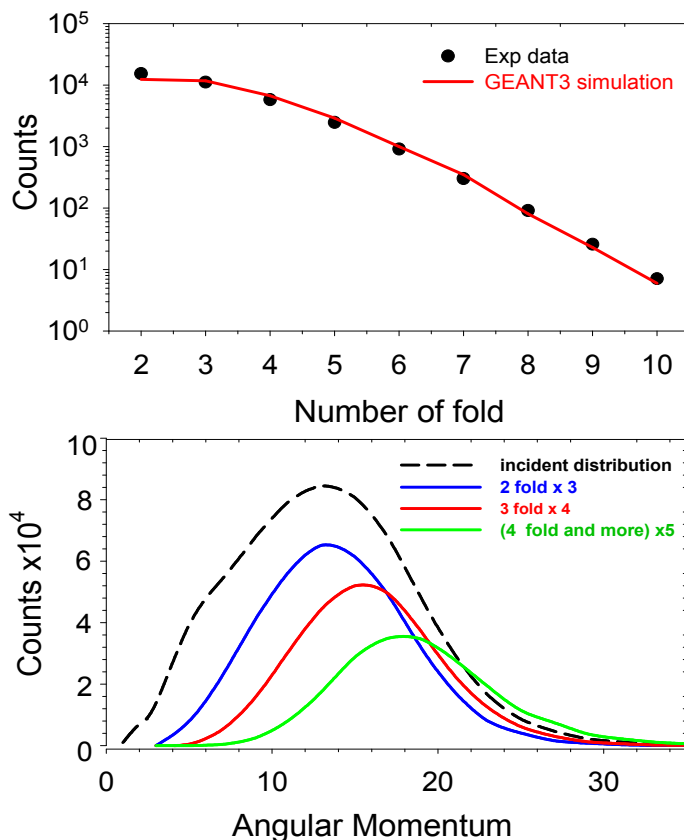


Figure 6.7: [Top panel] Measured fold distribution along with the GEANT3 simulation fit. [Bottom panel] Angular momentum distribution for different folds for the  ${}^4\text{He} + {}^{93}\text{Nb}$  system

### 6.3 In-beam-experiment: LAMBDA used as a neutron detector

The performance of the LAMBDA spectrometer as a neutron detector was tested by measuring the evaporated neutron energy spectrum in an in-beam experiment. The experiment was performed at the Variable Energy Cyclotron Centre, Kolkata using a 35 MeV alpha beam from the K-130 cyclotron. A self-supporting foil of  ${}^{93}\text{Nb}$  (99.9% pure) with a thickness of  $\sim 1 \text{ mg/cm}^2$  was used as the target. The compound nucleus  ${}^{97}\text{Tc}^*$  was populated at the initial excitation energy of 36 MeV. The experimental set-up was similar to that used for the efficiency measurement and is shown in Fig. 6.1. To keep the background of

the detectors at a minimum level, the beam dump was kept 3 m away from the target and was well shielded with the layers of lead and borated paraffin. Data from the BaF<sub>2</sub> and BC501A detectors were recorded in an event-by-event mode in coincidence with the  $\gamma$ -multiplicities in order to measure the neutron energy spectrum and to extract the angular momentum of the compound nucleus. The TOF technique was employed for neutron energy measurement in both the detectors using the start trigger from the  $\gamma$ -multiplicity filter. Along with the time spectrum, the pulse height spectrum of each detector was also measured to apply the energy thresholds in off-line analysis. The cross-talk probability of neutrons in the BaF<sub>2</sub> array was estimated in the above experiment and found to be same as that obtained in the efficiency measurement with <sup>252</sup>Cf.

The fold distribution was converted to the angular momentum distribution applying the approach discussed in Ref. [Dee10a]. The experimental fold distribution measured using the 50-element  $\gamma$ -multiplicity filter is shown in the top panel of Fig. 6.7. The angular momentum distributions corresponding to different folds are shown in the bottom panel of Fig. 6.7 while the average values are given in Table 6.1. The neutron energy spectra were extracted from the TOF spectra using the prompt  $\gamma$ -peak as a time reference. The neutron energy spectra measured using the BC501A and BaF<sub>2</sub> array are shown in Fig. 6.8 (open circles).

The asymptotic level density parameter  $\tilde{a}(A) = A/k$  is an important input for CASCADE calculation [Puh77], where  $k$  is kept free and generally adjusted to get the best fit with the experimental data. We extracted the values of  $k$  from the neutron energy spectra measured using the BC501A and BaF<sub>2</sub> array for different folds of the  $\gamma$ -multiplicity filter. The simulated angular momentum distribution corresponding to each fold was used as an input in the modified version of the statistical model code CASCADE. The value of  $k$  was extracted

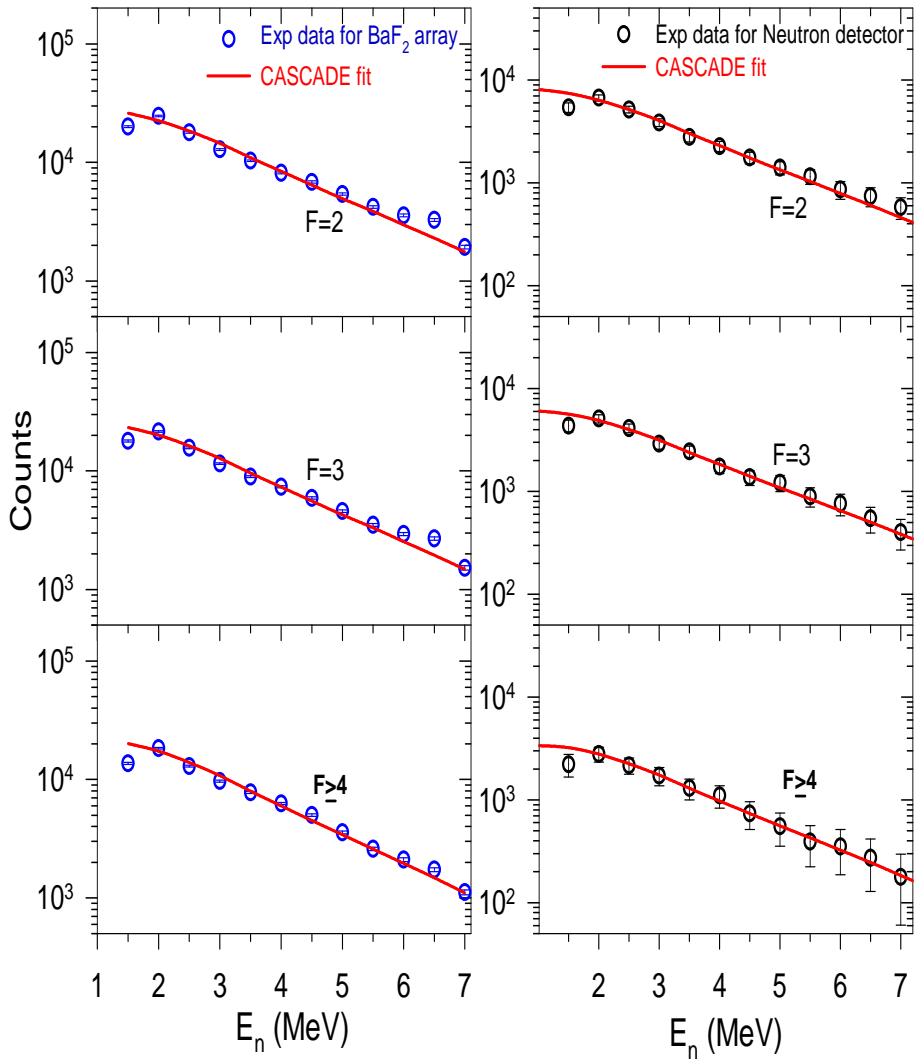


Figure 6.8: [a] Experimental neutron energy spectra (open circles) of BC501A detector along with the CASCADE fit (continuous line) for different folds. [b] Experimental neutron energy spectra (open circles) of BaF<sub>2</sub> detector along with the CASCADE fit (continuous line) for different folds.

from the experimental data by chi-square minimization technique in the energy range of 3–7 MeV. The experimental neutron energy spectra along with the CASCADE predictions for the BC501A and BaF<sub>2</sub> detector systems are shown in Fig. 6.8. The best fitted values of the inverse level density parameter ( $k$ ) for both the detector systems for different folds are compared in Table 6.1.

Table 6.1: *The values of  $k$  corresponding to different folds of BaF<sub>2</sub> and BC501A detectors.*

Fold	Angular momentum $\langle J \rangle \hbar$	$k$ (MeV) (BaF <sub>2</sub> array)	$k$ (MeV) (BC501A)
2	14	$10.8 \pm 0.4$	$10.4 \pm 0.2$
3	16	$10.5 \pm 0.4$	$10.3 \pm 0.4$
4 & more	19	$9.6 \pm 0.3$	$9.7 \pm 0.3$

## 6.4 Results and discussion

As seen in the previous section-6.2.1, the neutron detection efficiency of the BaF<sub>2</sub> array is comparable to that of the liquid organic scintillator. The efficiency of the BaF<sub>2</sub> array increases sharply up to 2–3 MeV and reaches a plateau at efficiency  $\sim 34\%$  which is comparable with that of the neutron detector at these energies. The TOF energy resolution at 4 MeV is around  $+ 0.4$  MeV, which is very good. Interestingly, it can also be seen from the Table 6.1 that the inverse level density parameters extracted from the BaF<sub>2</sub> and BC501A detectors in an in-beam experiment are in good agreement. It is also observed that the values of  $k$  decrease with the increase in angular momentum similar to the results obtained earlier for charged particle and neutron measurements [Pra12] from the same system. Thus, the excellent match between the level density parameter obtained from both the detector systems clearly suggests that the LAMBDA spectrometer can be effectively and efficiently used for the measurement of evaporated neutrons from an excited compound nucleus in an in-beam experiment with its intended use in the measurement of high energy  $\gamma$ -rays.



# Chapter 7

## Summary and Conclusion

The main motivation of the work presented in this thesis has been the study of giant dipole resonance (GDR) width at very low temperatures and to understand the exact nature of the damping mechanism of the collective vibration inside the nuclear medium. The evolution of the GDR width at low temperatures ( $T < 1.5$  MeV) is still unclear because the experimental data are in complete disagreement with the most popular macroscopic Thermal Shape Fluctuation Model (TSFM) in this temperature region. Moreover, a critical behavior (the GDR width remains same at the ground state value up to a critical temperature and increases thereafter) has been predicted recently in the evolution of the GDR width as a function of temperature. But, there are no such experimental measurements below the critical point and the subject strongly deserves further investigation.

In this work, a systematic measurement of GDR width in  $^{97}\text{Tc}$  nucleus has been performed at very low temperatures ( $T < 1.5$  MeV). This is the first measurement of the GDR width at finite temperature in  $^{97}\text{Tc}$  nucleus both above and below the critical point and can be effectively used to verify the existing theoretical models. The high energy  $\gamma$ -rays emitted from the decay of GDR have been measured in coincidence with the low energy discrete  $\gamma$ -rays in order to have the angular momentum gated GDR measurement. A part of LAMBDA has been used to measure the high energy  $\gamma$ -rays whereas

the low energy discrete  $\gamma$ -rays have been measured using a  $\gamma$ -multiplicity filter. The evaporated neutron energy spectra have also been measured simultaneously using a liquid organic scintillator (BC501A) based neutron detector to estimate the nuclear level density parameter and hence the temperature of the compound nucleus precisely. The GDR widths have been extracted by comparing the experimental high energy  $\gamma$ -ray spectra with the modified statistical model code (CASCADE) prediction.

The measured GDR widths have been compared with the different theoretical models such as macroscopic TSFM, phenomenological CTFM and microscopic PDM. It has been found that the macroscopic TSFM model completely fails to explain the experimental data at this low temperature region ( $T < 1.5$  MeV). This interesting result along with the previous measurements clearly suggest that the suppression of the GDR width at these low temperatures is a general feature for all nuclei. It has also been found that the extracted GDR widths indeed remains nearly constant till  $T \sim 1$  MeV and increases thereafter. On the other hand, the microscopic PDM describes the data quite well in the entire temperature range. It should be mentioned that in PDM calculation the ground state GDR width has been taken as 5.0 MeV (which is close to the deformed ground state GDR width 5.5 MeV) to match the experimental data. In order to compare the data with CTFM, the ground state GDR width was calculated using the ground state deformation of  $^{97}\text{Tc}$  ( $\beta = 0.134$ ) and spreading width parametrization  $\Gamma_s = 0.05E_{GDR}^{1.6}$  for the corresponding Lorentzian. The ground state value was estimated to be 5.5 MeV which is consistent with the experimentally measured value in this mass region. Interestingly, the CTFM represents the data remarkably well over the entire  $T$  region. This excellent match between the experimental data and the CTFM clearly suggests that the experimental GDR widths are not suppressed, rather TSFM over predicts the

GDR widths at low temperatures as it does not take into account the intrinsic shape fluctuations induced by the GDR vibrations. Moreover, the systematic trend of the data also shows that the critical temperature for the increase of GDR width is between 1 and 1.2 MeV as predicted by the CTFM ( $T_c = 0.7 + 37.5/A$ ). It is intriguing to find that, even though the formalisms of PDM and CTFM seem to be completely different in origin, the two models give very similar results. These interesting results indicate that the effect of GDR induced deformation could be one of the ways in explaining macroscopically the behavior of GDR width at low  $T$ . However, this effect is not explicitly needed in microscopic PDM, rather thermal pairing should be included to have adequate description of the damping of GDR width in open shell nuclei at low  $T$ . Nevertheless, the present experimental study does provide a stringent testing ground of the theoretical models for the evolution of GDR widths as a function of  $T$ .

The average deformations ( $\langle\beta\rangle$ ) were also extracted using the universal correlation between the experimental GDR width and the average deformation of the nucleus at finite  $T$ , and were compared with the TSFM. The correlation has been proposed recently by including the deformation induced by the GDR vibration in nuclei. The empirical deformations extracted from the experimental data match excellently well with the TSFM calculation above the critical temperature. The good description of the CTFM as well as the validity of the universal correlation indicates that GDR induced quadrupole moment could play a decisive role in suppressing the GDR width at low  $T$ .

Apart from the GDR studies, the thesis also deals with the neutron response of the LAMBDA spectrometer consisting of 162 BaF<sub>2</sub> crystals (each having dimension of  $3.5\times 3.5\times 35$  cm<sup>3</sup>) which was initially developed for the measurement of high-energy  $\gamma$ -rays from the decay of the GDR built on excited states. Until

now, the LAMBDA spectrometer has only been employed efficiently to reject the neutron contamination from the high-energy  $\gamma$ -ray spectrum by the time-of-flight (TOF) technique. However, instead of rejecting the neutrons, they can be utilized to extract the nuclear level density parameter which is an important ingredient for the statistical model calculation as well as for the precise measurement of compound nucleus temperature. In this thesis work, the neutron response of the LAMBDA spectrometer has also been studied and compared with a standardized liquid organic scintillator (BC501A) based neutron detector.

The energy dependent intrinsic efficiency of the LAMBDA spectrometer has been measured for neutron detection relative to a liquid organic scintillator based neutron detector (BC501A) of known efficiency and compared with a detailed GEANT4 simulation. The average interaction length of neutrons have also been calculated in each of the LAMBDA elements to estimate the time-of-flight energy resolution. Furthermore, the spectrometer has been tested in an in-beam experiment ( ${}^4\text{He} + {}^{93}\text{Nb}$  @  $E_{lab} = 35$  MeV) to measure the inverse nuclear level density parameter ( $k$ ) and compared with that measured using the standard BC501A neutron detector. Interestingly, it was observed that the values of  $k$  obtained from both the detector systems are very similar, indicating that the  $\text{BaF}_2$  detectors can be efficiently used for the measurement of evaporated neutrons from an excited compound nucleus in an in-beam experiment along with its intended use in the measurement of high energy  $\gamma$ -rays.

In future outlook, the encouraging results of the present work in this thesis open up the possibility of further studies in this direction both experimentally and theoretically. It would be interesting to compare the experimental data with TSFM by including the effect of thermal pairing. More and more experimental data are required below the critical temperature to confirm the critical

behavior in the variation of GDR width as a function of temperature. It would also be interesting if this critical behavior could be established from the first principle. On the other hand, the LAMBDA spectrometer is now ready for neutron measurement and could be used in neutron spectroscopy.



# Bibliography

- [Ago03] S. Agostinelli, et al., Nucl. Instr. and Meth. A 506 (2003) 250.
- [Alh86] Y. Alhassid, S. Levit, and J. Zingman, Phys. Rev. Lett. 57 (1986) 539, and Nucl. Phys. A469 (1987) 205 .
- [Alh88] Y. Alhassid et al, Phys. Rev. Lett. 61, (1988) 1926.
- [Alh93] Y. Alhassid and N. Whelan, Nucl. Phys. A 565, (1993) 427.
- [Aru04] P. Arumugam et al., Phys. Rev. C 69, (2004) 054313.
- [Bal47] G. C. Baldwin and G. S. Klaiber, Phys. Rev. 71, (1947) 3.
- [Ban07] K. Banerjee et al, Nucl. Instr. and Meth. A 580, (2007) 1383.
- [Ban09] K. Banerjee et al, Nucl. Instr. and Meth. A 608, (2009) 440.
- [Bar96] V. Baran et al., Nucl. Phys. A 599, (1996) 29c.
- [Bau98] T. Baumann et al., Nucl. Phys. A 635, (1998) 428.
- [Bet36] H. A. Bethe, Phys. Rev. 50, (1936) 332.
- [Boh39] N. Bohr and J. A. Wheeler, Phys. Rev. 56, (1939) 426.
- [Bor98] P. F. Bortignon, A. Bracco, and R. A. Broglia, *Giant Resonances: Nuclear Structure at Finite Temperature*, Harwood Academic Publishers (Australia 1998).
- [Bot37] W. Bothe and W. Gentner, Z. Phys. 71, (1937) 236
- [Bou85] C. Bourgeois and N. Perrin, IPNO. DRE. 85-17 Ostray (1985).
- [Bra89] A. Bracco et al., Phys. Rev. Lett. 62, (1989) 2080.
- [Bra95] A. Bracco et al., Phys. Rev. Lett. 74, (1995) 3748.

- [Bre02] T. A. Bredeweg et al., Phys. Rev. C 66 (2002) 014608.
- [Bri55] D. M. Brink, PhD Thesis, University of Oxford, 1955 (Unpublished).
- [Bro59] G. E. Brown and M. Bolsterli, Phys. Rev. Lett. 3, (1959) 472.
- [Bru86] R. Brun, et al, GEANT3, CERN-DD/EE/84-1, 1986.
- [Bud88] C. Budtz-Jorgensen and H. H. Knitter, Nucl. Phys. A 490, (1988) 307.
- [Cha87] D. R. Chakrabarty et al, Phys. Rev. C 36, (1987) 1886.
- [Cha88] D. R. Chakrabarty et al, Phys. Rev. C 37, (1988) 1437.
- [Dan98] N. Dinh Dang and A. Arima, Phys. Rev. Lett. 80 (1998) 4145, Nucl. Phys. A 636 (1998) 427.
- [Dan98b] Nguyen Dinh Dang and Akito Arima, Phys. Rev. Lett. 80, (1998) 4145.
- [Dan12a] N. Dinh Dang, Phys. Rev. C 85 (2012) 2023.
- [Dan12b] N. Dinh Dang and N. Quang Hung, Phys. Rev. C 86 (2012) 044333.
- [Dan03] Nguyen Dinh Dang and Akito Arima, Phys. Rev. C 68, (2003) 044303.
- [Dee10a] Deepak Pandit et al, Nucl. Instr. and Meth. A 624, (2010) 148.
- [Dee10b] Deepak Pandit et al, Phys. Rev. C 81, (2010) 061302(R).
- [Dee10c] Deepak Pandit et al., Phys. Lett. B 690 (2010) 473.
- [Dee12a] Deepak Pandit et al., Phys. Lett. B 713, (2012) 434.
- [Dee12b] Deepak Pandit, PhD Thesis, Homi Bhabha National Institute, India, 2012 (Unpublished).
- [Dee13] Deepak pandit et al., Phys. Rev. C 87, (2013) 044325.
- [Dey13] Balaram Dey et al, Nucl. Instr. and Meth. A 727, (2013) 7.
- [Dey14] Balaram Dey et al., Phys. Lett. B 731, (2014) 92.
- [Die74] F. S. Dietrich et al, Phys. Rev. C 10, (1974) 795.
- [Dil73] W. Dilg et al, Nucl. Phys. A 217, (1973) 269.
- [Dra82] J. K. Draper et al., Phys. Rev. Lett. 49, (1982) 434.

- [End92] G. Enders et al., Phys. Rev. Lett. 69, (1992) 249.
- [Fao94] J. H. L Faou et al., Phys. Rev. Lett. 72, (1994) 3321.
- [Gaa84] J.J.Gaardhoje et al., Phys. Rev. Lett. 53, (1984) 148.
- [Gaa86] J.J.Gaardhoje et al., Phys. Rev. Lett. 56, (1986) 1783.
- [Gaa87] J.J.Gaardhoje et al., Phys. Rev. Lett. 59, (1987) 1409.
- [Gaa92] J.J.Gaardhoje, Annu. Rev. Nucl. Part. Sci. 42, (1992) 483.
- [Gal85] M. Gallardo et al, Nucl. Phys. A 443, (1985) 415.
- [Gal87] M. Gallardo, F. J. Luis, and R. A. Broglia, Phys. Lett. B 191, (1987) 222.
- [Ger83] German et al., Phys. Rev. C(R). 28, (1983) 2554.
- [Gol48] M. Goldhaber and E. Teller Phys. Rev. 74 (1948) 1046.
- [Goh12] M. Gohil et al, Nucl. Instr. and Meth. A 664, (2012) 304.
- [Gun05] K. Gunzert-Marx et al., Nucl. Instr. and Meth. A 536 (2005) 146.
- [Hab97] M. K. Habior et al, Acta Physica polonica B 28, (1997) 189.
- [Har01] M. N. Harakeh and A. van der Woude, *Giant Resonances, Fundamental High-frequency Modes of Nuclear Excitation*, Clarendon Press, Oxford, 2001.
- [Hec03a] P. Heckman et al, Phys. Lett. B 555, (2003) 43.
- [Hec03b] P. Heckman, PhD Thesis, Michigan State University, 2003 (Unpublished).
- [Hil53] D. L. Hill and J. A. Wheeler, Phys. Rev. 89, (1953) 1102.
- [Hof94] H.J. Hofmann et al., Nucl. Phys. A 571, (1994) 301.
- [Hui62] J. R. Huizenga and G. Igo, Nucl. Phys. 29, (1962) 462.
- [Ign75] A. V. Ignatyuk, G. N. Smirenkin, and A. S. Tishin, Sov. J. Nucl. Phys. 21,(1975) 255 [Yad. Fiz. 21, 485 (1975)].
- [Jun08] A.R. Junghans et al., Phys. Lett. B 670, (2008) 200.
- [Kas92] J. Kasagi et al., Nucl. Phys. A 538, (1992) 585.

- [kat78] S. K. Kataria, V. S. Ramamurthy, and S. S. Kapoor, Phys. Rev. C 18, (1978) 549.
- [Kel99] M. P. Kelly et al., Phys. Rev. Lett. 82, (1999) 3404.
- [Kic87] M. Kicinska-Habior, et al., Phys. Rev. C 36 (1987) 612.
- [Knol] G. F. Knoll, Radiation Detection and Measurements, 3rd ed., Wiley, New York.
- [Kov79] M. A. Kovash et al, Phys. Rev. Lett. 42, (1979) 700.
- [Kry94] R. A. Kryager et al., Nucl. Instr. and Meth. A 346 (1994) 544.
- [Kub89] S. Kubota et al., Nucl. Instr. and Meth. A 285 (1989) 436.
- [Kus98] D. Kusnezov, Y. Alhassid, and K. A. Snover, Phys. Rev. Lett. 81, (1998) 542 and references therein.
- [Lan97] G. Lanzano et al., Nuovo Cimento. 110A (1997) 505.
- [Lev84] S. Levit and Y. Alhassid, Nucl. Phys. A 413, (1984) 439.
- [Mat89] T. Matulewicz et al., Nucl. Instr. and Meth. A 274 (1989) 501.
- [Mat97] M. Mattiuzi et al., Nucl. Phys. A 612, (1997) 262.
- [Nak01] N. Nakao et al., Nucl. Instr. and Meth. A 463 (2001) 275.
- [Nif90] H. Nifennecker and J. A. Pinston, Annu. Rev. Nucl. Part.Sci. 40, (1990) 113 .
- [Noo94] R. F. Noorman et al., Nucl. Phys. A 574, (1994) 501.
- [Per63] F. G. Perey, Phys. Rev. 131, (1963) 745.
- [Pra12] Pratap Roy, et al., Phys. Rev. C 86 (2012) 044622.
- [Puh77] F. Pühlhofer, Nucl. Phys. 280, (1977) 267.
- [Ram95] E. Ramakrishnan, PhD Thesis, Michigan State University, 1995 (Unpublished).
- [Ram96] E. Ramakrishnan et al, Phys. Rev. Lett. 76, (1996) 2025.
- [Rat03a] S. K. Rathi, PhD Thesis, Bombay University, 2003 (Unpublished).
- [Rei81] W. Reisdorf, et al., Z. Phys. A 300, (1981) 227.
- [Tho87] M. Thoennessen et al., Phys. Rev. Lett. 59 (1987) 2860.

## Bibliography

---

- [Tri08] L. Trippa, G. Colo and E. Vigezzi, *Phys. Rev. C* 77, (2008) 061304(R).
- [Trz01] Z. Trznadel et al., *Nucl. Phys. A* 687, (2001) 198.
- [Sch07] A. Schiller and M. Thoennessen., *Atomic Data and Nuclear Tables* 93 (2007) 549-573.
- [Sha99] N. P. Shaw, PhD Thesis, State University of New York at Stony Brook, 1999 (Unpublished).
- [Sim09] C. Simenel et al., *Phys. Rev. C* 80 (2009) 064309.
- [Sme91] A. Smerzi, A. Bonasera and M. DiToro, *Phys. Rev. C* 44, (1991) 1713.
- [Sno86] K.A. Snover, *Annu. Rev. Nucl. Part.Sci.* 36, (1986) 545.
- [Spe91] J. Speth, *Electric and Magnetic Giant Resonance in Nuclei*, World Scientific Publishing Co. Pte. Ltd, 1991.
- [Sri08a] Srijit Bhattacharya, 2008, PhD Thesis, University of Calcutta, 2007 (Unpublished).
- [Sri08b] Srijit Bhattacharya et al, *Phys. Rev. C* 77, (2008) 024318.
- [Sri14] Srijit Bhattacharya et al, *Phys. Rev. C* 90, (2014) 054319.
- [Ste50] H. Steinwedel and J. H. D. Jensen, *Z. Naturforsch.* 5a (1950) 413.
- [Sto89] A. Stolk, et al., *Nucl. Phys. A* 505 (1989) 241.
- [Suk95] Cs. Sükösd et al., *Nucl. Instr. and Meth. A* 355, (1995) 552.
- [Sup07] S. Mukhopadhyay et al, *Nucl. Instr. and Meth. A* 582, (2007) 603.
- [Sup12a] S. Mukhopadhyay et al., *Phys. Lett. B* 709 (2012) 9.
- [Sup12b] S. Mukhopadhyay, PhD Thesis, University of Calcutta, India, 2012 (Unpublished).
- [Vie96] G. Viesti et al., *Nucl. Phys. A* 604, (1996) 81.
- [Wag97] V. Wagner et al., *Nucl. Instr. and Meth. A* 394 (1997) 332.
- [Wie06] O. Wieland et al., *Phys. Rev. Lett.* 97, (2006) 012501.
- [Wil56] D. H. Willkinson, *Physica* 22, (1956) 1039.
- [Wil64] D. Wilmore and P. E. Hodgson, *Nucl. Phys.* 55, (1964) 673.